LANGLEY
GRANT
IN-32-CR
70321
P- 30

HIGH-FREQUENCY TECHNIQUES FOR RCS PREDICTION OF PLATE GEOMETRIES

Semiannual Progress Report

Constantine A. Balanis and Lesley A. Polka

August 1, 1991 - January 31, 1992

Department of Electrical Engineering
Telecommunications Research Center
Arizona State University
Tempe, Arizona 85287-7206

HIGH-FREQUENCY TECHNIQUES FOR RCS PREDICTION OF PLATE GEOMETRIES

Semiannual Progress Report

Constantine A. Balanis and Lesley A. Polka

August 1, 1991 - January 31, 1992

Department of Electrical Engineering
Telecommunications Research Center
Arizona State University
Tempe, Arizona 85287-7206

ABSTRACT

This report examines the principal-plane scattering from perfectly conducting and coated strips and rectangular plates. Previous reports have detailed Geometrical Theory of Diffraction/Uniform Theory of Diffraction (GTD/UTD) solutions for these geometries. The GTD/UTD solution for the perfectly conducting plate yields monostatic RCS results that are nearly identical to measurements and results obtained using the Moment Method (MM) and the Extended Physical Theory of Diffraction (EPTD). This was demonstrated in previous reports. This report extends the previous analysis to bistatic cases. GTD/UTD results for the principal-plane scattering from a perfectly conducting, infinite strip are compared to MM and EPTD data. A comprehensive overview of the advantages and disadvantages of the GTD/UTD and of the EPTD and a detailed analysis of the results from both methods are provided.

Several previous reports also presented preliminary discussions and results for a GTD/UTD model of the RCS of a coated, rectangular plate. Several approximations for accounting for the finite coating thickness, plane-wave incidence, and far-field observation were discussed. In this report, these approximations are replaced by a revised wedge diffraction coefficient that implicitly accounts for a coating on a perfect conductor, plane-wave incidence, and far-field observation. This coefficient is computationally more efficient than the previous diffraction coefficient because the number of Maliuzhinets functions that must be calculated using numerical integration is reduced by a factor of 2. The derivation and the

revised coefficient are presented in detail for the hard polarization

case. Computations and experimental data are also included. The soft

polarization case is currently under investigation.

I. INTRODUCTION

The research of previous reporting periods [1]-[6] has dealt with high-frequency methods for the prediction of scattering from basic geometries whose properties are of interest for modeling more complicated, practical radar targets. Nonprincipal-plane scattering from perfectly conducting, rectangular plates has been explored using the Method of Equivalent Currents (MEC). Several variations on the technique have been investigated for first-order diffraction prediction. Second-order effects and corner diffraction have also been investigated using several different models and measurements.

More recent reports [1]-[3] have concentrated on monostatic, principal-plane scattering from perfectly conducting and coated strips and plates with an emphasis on near-grazing and grazing incidence and higher-order diffractions. This report presents bistatic results for the perfectly conducting strip/plate geometry and a comprehensive overview for applying the Geometrical Theory of Diffraction/Uniform Theory of Diffraction (GTD/UTD) [7], [8] and the Extended Physical Theory of Diffraction (EPTD) [9]-[11] to problems involving the scattering between two parallel wedges separated by an electrically small distance ($\lambda/2$ - 2λ). Extensive comparisons among GTD/UTD, EPTD, and Moment Method (MM) results are included.

In addition to the perfectly conducting plate model, a revised model for the coated plate is discussed. Previous reports [1], [3] have discussed approximations for incorporating a finite-thickness coating on top of a perfect conductor and plane-wave incidence,

3

far-field observation into the impedance wedge diffraction coefficient

developed by Tiberio, *et al.* [12] and Griesser and Balanis [13] from

Maliuzhinets' solution [14]. This report examines the diffraction

coefficient for the general impedance wedge and revises the

expressions for the specific case of a coating backed by a conductor

for plane-wave incidence, far-field observation. The result is more

intuitively correct than the previously used approximations and also

more computationally efficient because the number of ·Maliuzhinets

functions that must be computed by numerical integration is reduced

from 12 to 6. Computed results and measured data are included for the

hard polarization. Work is currently in progress on the soft

polarization case.

II. THEORY AND RESULTS

A. PRINCIPAL-PLANE SCATTERING FROM A PERFECTLY CONDUCTING, RECTANGULAR PLATE

The infinite strip and corresponding plate geometries are shown

in Fig. 1. The strip width is w; the plate length is L. The

incidence and observation angles are ϕ' and ϕ, respectively. [1] and

[3] contained details and analyses of the monostatic GTD/UTD model.

The bistatic model is simply a more generalized version of the

previous model. As a review, the infinite strip is modeled as two

infinite half planes. This approximation is, of course, more valid

for electrically large strip widths; however, it was demonstrated in

[1] and [3] that the monostatic model performs remarkably well for

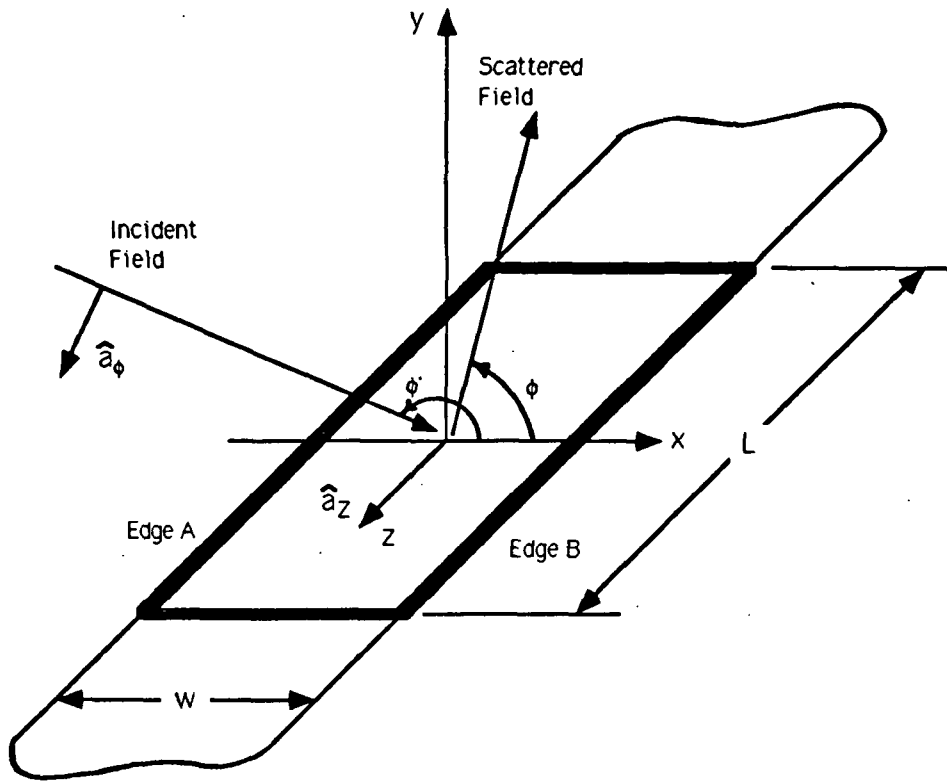widths as small as $\lambda/2$. The radar cross section (RCS) of a finite,

Fig. 1. Perfectly conducting strip/plate geometry
for principal-plane scattering.

rectangular plate is approximated from the scattering width (SW) of the corresponding infinite strip using the truncation approximation [15]:

$$\sigma_{3-D} \cong \frac{2L^2}{\lambda} \sigma_{2-D} \tag{1}$$

The GTD/UTD model consists of Keller's diffraction coefficient [7] for first-order terms. For the soft polarization, no higher-order terms exist due to boundary conditions; however, a slope term is included in the model using the slope diffraction coefficient [16]. Higher-order terms for the hard polarization are easy to include using the UTD diffraction coefficients [8]. Typically up to fourth-order terms are sufficient for accurate prediction, even for diffraction distances as small as $\lambda/2$; thus, the results presented here include first-, second-, third-, and fourth-order terms only.

The incident fields for both polarizations are:

Soft Polarization

$$\underline{E_i} = \hat{a}_z \, E_o e^{jk(x\cos(\phi') \, + \, y\sin(\phi'))} \tag{2a}$$

Hard Polarization

$$\underline{E_i} = -\hat{a}_\phi \, E_o e^{jk(x\cos(\phi') \, + \, y\sin(\phi'))} \tag{2b}$$

An $e^{j\omega t}$ time convention is assumed and suppressed. The resulting diffracted fields are obtained using a straightforward application of the GTD/UTD in which the diffracted field is a product of the incident field at the point of diffraction, the diffraction coefficient, an amplitude spreading factor, and a phase factor. The details are omitted. The resulting first-order fields are:

6

Soft Polarization

$$\underline{E}^{1st} = \hat{a}_z \, E_0 \, \frac{e^{-jk\rho}}{\sqrt{k\rho}} \left[\frac{-e^{-j\pi/4}}{\sqrt{2\pi}} \right] \left\{ \frac{\cos\left(\frac{kw}{2}(\cos\phi' + \cos\phi) \right)}{\cos\left(\frac{\phi - \phi'}{2} \right)} \right. \tag{3a}$$

$$\left. + j \, \frac{\sin\left(\frac{kw}{2}(\cos\phi' + \cos\phi) \right)}{\cos\left(\frac{\phi + \phi'}{2} \right)} \right\}$$

Hard Polarization

$$\underline{E}^{1st} = -\hat{a}_\phi \, E_0 \, \frac{e^{-jk\rho}}{\sqrt{k\rho}} \left[\frac{-e^{-j\pi/4}}{\sqrt{2\pi}} \right] \left\{ \frac{\cos\left(\frac{kw}{2}(\cos\phi' + \cos\phi) \right)}{\cos\left(\frac{\phi - \phi'}{2} \right)} \right. \tag{3b}$$

$$\left. - j \, \frac{\sin\left(\frac{kw}{2}(\cos\phi' + \cos\phi) \right)}{\cos\left(\frac{\phi + \phi'}{2} \right)} \right\}$$

The distance, ρ, is measured from the center of the strip to the observation point.

For the soft polarization, the slope field is:

$$\underline{E}^{slope} = \hat{a}_z \, E_0 \, \frac{e^{-jk\rho}}{\sqrt{k\rho}} \left[-j \, \frac{e^{-jkw}}{\sqrt{kw}} \right] \left[\frac{180}{w\pi} \right] \tag{4}$$

$$\times \left\{ D_{BA}^s \, DS_A \, e^{j(kw/2)(\cos\phi' - \cos\phi)} + D_{AB}^s \, DS_B \, e^{-j(kw/2)(\cos\phi' - \cos\phi)} \right\}$$

where

$$DS_A = DS(soft, \, w, \, 0°, \, \phi, \, 2, \, 90°)$$
$$DS_B = DS(soft, \, w, \, 0°, \, 180° - \phi, \, 2, \, 90°)$$
$$D_{BA}^s = D(soft, \, w, \, 180° - \phi', \, 1°, \, 2, \, 90°)$$
$$D_{AB}^s = D(soft, \, w, \, \phi', \, 1°, \, 2, \, 90°)$$

DS_A and DS_B are slope diffraction coefficients of the general form $DS(polarization, \, d, \, \psi', \, \psi, \, n, \, \beta)$, and D_{BA} and D_{AB} are UTD diffraction coefficients of the form $D(polarization, \, d, \, \psi', \, \psi, \, n, \, \beta)$. Subroutines for calculating both types of coefficients are in [17], where:

d = diffraction distance
ψ' = wedge incidence angle

ψ = wedge diffraction angle

n = wedge parameter

β = the oblique incidence angle

For the hard polarization, higher-order terms are expressed through repeated application of the UTD diffraction coefficient [8]. The general nth-order diffracted field is:

$$\underline{E}^{nth} = -\hat{a}_\phi E_o \frac{e^{-jk\rho}}{\sqrt{k\rho}} \sqrt{\frac{k}{w^{(n-1)}}} e^{-jkw(n-1)} D_n^{(n-2)}$$

$$\times \left\{ e^{(-jkw/2)} \left((-1)^{(n-1)} \cos\phi' + \cos\phi \right) D_{Ai} D_{Ao} \right.$$

$$\left. + e^{(jkw/2)} \left((-1)^{(n-1)} \cos\phi' + \cos\phi \right) D_{Bi} D_{Bo} \right\}$$

(5)

where

$$D_n = D(hard, w, 0°, 0°, 2, 90°)$$

$$D_{Ai} = D\left(hard, w, \begin{array}{l} 180°-\phi' \ (n=even) \\ or \\ \phi' \ (n=odd) \end{array}, 0°, 2, 90°\right)$$

$$D_{Ao} = D(hard, w, 0°, \phi, 2, 90°)$$

$$D_{Bi} = D\left(hard, w, \begin{array}{l} 180°-\phi' \ (n=odd) \\ or \\ \phi' \ (n=even) \end{array}, 0°, 2, 90°\right)$$

$$D_{Bo} = D(hard, w, 0°, 180°-\phi, 2, 90°)$$

As previously, D(polarization, d, ψ', ψ, n, β) is the UTD diffraction coefficient.

The GTD/UTD formulation is not theoretically valid at and near grazing incidence because overlapping transition regions exist at these angles. One method that is capable of dealing with the fields in overlapping transition regions is the EPTD. This method is a

8

high-frequency asymptotic technique that is as computationally efficient as the GTD/UTD; however, explicit diffraction coefficients do not exist. The method is, thus, much more difficult to apply than the GTD/UTD. The last report [1] analyzed the error in the GTD/UTD formulation for monostatic scattering. Extensive comparisons among measurements, MM data, and EPTD data for the monostatic case revealed that the error due to using the GTD/UTD in overlapping transition regions was minor for this case except within a few degrees of grazing incidence, even for very narrow diffraction distances. It was also demonstrated that the error due to using the truncation approximation of Eq. (1) was increasingly significant as the diffraction distance increased, whereas the error due to using the GTD/UTD in overlapping transition regions decreased with increasing diffraction distance.

This report continues the investigation of the errors inherent in the GTD/UTD model by comparing MM and EPTD results with the GTD/UTD results for bistatic scattering from the infinite strip. The EPTD model follows from the formulation of [9]. The first-order fields are the GTD fields of Eq. (3). For the soft polarization, a slope diffracted field similar to that of Eq. (4) is used for the edge that is not in an overlapping transition region for a particular incidence angle. Recall, however, that the expression of Eq. (4) is for the total slope-diffracted field from both edges not from a single edge. The field diffracted from an edge in an overlapping transition region is expressed using the EPTD:

Left Edge (Edge A)

$$\underline{E}^{slope} = \hat{a}_z\, E_o \frac{e^{-jk\rho}}{\sqrt{k\rho}} \left[\frac{e^{-j\pi/4}}{\sqrt{8\pi}}\right] \left(e^{-jkw}e^{(jkw/2)(\cos\phi'-\cos\phi)}\right) \tag{6a}$$

$$\times \left\{ \frac{-e^{-j\pi/4}}{\sqrt{\frac{\pi kw}{2}}\left(\cos(\phi'/2)+\sin(\phi/2)\right)} \right.$$

$$+ \left(\frac{8}{\cos\phi'+\cos\phi}\right)\left[\cos\left(\frac{\phi'}{2}\right)\left|\cos\left(\frac{\phi}{2}\right)\right| F\left(\sqrt{2kw}\,|\cos(\phi/2)\,|\right)\right.$$

$$\left.\left.- \sin\left(\frac{\phi}{2}\right)\left|\sin\left(\frac{\phi'}{2}\right)\right| F\left(\sqrt{2kw}\,|\sin(\phi'/2)\,|\right)\right]\right\}$$

Right Edge (Edge B)

$$\underline{E}^{slope} = \hat{a}_z\, E_o \frac{e^{-jk\rho}}{\sqrt{k\rho}} \left[\frac{e^{-j\pi/4}}{\sqrt{8\pi}}\right] \left(e^{-jkw}e^{(-jkw/2)(\cos\phi'-\cos\phi)}\right) \tag{6b}$$

$$\times \left\{ \frac{-e^{-j\pi/4}}{\sqrt{\frac{\pi kw}{2}}\left(\sin(\phi'/2)+\cos(\phi/2)\right)} \right.$$

$$+ \left(\frac{8}{\cos\phi'+\cos\phi}\right)\left[\cos\left(\frac{\phi}{2}\right)\left|\cos\left(\frac{\phi'}{2}\right)\right| F\left(\sqrt{2kw}\,|\cos(\phi'/2)\,|\right)\right.$$

$$\left.\left.- \sin\left(\frac{\phi'}{2}\right)\left|\sin\left(\frac{\phi}{2}\right)\right| F\left(\sqrt{2kw}\,|\sin(\phi/2)\,|\right)\right]\right\}$$

There are no specific criteria for determining the range of incidence angles for which an edge is in an overlapping transition region. Through trial and error, however, it was found that excellent results are obtained by approximating that the left edge is in an overlapping transition region when $0° \le \phi' \le 90°$ and that the right edge is in an overlapping transition region when $90° \le \phi' \le 180°$. These same criteria are used for determining when an edge is in a transition region for the hard polarization.

For the hard polarization, the second-order field diffracted by an edge that is not in an overlapping transition region is represented by an expression similar to that of Eq. (5). Note that Eq. (5) represents the total second-order field, not just the field from a single edge. The second-order field for an edge in an overlapping transition region is represented using the EPTD as:

Left Edge (Edge A)

$$E^{2nd} = -\hat{a}_\phi E_0 \frac{e^{-jk\rho}}{\sqrt{k\rho}} \left[\frac{e^{-j\pi/4}}{\sqrt{8\pi}} \right] \left(e^{-jkw} e^{(jkw/2)(\cos\phi'-\cos\phi)} \right) \qquad (7a)$$

$$\times \left\{ \frac{e^{-j\pi/4}}{\sqrt{\frac{\pi kw}{2}} \sin(\phi'/2) \cos(\phi/2)} \right.$$

$$+ \left(\frac{8}{\cos\phi'+\cos\phi} \right) \left[\cos\left(\frac{\phi'}{2}\right) \cos\left(\frac{\phi}{2}\right) \left(F\left(\sqrt{2kw}|\sin(\phi'/2)|\right) - \frac{e^{-j\pi/4}}{\sqrt{8\pi kw} \sin\left(\frac{\phi'}{2}\right)} \right) \right.$$

$$\left. - \sin\left(\frac{\phi'}{2}\right) \sin\left(\frac{\phi}{2}\right) \left(F\left(\sqrt{2kw}|\cos(\phi/2)|\right) - \frac{e^{-j\pi/4}}{\sqrt{8\pi kw} \cos\left(\frac{\phi}{2}\right)} \right) \right]$$

Right Edge (Edge B)

$$E^{2nd} = -\hat{a}_\phi E_0 \frac{e^{-jk\rho}}{\sqrt{k\rho}} \left[\frac{e^{-j\pi/4}}{\sqrt{8\pi}} \right] \left(e^{-jkw} e^{(-jkw/2)(\cos\phi'-\cos\phi)} \right) \qquad (7b)$$

$$\times \left\{ \frac{e^{-j\pi/4}}{\sqrt{\frac{\pi kw}{2}} \cos(\phi'/2) \sin(\phi/2)} \right.$$

$$+ \left(\frac{8}{\cos\phi'+\cos\phi} \right) \left[\cos\left(\frac{\phi'}{2}\right) \cos\left(\frac{\phi}{2}\right) \left(F\left(\sqrt{2kw}|\sin(\phi/2)|\right) - \frac{e^{-j\pi/4}}{\sqrt{8\pi kw} \sin\left(\frac{\phi}{2}\right)} \right) \right.$$

$$\left. - \sin\left(\frac{\phi'}{2}\right) \sin\left(\frac{\phi}{2}\right) \left(F\left(\sqrt{2kw}|\cos(\phi'/2)|\right) - \frac{e^{-j\pi/4}}{\sqrt{8\pi kw} \cos\left(\frac{\phi'}{2}\right)} \right) \right]$$

Higher-order fields for the hard polarization case are formulated in terms of the UTD coefficients, and the results are similar to Eq.

(5). The EPTD fields must be incorporated as the incident fields. The formulation is trivial. Since the resulting equations are similar to those of Eq. (5), they will not be repeated here.

Results from the GTD/UTD and the EPTD models are compared with MM data for bistatic scattering from a strip in Figs. 2 - 9. The bistatic SW is shown for both polarizations, various incidence angles, and two different strip widths $(w=\lambda/2$ and $w=2\lambda)$. In general, the EPTD results for the soft polarization cases of Figs. 2, 3, 4, and 6 are in exact agreement with the MM data, even for the electrically small distance of $\lambda/2$ and grazing incidence case of Fig. 2. The only soft polarization case for which the EPTD yields results that are not identical to the MM is the $\lambda/2$, $\phi'=135^{\circ}$ case of Fig. 8. In this instance, a discrepancy of approximately 1.5 dB exists at $\phi=180^{\circ}$. Nearly exact agreement between the EPTD and the MM is obtained for the hard polarization cases of Figs. 5, 7, and 9. Results for grazing incidence, hard polarization are not shown because they are trivially zero due to boundary conditions. Exact agreement is obtained in the forward direction, for hard polarization; and the agreement begins to slowly deteriorate in the backscattering direction. The EPTD results in and near the backscattering direction improve with increasing strip width. For the 2λ-width strip of Fig. 7, the largest error in the EPTD results is approximately 1-dB.

The GTD/UTD model does not perform well at exactly grazing incidence, as is demonstrated in Figs. 2 and 3. The GTD/UTD results, however, quickly converge to the MM/EPTD values as the backscattering direction is approached to the extent that the GTD/UTD result for the

12
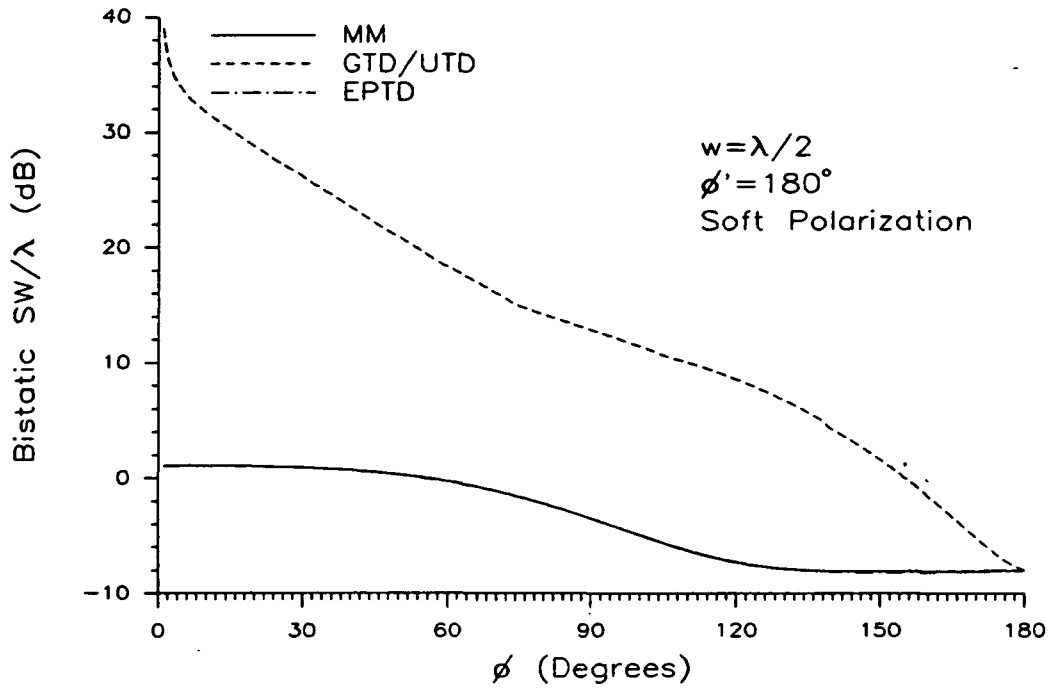
Fig. 2. Principal—plane, bistatic SW of an infinite strip.
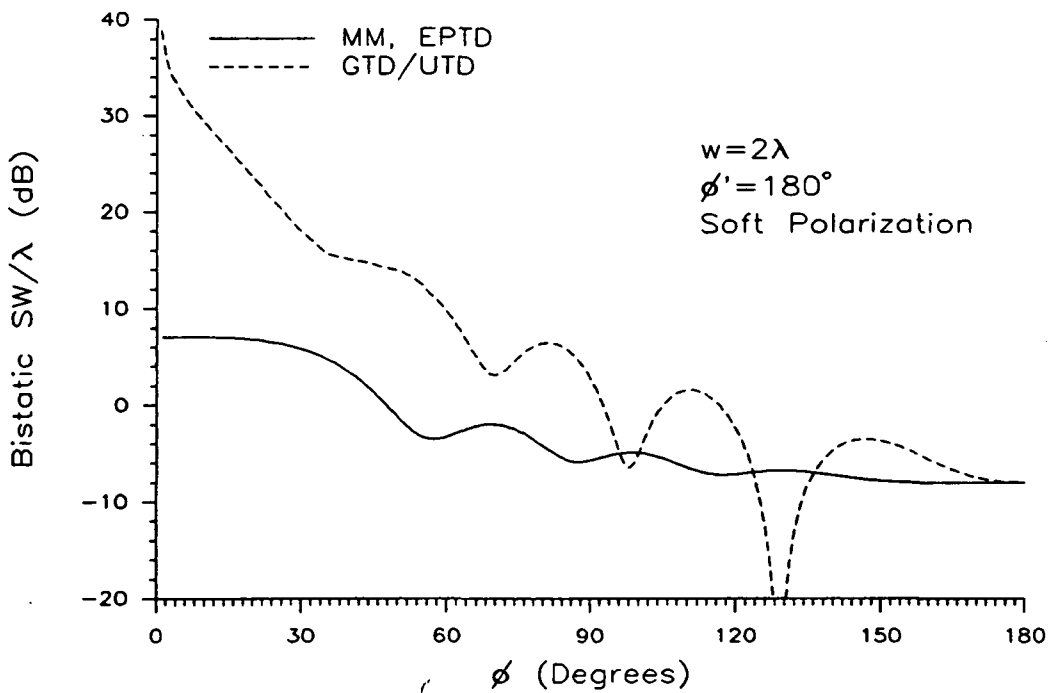
Fig. 3. Principal—plane, bistatic SW of an infinite strip.
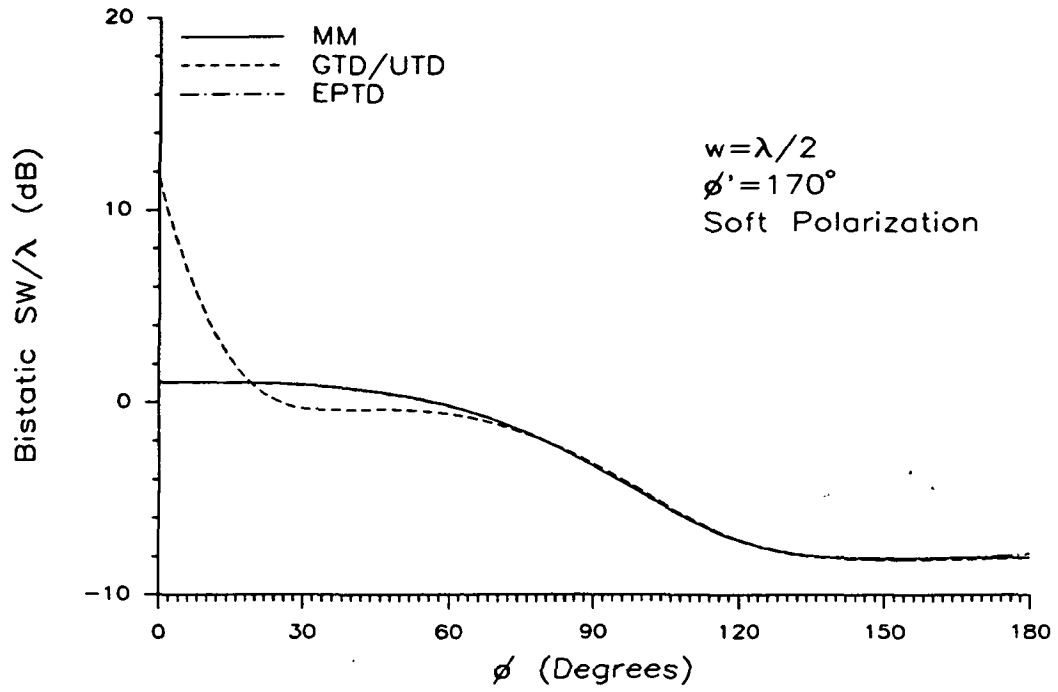
Fig. 4. Principal—plane, bistatic SW of an infinite strip.
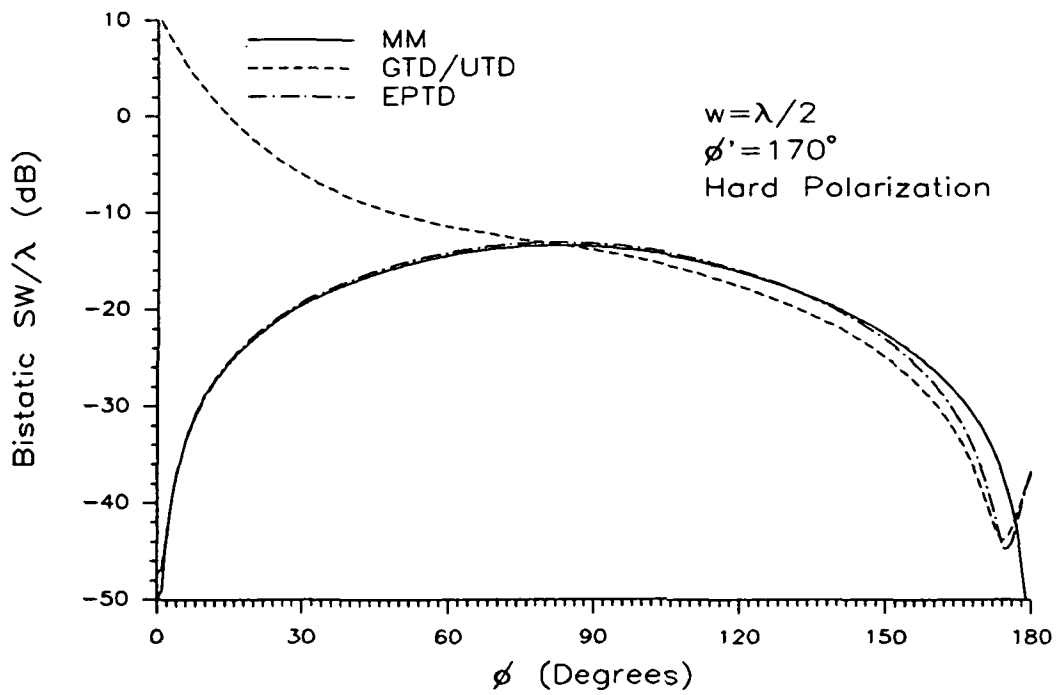
Fig. 5. Principal—plane, bistatic SW of an infinite strip.
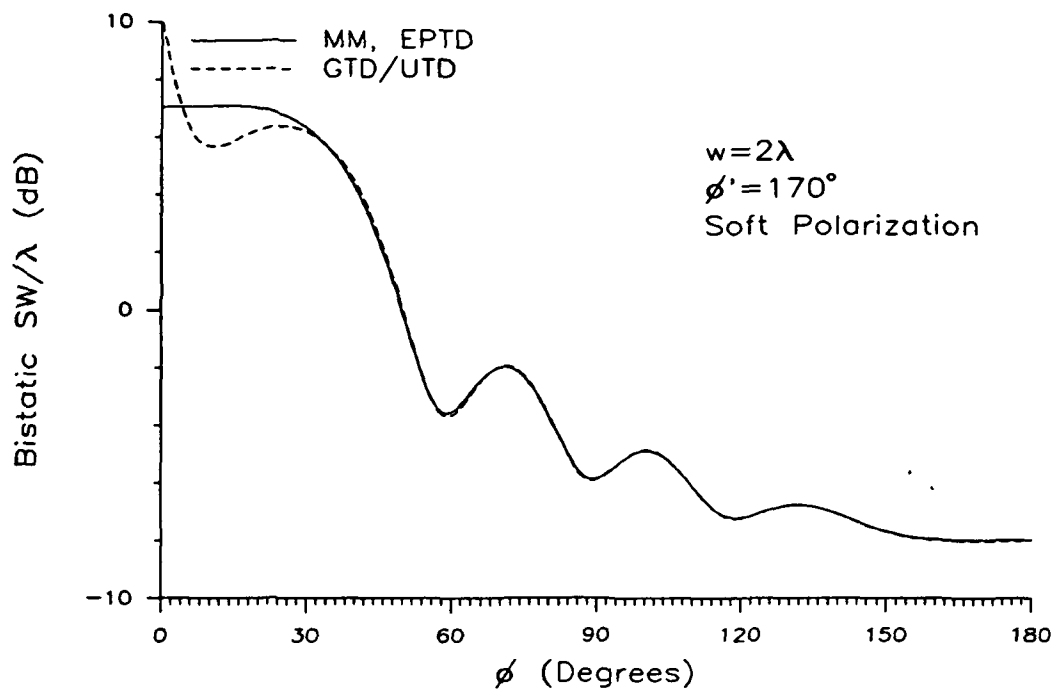
Fig. 6. Principal—plane, bistatic SW of an infinite strip.
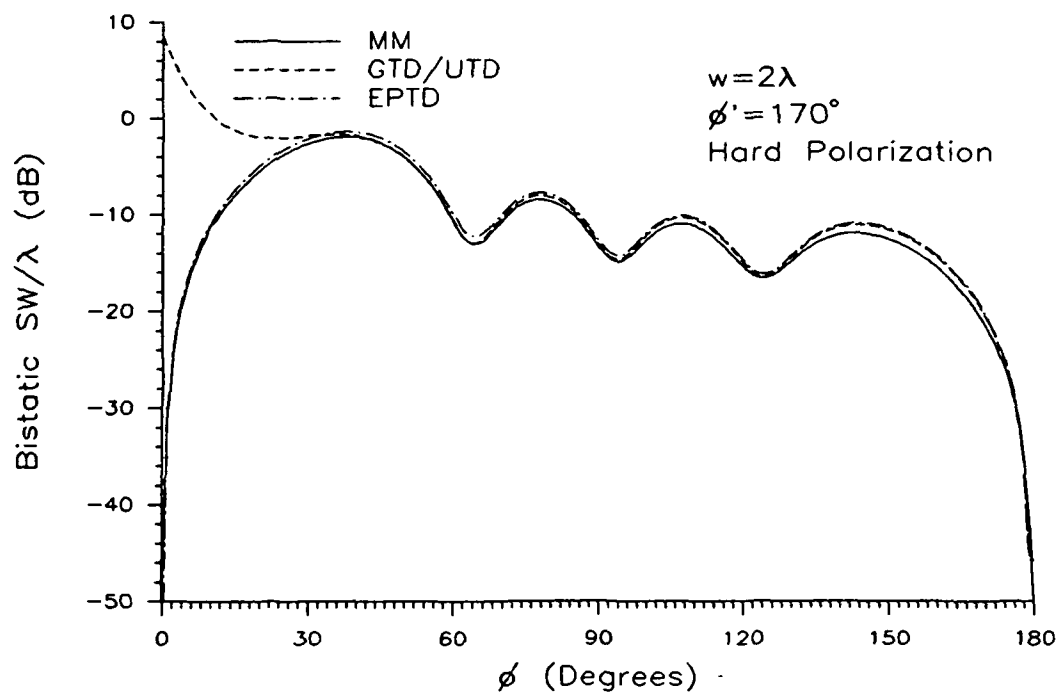
Fig. 7. Principal—plane, bistatic SW of an infinite strip.

15
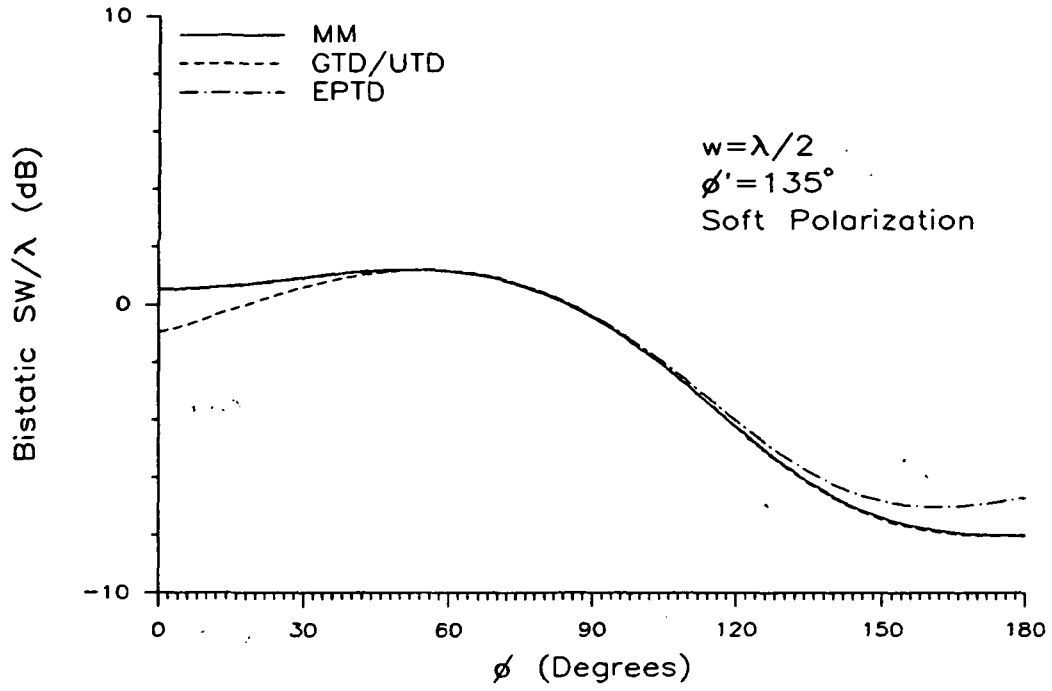
Fig. 8. Principal-plane, bistatic SW of an infinite strip.
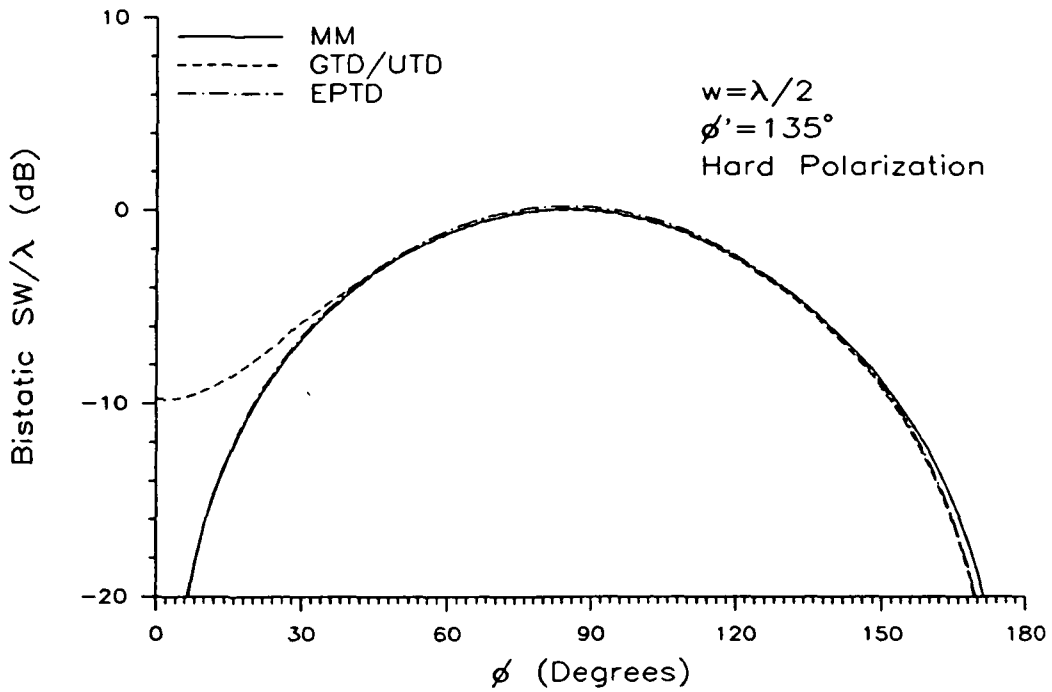
Fig. 9. Principal-plane, bistatic SW of an infinite strip.

16

$\lambda/2$-width strip of Fig. 2 differs by only 0.08 dB from the MM/EPTD result at the backscatter direction ($\phi=180°$). The GTD/UTD results of Figs. 4 - 9 illustrate the general improvement of the model with increasing strip width away from but still near grazing incidence. The soft polarization results are, in general, better than the hard. In the backscatter direction, the GTD/UTD model yields nearly the same results as the EPTD, which are usually the same as the MM values for the soft polarization.

Other bistatic cases for both polarizations were analyzed to compile a comprehensive set of data. Strip widths considered ranged from $\lambda/4$ to 3.183λ in width and incidence angles from grazing ($\phi'=180°$) to $45°$ from grazing ($\phi'=135°$). The most interesting and representative results are given in Figs. 2 - 9; however, an analysis of all the available data affords the following observations concerning the effectiveness of the GTD/UTD and the EPTD:

(1) For most backscattering ($\phi=\phi'$) cases, the GTD/UTD yields results identical to the EPTD for both polarizations and strip widths as small as $\lambda/4$, including grazing incidence ($\phi'=180°$). The two exceptions to this are for the hard polarization, $\lambda/2$ and $\phi'=170°$ case of Fig. 5 and for the soft polarization, $\lambda/2$ and $\phi'=135°$ case of Fig. 8. In the first case, a difference of 2.1 dB exists between the GTD/UTD and the EPTD. It is important to note that for this case the EPTD differs from the MM by over 4 dB. In the second case, the GTD/UTD differs from the EPTD by 0.4 dB. In this case the GTD/UTD provides nearly exact agreement with the MM whereas the EPTD differs from the MM by almost 0.4 dB.

(2) For both polarizations, the GTD/UTD results improve rapidly as the strip width increases and as the incidence angle *moves beyond the grazing angle*. For soft polarization and near-grazing incidence ($\phi'=170°$), the GTD/UTD results agree identically with the MM and EPTD data for a large range of observation angles away from the forward scattering direction. The range of agreement increases dramatically with increasing strip width. Even for a width as small as $\lambda/4$ at $\phi'=170°$, accurate results (less than 0.4 dB

discrepancy) are obtained for observation angles in the range $90° \leq \phi \leq 180°$.

(3) The range of agreement between the GTD/UTD and the EPTD is smaller for the hard polarization and near-grazing incidence cases ($\phi'=170°$); however, differences of less than 2 dB are obtained for this case for a strip width as small as $\lambda/3$ in the observation range of $90° \leq \phi \leq 180°$.

(4) For angles away from grazing incidence ($\phi'=135°$) for both polarizations, the GTD/UTD model yields nearly identical results to the MM and the EPTD models for the 2λ-width strip. For this incidence angle, soft polarization, and the $\lambda/2$-width strip, the GTD/UTD model agrees identically with the MM for $45° \leq \phi \leq 180°$. The accuracy of the GTD/UTD slowly deteriorates in the $0° \leq \phi \leq 45°$ range to a maximum error of 1.5 dB at $\phi=0°$. For the same incidence angle and $\lambda/2$-width strip for the hard polarization, the GTD/UTD agrees within 0.5 dB with the MM and the EPTD in the $45° \leq \phi \leq 160°$ region; however, the error in the GTD/UTD gradually becomes unacceptable in the $0° \leq \phi \leq 45°$ region and increases to 2 dB in the $160° \leq \phi \leq 180°$ region.

(5) The EPTD yields highly accurate results for nearly all scattering widths, incidence and observation angles and both polarizations. For most cases it is difficult to distinguish between the EPTD and the MM results. The few exceptions are interesting. The only soft polarization case for which the EPTD differs remarkably from the MM is for the 0.5λ strip and $\phi'=135°$. The EPTD model gradually begins to deteriorate in the backscatter region ($125° \leq \phi \leq 180°$) to a maximum discrepancy of 1.5 dB at $\phi=180°$. For this case, the GTD/UTD agrees exactly with the MM in the backscatter region ($125° \leq \phi \leq 180°$) and, thus, provides much better results than the EPTD. A similar trend of deterioration in the backscattering direction is much more evident in the hard polarization results. For all strip widths and incidence angles considered for this polarization, the EPTD results differ, usually within acceptable limits, from the MM data. The worst agreement observed is for the $\lambda/2$ and $\phi'=170°$ case of Fig. 5. The discrepancies between the EPTD and MM decrease with increasing strip width.

(6) For soft polarization and grazing incidence ($\phi'=0°$ or $180°$), the GTD/UTD yields highly inaccurate results except in the backscattering direction ($\phi=\phi'$).

B. PRINCIPAL-PLANE SCATTERING FROM A COATED, RECTANGULAR PLATE

The geometry for the coated, rectangular plate is shown in Fig. 10. The incidence and observation angles are ϕ' and ϕ, respectively. The plate width is w. As for the perfectly conducting plate, the RCS
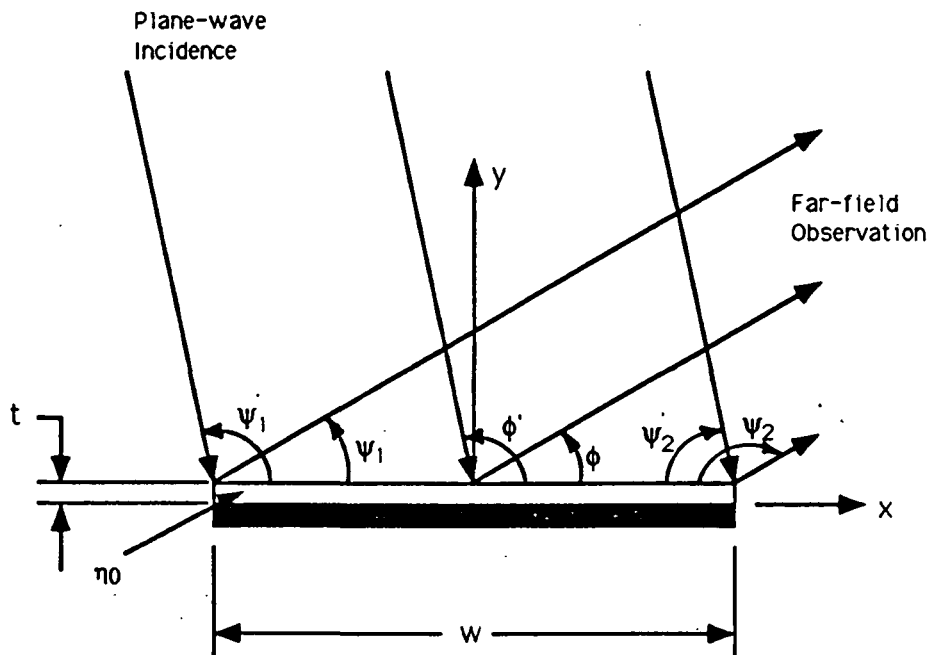
Fig. 10. Geometry for principal-plane scattering from a strip/plate
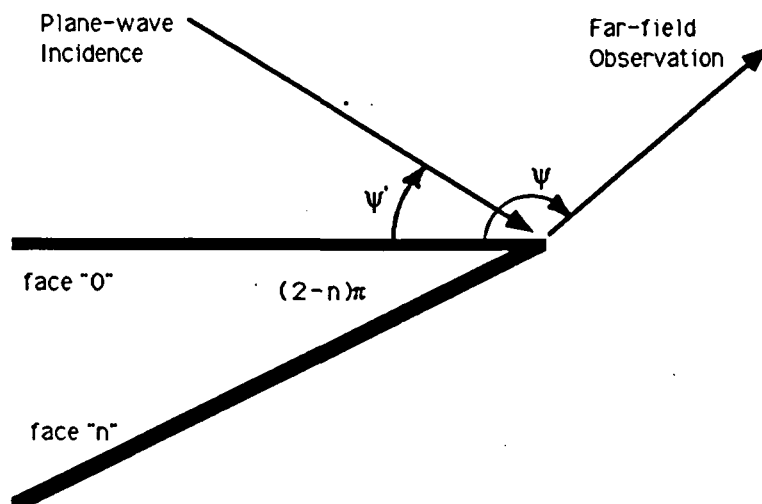with a finite-thickness coating backed by a perfect conductor.

Fig. 11. Impedance wedge geometry.

will be approximated from the SW of the infinite strip using Eq. (1).

The relative permittivity and permeability of the coating material are

ε_{r0} and μ_{r0}, respectively. The plate is modeled as two infinite

half-planes. The geometry of the impedance wedge is illustrated in

Fig. 11. The incidence and observation angles with respect to the

wedge are designated as ψ' and ψ, respectively. These angles, for the

plate of Fig. 10, are designated as ψ_1' and ψ_1 for the left edge (Edge

1) and as ψ_2' and ψ_2 for the right edge (Edge 2). In Fig. 11, n is

the wedge parameter (n=2 for a half plane); η_0 is the impedance of the

"0" face, normalized with respect to the free-space impedance; and η_n

is the normalized impedance of the "n" face.

The incident fields for both polarizations are the same as those

of the previous section, given by Eq. (2). Using the standard

formulation for determining diffracted fields as a product of the

incident field, the diffraction coefficient, a phase factor, and an

amplitude spreading factor, the first-order diffracted fields can be

expressed as:

<u>Soft</u> <u>Polarization</u>

$$\underline{E}^{1st} = \hat{a}_z E_o \frac{e^{-jk\rho}}{\sqrt{\rho}} \left\{ e^{(-jkw/2)(\cos\phi' + \cos\phi)} D(w, \psi_1', \psi_1, \theta_0^s, \theta_2^s, 2) \right. \tag{8a}$$

$$\left. + e^{(jkw/2)(\cos\phi' + \cos\phi)} D(w, \psi_2', \psi_2, \theta_0^s, \theta_2^s, 2) \right\}$$

Hard Polarization

$$\underline{E}^{1st} = -\hat{a}_\phi E_o \frac{e^{-jk\rho}}{\sqrt{\rho}} \left\{ e^{(-jkw/2)(\cos\phi' + \cos\phi)} D(w, \psi_1', \psi_1, \theta_0^h, \theta_2^h, 2) \right.$$

(8b)

$$\left. + e^{(jkw/2)(\cos\phi' + \cos\phi)} D(w, \psi_2', \psi_2, \theta_0^h, \theta_2^h, 2) \right\}$$

$D(d, \psi', \psi, \theta_0, \theta_n, n)$ is the diffraction coefficient for an impedance wedge, where:

    d = diffraction distance

    ψ' = incidence angle

    ψ = observation angle

    θ_0, θ_n = Brewster angles of the "0" and "n" faces, respectively

    n = wedge parameter = 2 for a half plane

The Brewster angles are:

$$\theta_0 = \begin{cases} \sin^{-1}(1/\eta_0) & \text{soft polarization} \\ \sin^{-1}(\eta_0) & \text{hard polarization} \end{cases}$$

$$\theta_n = \begin{cases} \sin^{-1}(1/\eta_n) & \text{soft polarization} \\ \sin^{-1}(\eta_n) & \text{hard polarization} \end{cases}$$

where η_0 and η_n are the impedances of the "0" and "n" faces normalized with respect to the free-space impedance.

The UTD diffraction coefficient for the impedance wedge was originally developed by Tiberio, et al. [12] from Maliuzhinets' wedge solution [14]. Griesser and Balanis [13] revised the coefficient to make it computationally tractable. The coefficient of [13] is for finite, non-zero surface impedances and for cylindrical-wave incidence. In this work, the coefficient is simplified for the specific case of plane-wave incidence, far-field observation, and an

"n" face with $\eta_n=0$ (*i.e.* the "n" face is a perfect electric conductor).

The original diffraction coefficient of [13] is:

$$D(d,\psi',\psi,\theta_0,\theta_n,n) = \left(-\frac{e^{-j\pi/4}}{2n\sqrt{2\pi k}} \right) \tag{9}$$

$$\times \left[\frac{\Psi\left(-\pi+\frac{n\pi}{2}-\psi\right)}{\Psi\left(\frac{n\pi}{2}-\psi'\right)} \frac{\sin\left(\frac{\psi'}{n}\right)+\sin\left(\frac{\theta_0}{n}\right)}{\sin\left(\frac{\psi+\pi}{n}\right)+\sin\left(\frac{\theta_0}{n}\right)} \cot\left(\frac{\pi+\beta^-}{2n}\right) F\left(kd(1+\cos(\beta^--2n\pi N\pm))\right) \right.$$

$$+ \frac{\Psi\left(\pi+\frac{n\pi}{2}-\psi\right)}{\Psi\left(\frac{n\pi}{2}-\psi'\right)} \frac{\sin\left(\frac{\psi'}{n}\right)+\sin\left(\frac{\theta_0}{n}\right)}{\sin\left(\frac{\psi-\pi}{n}\right)+\sin\left(\frac{\theta_0}{n}\right)} \cot\left(\frac{\pi-\beta^-}{2n}\right) F\left(kd(1+\cos(\beta^--2n\pi N_-))\right)$$

$$+ \frac{\Psi\left(-\pi+\frac{n\pi}{2}-\psi\right)}{\Psi\left(\frac{n\pi}{2}-\psi'\right)} \frac{\sin\left(\frac{\psi'}{n}\right)-\sin\left(\frac{\theta_0}{n}\right)}{\sin\left(\frac{\psi+\pi}{n}\right)+\sin\left(\frac{\theta_0}{n}\right)} \cot\left(\frac{\pi+\beta^+}{2n}\right) F\left(kd(1+\cos(\beta^+-2n\pi N_+^+))\right)$$

$$\left. + \frac{\Psi\left(\pi+\frac{n\pi}{2}-\psi\right)}{\Psi\left(\frac{n\pi}{2}-\psi'\right)} \frac{\sin\left(\frac{\psi'}{n}\right)-\sin\left(\frac{\theta_0}{n}\right)}{\sin\left(\frac{\psi-\pi}{n}\right)+\sin\left(\frac{\theta_0}{n}\right)} \cot\left(\frac{\pi-\beta^+}{2n}\right) F\left(kd(1+\cos(\beta^+-2n\pi N_+^-))\right) \right]$$

For plane-wave incidence, far-field observation, the Fresnel transition functions, $F(x)$, in Eq. (9) can be set to 1. $\Psi(z)$ is the auxiliary Maliuzhinets function, which can be expressed in terms of Maliuzhinets functions, $\Psi_n(z)$, as [14]:

$$\Psi(z) = \left[\Psi_n(\pi/2)\right]^4 \cos\left(\frac{z+(n\pi/2)-\theta_0}{2n}\right) \cos\left(\frac{z-(n\pi/2)+\theta_n}{2n}\right) \tag{10}$$

$$\times \frac{\Psi_n\left(z+(n\pi/2)-(\pi/2)+\theta_0\right) \Psi_n\left(z-(n\pi/2)+(\pi/2)-\theta_n\right)}{\Psi_n\left(z+(n\pi/2)-(\pi/2)-\theta_0\right) \Psi_n\left(z-(n\pi/2)+(\pi/2)+\theta_n\right)}$$

$\Psi_n(z)$ can be numerically integrated. The procedure for this is outlined in [13]. For hard polarization, using Eq. (10) and $\theta_n=0$ for a perfectly electrically conducting "n" face, Eq. (9) can be simplified to:

22

$$D\left(\psi',\psi,\theta_0^h,n\right) = \left[-\frac{e^{-j\pi/4}}{2n\sqrt{2\pi k}}\right]\left[\frac{1}{\cos\left(\frac{\psi'}{2n}\right)\sin\left(\frac{\psi'+\theta_0^h}{2n}\right)}\right] \tag{11}$$

$$\times \frac{\Psi_n\left(-(\pi/2)+n\pi-\psi'-\theta_0^h\right)}{\Psi_n\left(-(\pi/2)+n\pi-\psi'+\theta_0^h\right)}$$

$$\times \left\{\frac{\Psi_n\left(-(3\pi/2)+n\pi-\psi+\theta_0^h\right)}{\Psi_n\left(-(3\pi/2)+n\pi-\psi-\theta_0^h\right)}\frac{\cos\left(\frac{\pi+\psi}{2n}\right)}{\cos\left(\frac{\pi+\psi-\theta_0^h}{2n}\right)}\right.$$

$$\times \left[\cos\left(\frac{\psi'-\theta_0^h}{2n}\right)\sin\left(\frac{\psi'+\theta_0^h}{2n}\right)\cot\left(\frac{\pi+\beta^-}{2n}\right) + \sin\left(\frac{\psi'-\theta_0^h}{2n}\right)\cos\left(\frac{\psi'+\theta_0^h}{2n}\right)\cot\left(\frac{\pi+\beta^+}{2n}\right)\right]$$

$$+ \left\{\frac{\Psi_n\left((\pi/2)+n\pi-\psi+\theta_0^h\right)}{\Psi_n\left((\pi/2)+n\pi-\psi-\theta_0^h\right)}\frac{\cos\left(\frac{\pi-\psi}{2n}\right)}{\cos\left(\frac{\pi-\psi+\theta_0^h}{2n}\right)}\right.$$

$$\left.\times\left[\cos\left(\frac{\psi'-\theta_0^h}{2n}\right)\sin\left(\frac{\psi'+\theta_0^h}{2n}\right)\cot\left(\frac{\pi-\beta^-}{2n}\right)+ \sin\left(\frac{\psi'-\theta_0^h}{2n}\right)\cos\left(\frac{\psi'+\theta_0^h}{2n}\right)\cot\left(\frac{\pi-\beta^+}{2n}\right)\right]\right\}$$

where $\beta^{\pm}=\psi\pm\psi'$. Using the above coefficient is much more computationally speedy than the previous solutions to the coated strip problem which report were reported in [1] - [3] because the number of Maliuzhinets function in the coefficient has been reduced from 12 to 6.

Computational results are compared to measurements in Figs. 12 and 13 for a plate with a coating of thickness t=0.0423λ with material parameters μ_{r0}=1.539-j1.2241 and ε_{r0}=11.826-j0.16639. The plate dimensions are 2λ × 2λ. The measurements were made at 10 GHz. The computed hard polarization results are obtained using Eqs. (8b) and (11). In Fig. 12, the computed results are obtained using:

$$\eta_0 = \sqrt{\frac{\mu_{r0}}{\varepsilon_{r0}}} \tag{12a}$$
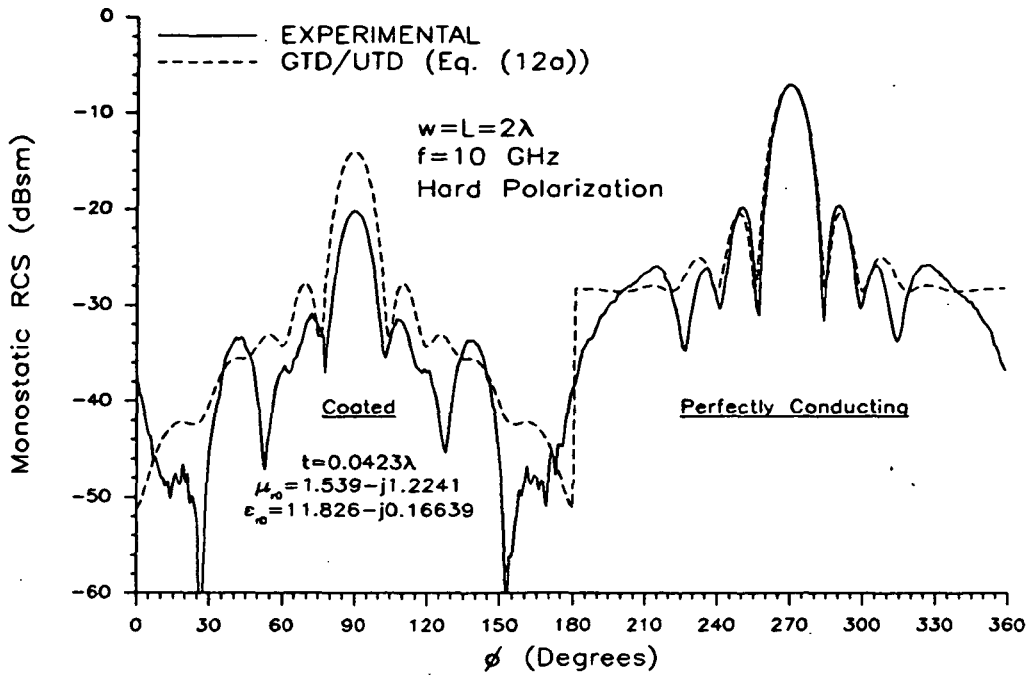
Fig. 12. Principal—plane, monostatic RCS of a coated plate.
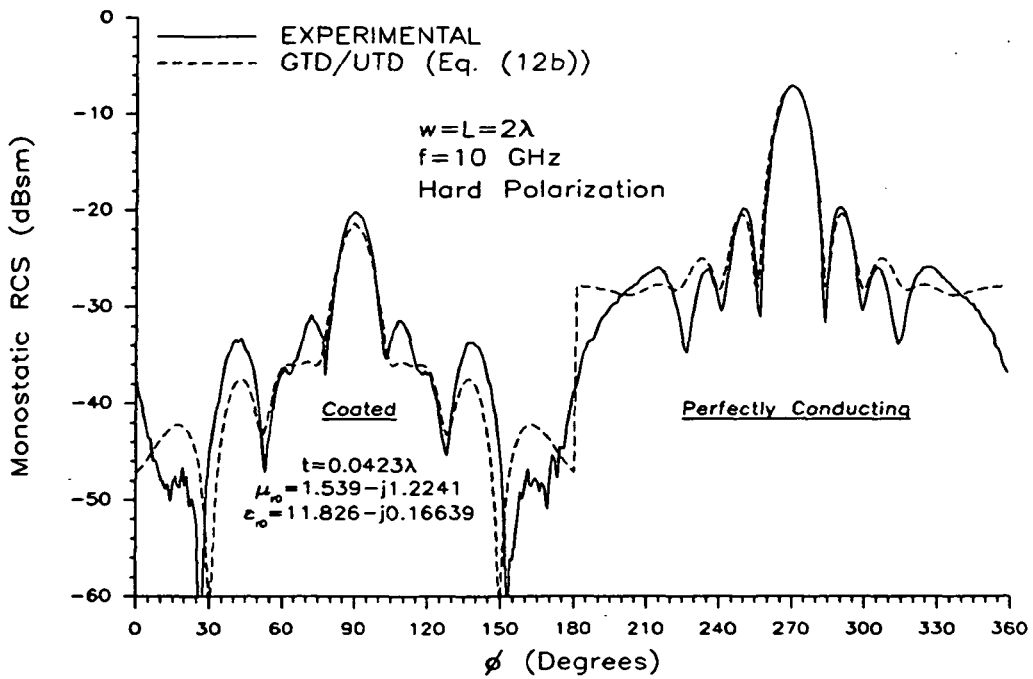
Fig. 13. Principal—plane, monostatic RCS of a coated plate.

where μ_{r0} and ε_{r0} are the relative permeability and relative permittivity, respectively, of the "0" face. In Fig. 13, η_0 is approximated using the shorted-transmission-line equivalent impedance for normal incidence:

$$\eta_0 = j \sqrt{\frac{\mu_{r0}}{\varepsilon_{r0}}} \, \tan\left(2\pi \sqrt{\mu_{r0}\varepsilon_{r0}} \, t\right) \qquad (12b)$$

where t is in free-space wavelengths. The results of Fig. 13, using the η_0 of Eq. (12b) are much better than those of Eq. (12a). Although the diffraction coefficient of Eq. (11) accounts for the perfectly conducting face of the wedge, it is necessary to use the shorted-transmission-line approximation of Eq. (12b) to account for the effect of the perfectly conducting backing on the coating impedance. The discontinuity at $\phi=180°$ occurs because surface waves are not included in the model. Future work will involve revising the model to include the surface-wave terms. In addition, higher-order terms will be added to better predict the side lobes.

III. FUTURE WORK

Future work will involve finalizing the model for the coated strip/plate in order to provide a comprehensive analysis as was presented in this report for the perfectly conducting strip/plate. Surface-wave and higher-order diffraction terms will be added to the present model. Nonprincipal-plane scattering from the coated plate will also be considered. Furthermore, research will continue on the nonprincipal-plane scattering from the perfectly conducting plate,

which has been the topic of previous reports. Questions concerning higher-order and corner diffractions still remain. Research will also continue on the subject of impedance coatings. Finally, the coated dihedral corner reflector model of [18] will be revised to better account for a finite-thickness lossy coating on top of a perfectly conducting surface.

IV. PUBLICATIONS

During this reporting period two papers were submitted to the *IEEE Transactions on Antennas and Propagation* for consideration for publication. The work reported in these papers was supported by this NASA grant. The papers were as follows:

[a] Lesley Anne Polka and Constantine A. Balanis, "Measurements and a method of equivalent currents model for nonprincipal-plane scattering from a rectangular plate," submitted for publication in *IEEE Trans. Antennas Propagat.*

[b] Lesley Anne Polka and Constantine A. Balanis, "Measurements and theory for strip and narrow plate scattering at and near grazing angles," submitted for publication in *IEEE Trans. Antennas Propagat.*

V. REFERENCES

[1] C. A. Balanis and L. A. Polka, "High-frequency techniques for RCS prediction of plate geometries," Semiannual Report, Grant No. NAG-1-562, National Aeronautics and Space Administration, Langley Research Center, Hampton, VA, Jul. 31, 1991.

[2] ——, "High-frequency techniques for RCS prediction of plate geometries," Semiannual Report, Grant No. NAG-1-562, National Aeronautics and Space Administration, Langley Research Center, Hampton, VA, Jan. 31, 1991.

[3]   C. A. Balanis, L. A. Polka, and K. Liu, "Scattering from coated structures and antenna pattern control using impedance surfaces," Semiannual Report, Grant No. NAG-1-562, National Aeronautics and Space Administration, Langley Research Center, Hampton, VA, Jul. 31, 1990.

[4]   ——, "Nonprincipal-plane scattering from rectangular plates and pattern control of horn antennas," Semiannual Report, Grant No. NAG-1-562, National Aeronautics and Space Administration, Langley Research Center, Hampton, VA, Jan. 31, 1990.

[5]   ——, "Nonprincipal-plane scattering from flat plates — second-order and corner diffraction and pattern control of horn antennas," Semiannual Report, Grant No. NAG-1-562, National Aeronautics and Space Administration, Langley Research Center, Hampton, VA, Jul. 31, 1989.

[6]   ——, "Nonprincipal plane scattering of flat plates and pattern control of horn antennas," Semiannual Report, Grant No. NAG-1-562, National Aeronautics and Space Administration, Langley Research Center, Hampton, VA, Jan. 31, 1989.

[7]   J. B. Keller, "Geometrical theory of diffraction," J. Opt. Soc. Amer., vol. 52, pp. 116-130, Feb. 1962.

[8]   R. G. Kouyoumjian and P. H. Pathak, "A uniform geometrical theory of diffraction for an edge in a perfectly conducting surface," Proc. IEEE, vol. 62, pp. 1448-1461, Nov. 1974.

[9]   A. Michaeli, "A uniform GTD solution for the far-field scattering by polygonal cylinders and strips," IEEE Trans. Antennas Propagat., vol. AP-35, pp. 983-986, Aug. 1987.

[10]   ——, "A new asymptotic high-frequency analysis of electromagnetic scattering by a pair of parallel wedges: closed form results," Radio Science, vol. 20, pp. 1537-1548, Nov. - Dec. 1985.

[11]   ——, "A closed form physical theory of diffraction solution for electromagnetic scattering by strips and 90° dihedrals," Radio Science, vol. 19, pp. 609-616, Mar. - Apr. 1984.

[12]   R. Tiberio, G. Pelosi, and G. Manara, "A uniform GTD formulation for the diffraction by a wedge with impedance faces," IEEE Trans. Antennas Propagat., vol. AP-33, pp. 867-873, Aug. 1985.

[13]   T. Griesser and C. A. Balanis, "Reflections, diffractions, and surface waves for an impedance wedge of arbitrary angle," IEEE Trans. Antennas Propagat., vol. AP-37, Jul. 1989.

[14]   G. D. Maliuzhinets, "Excitation, reflection and emission of surface waves from a wedge with given face impedances," Sov. Phys. Doklady, vol. 3, pp. 752-755, Jul./Aug. 1958.

[15] R. A. Ross, "Radar cross section of rectangular flat plates as a function of aspect angle," *IEEE Trans. Antennas Propagat.*, vol. AP-14, pp. 329-335, May 1966.

[16] P. H. Pathak, "Techniques for high frequency problems," in *Antenna Handbook: Theory, Applications, and Design*, Y. T. Lo, S. W. Lee, Eds. New York: Van Nostrand Reinhold, 1988.

[17] C. A. Balanis, *Advanced Engineering Electromagnetics*. New York: John Wiley & Sons, 1989.

[18] T. Griesser, C. A. Balanis, and K. Liu, "RCS analysis and reduction for lossy dihedral corner reflectors," *Proc. IEEE*, vol. 77, pp. 806-814, May 1989.

NAG-1-1037

IN-05-CR,

PART 2

69293
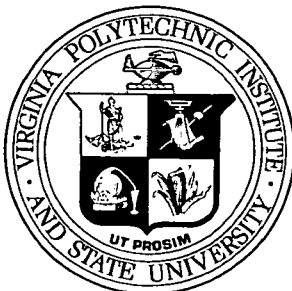
P 86

COLLEGE
OF
ENGINEERING

VIRGINIA
POLYTECHNIC
INSTITUTE
AND
STATE
UNIVERSITY

Hi-Alpha Forebody Design: Part II
Determination of Body Shapes for
Positive Directional Stability

by

R. Ravi and William H. Mason

VPI-Aero-182 (rev.,)

October 22, 1991
(rev., February 2, 1992)

Prepared for:

Department of Aerospace And Ocean Engineering
Virginia Polytechnic Institute and State University
Blacksburg, VA 24061

TABLE OF CONTENTS

LIST OF TABLES

LIST OF FIGURES

HI-ALPHA FOREBODY DESIGN: PART II
DETERMINATION OF BODY SHAPES FOR POSITIVE STABILITY

R. Ravi
William H. Mason

Virginia Polytechnic Institute and State University

SUMMARY

Computational Fluid Dynamics (CFD) has been used to study aircraft forebody flowfields at low speed high angle-of-attack conditions with sideslip. The purpose is to define forebody geometries which provide good directional stability characteristics under these conditions. The flows over the experimentally investigated and previously computed by the authors F-5A forebody and Erickson forebody were recomputed with better and refined grids. The results were obtained using a modified version of cfl3d to solve either the Euler equations or the Reynolds equations employing a form of the Baldwin-Lomax turbulence model. Based on those results, we conclude that current CFD methods can be used to investigate the aerodynamic characteristics of forebodies to achieve desirable high angle-of-attack characteristics. An analytically defined generic forebody model is described, and a systematic study of forebody shapes was then conducted to determine which shapes promote a positive contribution to directional stability at high angle-of-attack. A novel way of presenting the results is used to illustrate how the positive contribution arises. Based on the results of this initial parametric study, some guidelines for aerodynamic design to promote positive directional stability are presented.

INTRODUCTION

Current and future fighter aircraft will be operating at high angles-of-attack where the flowfields are dominated by large regions of separated vortical flows. Considerable research is being done both in the experimental and computational areas to understand the physics of such complex flows. A good understanding of these flows would enable the aircraft designer to design fighter aircraft to achieve better maneuverability at high angles-of-attack. At high angle-of-attack the forebody aerodynamic characteristics make significant contributions to the complete configuration aerodynamics. The surveys by Chambers (Ref. 1) and Chambers and Grafton (Ref. 2) present the basis of the current understanding of high angle-of-attack aerodynamics.

One of the specific characteristics of interest is directional stability. For the F-5A, which has good high angle-of-attack characteristics, it has been shown experimentally (Ref. 3) that the forebody makes a significant positive contribution to directional stability at angles-of-attack above which the vertical tail ceases to be effective. That forebody had a smooth cross section, although it was not axisymmetric. The current authors recently demonstrated that the experimental results could also be predicted using Computational Fluid Dynamics (CFD) methods (Refs. 4 and 5). The ability to reproduce previously obtained experimental results meant that it would be valid to use CFD to try to design shapes for specific aerodynamic characteristics at high angle-of-attack, where large regions of separated flow are present.

Future advanced fighters are likely to possess chine type forebodies, as evidenced by the YF-22 and YF-23 configurations. For these aircrafts high levels of agility are demanded, and the aerodynamic characteristics at high angle-of-attack play an important role in determining aircraft handling qualities and agility.

Because of the interest in chine-shaped forebodies, a key issue in the application of computational methods to forebody design is the ability to treat chine sectional shapes. Few general chine-shaped forebody wind tunnel tests are available to use for comparison with computational

2

methods. One is the wind tunnel investigation conducted by Erickson and Brandon (Ref. 6, the "Erickson Forebody"). In that study the chine effects were investigated for a generic fighter configuration, and pressure distributions were measured on the chine forebody. All forebody results were acquired in the presence of the wing. More recently Kegelman and Roos (Refs. 7 and 8) studied experimentally the influence of cross-sectional shape on the vortex flowfield at high alpha. They compared the surface pressures and the aerodynamic loads between a circular, elliptical and a chined cross section at high angles of attack. Hall (Ref. 9) studied the influence of the forebody cross-sectional shape on wing vortex-burst location. This study also involved the comparison of a two chine cross-sections with a circular section.

The results were obtained using **cfl3d** (Ref. 10) to solve either the Euler equations or the Reynolds equations employing a form of the Baldwin-Lomax turbulence model. Version 1.1 of the code with the modifications as described in Ref. 5 was used in all the computations.

In this report we first repeat the results obtained on the F-5A forebody (Ref. 4) using a grid better suited to the geometry to assess possible sensitivity of the previous results to the grid. Secondly, we compare computed predictions with the experimental data for the "Erickson Forebody" at $\alpha = 30°$ ($5°$ and $10°$ sideslip)and at $\alpha = 40°$ ($10°$ sideslip). The above two cases were used to establish a methodology base for analysing generic cross-sectional forebodies.

A generic forebody which can be used to systematically study forebody aerodynamics for families of forebody shapes at high alpha is proposed. Using this model, a computational study is carried out to determine which shapes lead to the best directional stability characteristics. The reference parameters used in computing the forces and moments for the cases studied in this report are presented in Table 1. The report concludes with some guidelines for high angle-of-attack forebody design.

LIST OF SYMBOLS

a	maximum half breadth of the generic forebody definition
b	maximum centerline of the generic forebody definition
b'	wingspan
c	mean aerodynamic chord
C_L	lift-force coefficient, lift/$q_\infty S_{ref}$
C_n	yawing-moment coefficient, yawing moment/$q_\infty S_{ref} b'$
$C_{n\beta}$	directional stability derivative, $\partial C_n / \partial \beta$
C_p	pressure coefficient, $(p-p_\infty)/q_\infty$
C_y	side-force coefficient, side-force/$q_\infty S_{ref}$
c_y	local side-force, section side-force/$q_\infty S_{ref}$
FS	fuselage station
m,n	adjustable parametric coefficients
M_∞	free stream Mach number
l	model length
Re_l	Reynolds number based on model length, l
S_{ref}	reference area
u^*	wall friction velocity, $\sqrt{\tau_w / \rho}$
V_{sep}	cross flow velocity magnitude at separation point (chine edge)
x,y,z	body coordinate system : x positive aft along model axis, y positive to right and z positive up
XN	distance from the tip of the nose to the station where the planform span becomes a constant.
y^+	inner law variable, yu^*/v
α	angle of attack, deg
β	angle of sideslip, deg
ΔC_p	difference between leeward and windward C_p across the vertical plane of symmetry

4

F-5A FOREBODY

The wind tunnel experiment demonstrating the dominant contribution of the F-5A forebody to directional stability at high angle-of-attack was simulated computationally in the first phase of this work (Ref. 5). This forebody had been tested by Sue Grafton, et.al. at NASA Langley Research Center and the results are available in Ref. 3. The geometry math model and the comparison with the wind tunnel model was described in detail in Ref. 5. In that study the grid was constructed from two dimensional O-type cross flow grids which are longitudinally stacked, constituting a single block H-O topology as shown in fig. 1. It is difficult to resolve the flow details near the nose using an H-O topology. Hence, we investigated the same geometry using an alternate grid system to assess possible grid effects on the results.

F-5A Grid Details

The inviscid calculations on the F-5A (Ref. 5) were repeated on the new grid shown in fig. 2. This grid consists of two blocks, where the first block used a C-O topology to improve the grid resolution at the nose. This grid was generated using a transfinite interpolation grid generator provided by Ghaffari (Ref. 11). The first block extends from the nose to the point where the flat sidewall starts *i.e.*, 14.025 inches from the nose, as explained in Ref. 5. The inviscid calculations were performed on a grid which used 32 axial, 93 circumferential and 45 radial points (32 x 93 x 45). The outer boundary extends 32.7 inches radially outward and is comparable to the length of the forebody which was 31.02 inches. The second block used the previous H-O grid topology with 13 axial, 93 circumferential and 45 radial points (13 x 93 x 45). The C-O grid generator used for the first block requires a user specified normal distance to the first grid point and the distance of the outer boundary as the input. The H-O grid generator used for the second block uses the distance of outer boundary and a stretching parameter as the input. Care was taken to ensure that

5

the distance of the first grid normal to the surface is the same for both the blocks at the interface.

Figures 3 and 4 show the grid used for inviscid calculations at different cross-sections downstream from the nose. Figure 3(a) shows the entire cross-sectional grid at FS 14.02 and fig. 3(b) shows the details near the body at the same station. Figures 4(a) and 4(b) contain the same information at FS 29.61. Because of the presence of the flat sidewall at sections downstream, the grid points were clustered near the maximum half breadth points forward of the flat sidewall. This provided adequate definition of the flat wall portion of the forebody.

A grid refinement study was done for both inviscid and turbulent solutions for an angle-of-attack of $40°$. The grids used in this study were the same stacked grids used in the first phase of this work (Ref. 5). The baseline inviscid grid had 33 (axial), 93 (circumferential) and 45 points in the radial direction. The baseline viscous grid had 33 (axial), 93 (circumferential) and 65 points in the radial direction. During the grid refinement study, the number of points in the radial direction were increased with improved radial stretching, so that at least four fine grid points were present in the first grid point of the crude grid. The circumferential and axial densities were kept the same. The inviscid refined grid had 90 points in the radial direction while the refined viscous grid had 100 points radially.

Results and Discussion of Computations on the F-5A Forebody

Inviscid calculations were performed for $\alpha = 30°$ and $\beta = 5°$ to compare the results of this new grid system with those obtained using a stacked grid earlier in Ref. 5. The boundary conditions were the same in both the cases except on the axis that runs from the nose to the upstream farfield boundary where a singularity type boundary condition was imposed for the new grid. In the earlier computations this boundary was a part of the surface and so an inviscid boundary condition was imposed.

Figures 5 and 6 show the comparison of the inviscid surface pressures between the two grid

systems at FS 6.58 and FS 26.77 respectively. It is very difficult to identify a difference between the two results at these stations. A comparison of the longitudinal variation of C_p on the leeward plane is shown in fig. 7. This figure shows the improved resolution of the solution near the nose with the new C-O grid. There was negligible change in the value of the directional stability C_{n_β}

A detailed study of the results obtained with the stacked grid was also performed. Figure 8 shows the sign convention used in computing the side-force and yawing moment. The F-5A forebody experimental directional stability data from Ref. 3 are shown along with the computed inviscid and viscous results in fig. 9. The computed results revealed the same trend found in the wind tunnel data and were already presented in Refs. 4 and 5. Additionally, we show the results obtained with the refined grid for both inviscid and turbulent cases at $\alpha = 40°$. Although the results changed slightly with grid resolution, the trends were the same in both the cases.

Figure 10 shows the axial distribution of side-force contributing to the yawing moment presented in fig. 9 at $\alpha = 40°$. The importance of the viscosity in producing the positive stability is clearly demonstrated. The viscous solution develops a significant restoring force, with a positive side-force over most of the forebody and generally increasing with downstream distance. This is a consequence of the increasing asymmetry of the forebody vortices with distance from the nose. The inviscid solution shows essentially no side-force over the majority of the forebody. Figures 11 and 12 provide the circumferential pressure distributions at two stations for both inviscid and turbulent cases. The corresponding cross-sectional shape, the direction of incoming flow and the origin of reference for the angular measure are shown below each of these figures. The negative peak pressures are due to the vortices on the upper surface of the cross section and are shown more clearly in the following flow visualization pictures to be presented in fig. 14. The asymmetry in the pressure distribution due to the sideslip can be seen in fig. 11, and is much more noticeable in fig. 12. At FS 14.02 the viscous solution results clearly show the effect of the vortices, with two low pressure regions, denoted B and C, underneath the vortices. The low pressure peaks A and D are due to the flow around the highly curved sides of the body. At station FS 29.61 the inviscid results contain four distinct low pressure peaks corresponding to the high curvature regions at the

7

cross-section corners. Considering viscous effects, the turbulent flow is massively separated and the primary vortices are moving away from the body. The small low pressure peak at C in fig. 12 is due to the secondary vortex, as shown in fig. 14 The inviscid results contain low pressure regions that are due to the distinct corners in the cross section (high cross-section curvature).

Figure 13 contains the pressure differences, ΔC_p, between the leeward and windward sides of the body at the same stations at which the pressures were plotted in figs. 11 and 12. These provide insight into the distribution of side-force at a particular station to help explain the effect of viscosity in creating the restoring force. Although the viscous effects are primarily associated with the vortex and separated flowfield on the top side of the forebody, the effects of viscosity are seen to alter the balance of pressures between the sides of the body over most of the side projection. It is particularly interesting to notice that the near zero side-force associated with the inviscid flow arises as a delicate balance between a side-force in one direction on the lower portion of the body, and a side-force in the opposite direction on the upper part. The effects of viscosity are to reduce the magnitudes of the peak effects as well as producing a shift which results in a distribution which has a much larger net side-force.

Figures 14(a) and 14(b) show the cross-sectional stagnation pressure contours at axial stations $x = 14.02$ inches and $x = 29.61$ inches from the nose for the viscous calculation at the same flow conditions shown in figs. 11 and 12. The incoming flow is the same as shown in figs. 11(b) and 12(b). The leeward (LHS) vortex is farther away from the surface than the windward (RHS) vortex. The asymmetry of the low pressures on the body under the vortices is generally considered to be pulling the body to smaller sideslip, and thus provides a stabilizing moment. However, we have shown in fig. 13 that the side-force is affected by the separated flow indirectly through its effect on the pressure distribution over virtually the entire surface. These local effects of the vortices actually act primarily on the essentially flat top-surface and don't directly contribute to the side-force. At FS 29.61 we can also see the secondary vortices under the primary vortices.

Figures 15 and 16 show the inviscid and turbulent calculation pressures at FS 14.02 and FS 29.61 plotted as vectors perpendicular to the surface. In these diagrams, the surface is treated as a line of zero pressure and the vectors going outward from the surface represent negative pressure coefficients. These diagrams should be studied in conjunction with pressure plots of fig. 11 and 12. At FS 14.02 the viscous diagrams show clearly the effect of the vortices resulting in two low pressure peaks on the upper surface. At FS 29.61, the inviscid results show two peaks as the flow accelerates around the corners on the upper surface. However, the viscous flow calculation separates closer to the windward plane on the leeward side and the peak is almost insignificant. On the windward side, as expected, the flow separates away from the windward plane and the low pressure peak is therefore still visible. The intermediate peak in this case is because of the secondary vortex.

Figure 17 shows the vortex path development along the body. The leeward vortex (here on the RHS of the body) is seen to be rising above the body much faster than the windward vortex (LHS). The windward vortex is actually "blown back" over the forebody, and is moving along the top surface near the center. This is also evident from fig. 14.

ERICKSON CHINE FOREBODY

Erickson and Brandon experimentally investigated the chine effects on a generic fighter configuration and have published the detailed pressure data over a large range of angles of attack and sideslip (Ref. 6). This flowfield on such a model was computationally investigated in the earlier part of this work and the details were presented in Ref. 5. The geometry math model and the comparison with the wind tunnel model was also described in detail there. In that study, the grid was constructed from two dimensional O-type cross flow grids which are longitudinally stacked, constituting a single block H-O topology as was done earlier in the case of F-5A. Here we investigate the same geometry using an alternate grid system and also study the grid resolution requirements for a chined forebody.

9

Erickson Forebody Grid Details

The inviscid calculations on the Erickson forebody were repeated on the alternate C-O grid shown in fig. 18. The baseline inviscid calculation grid had 45 points in the radial direction and 101 points in the full circumferential direction. Longitudinally, the grid was clustered near the nose with 25 stations on the forebody as shown in fig. 18. The axial grid planes were defined at stations corresponding to the experimental measured stations. These were at a distance of 7.19, 13.56 and 19.94 inches from the nose along the length of the body. The smoothing of the surface unit normals introduced some grid skewness near the chine nose as well as around the chine edge. This was done to avoid large cell volume discontinuities.

As compared to the inviscid solution grid, the viscous calculation used a grid with 65 points in the radial direction, and with longitudinal and circumferential grid points remaining identical with the grid used for the inviscid calculations. The baseline grid was established with sufficient normal clustering near the surface to adequately resolve the laminar sublayer in the turbulent boundary layer flow. This grid produced an average normal cell size of approximately $10^{-4}l$. At the wind tunnel freestream conditions for the Erickson forebody ($M_\infty = 0.2$, $Re_l = 1.02 \times 10^6$ based on model length, and $\alpha = 20°$) the baseline grid typically resulted in a value of $y^+ \approx 2$ at the first mesh point above the surface.

Figure 19 shows the grid used for inviscid calculations at the last section downstream from the nose. Figure 19(a) shows the entire cross-sectional grid at FS 14.02 and figs. 19(b) and 19(c) provide the details near the surface and chine edge respectively.

A grid refinement study was done with both the inviscid and turbulent grids. In each of these cases the number of grid points were doubled in the normal direction with increased clustering in the normal direction. The circumferential and axial densities were kept the same. Approximately four fine grid points were packed in the first cell of the baseline grid for both the fine inviscid and the fine turbulent grids. The fine Navier-Stokes grid provided a y^+ value of approximately 0.5.

Results and Discussion of Computations on the Erickson Forebody

Inviscid calculations were performed for $\alpha = 30°$ and $\beta = 0°$ to compare the results of this new grid system with those obtained using a stacked grid earlier in Ref. 5. The stacked grid used earlier had 33 axial stations with 25 on the surface and 8 ahead of the nose. The radial and circumferential densities were the same. As in the case of F-5A, the boundary condition on the axis that runs from the nose to the upstream farfield boundary was altered to a singularity type boundary condition. In the earlier computations this boundary was a part of the surface and so an inviscid boundary condition was imposed.

Figures 20 and 21 show the comparison of the inviscid surface pressures between the two grid systems at FS 7.19 and FS 13.56 respectively. The difference is almost insignificant as was seen in the case of F-5A. The advantage of using this grid system is that you can maintain the same grid density on the surface while reducing the number of axial stations.

Figures 22 - 24 present the computed upper surface pressure distributions at three stations obtained on the isolated forebody along with experimental data on the forebody-wing model for various angles of attack and sideslip. The details of the experimental investigation are available in Ref. 6. Figure 22 shows the upper surface pressures for the $\alpha = 30°$ and $\beta = 5°$ case. At the section closest to the nose (FS 7.19) the inviscid computations predict the pressures very close to the experimental values. At stations further downstream the agreement deteriorates. At FS 19.94 the wind tunnel data appears to reflect the higher local incidence induced by the wing flowfield. The inviscid refined grid results show a suction peak in slightly better agreement than the baseline grid at the first station, but provide no improvement further downstream. Turbulent viscous effects do not change the pressure levels at the mid section of the forebody, but do have some effect on the peak suction pressure level. The peak suction pressures were reduced, as expected, resulting in poorer agreement with the experimental data. In the turbulent flow case the refined grid solution resulted in only minor changes in the pressure distribution. The trend remains the same when the

11

sideslip is increased to 10° as shown in fig. 23. Figure 24 shows the pressures for $\alpha = 40°$ and $\beta = 10°$. Erickson and Brandon (Ref. 6) suggest that the extent of upstream influence of vortex breakdown occurring downstream was found to differ at different combinations of angles of attack and sideslip. For example, vortex core bursting had occurred at $\alpha = 40°$ whenever the sideslip angle exceeded 5°. The computations neither model the wing effects or vortex burst effects.

Figure 25 shows the side-force computed for the Erickson forebody. Both the inviscid and the viscous solutions show similar trends, and the minor grid effects indicate that the solutions are grid resolved. Here, in contrast to the smooth forebody cross-section results for the F-5A, both inviscid as well as the turbulent results develop restoring forces, with a positive side-force over most of the forebody and generally increasing with downstream distance. This is expected because of the fixed separation lines along the edge of the chine, regardless of viscosity, and is in marked contrast to the smooth cross-section results obtained on the F-5A forebody (Ref. 4). There the inviscid and viscous solutions were completely different, with the inviscid solution providing essentially no side-force. The vortical flow in this case is being governed essentially by inviscid phenomena. The directional stability characteristics in fig. 26 show the stabilizing effect of the chined forebody over the entire range from 20° to 40° angle-of-attack. Qualitatively, the trend shown by both Euler and Navier-Stokes grids are very similar. This observation is important, and provides a basis for deciding on the solution strategy to be used for the parametric computations on a generic forebody to be discussed later.The directional stability computed for this forebody is similar using either Euler or Navier-Stokes solutions at 30° angle of attack. At $\alpha = 40°$, the refined Navier-Stokes grid calculation resulted in improved correlation with Euler results.

Figures 27 and 28 show the inviscid and turbulent calculation pressures at FS 7.19 and FS 19.94 plotted as vectors perpendicular to the surface. As before, the surface is treated as a line of zero pressure and the vectors going outward from the surface are proportional to the negative pressures. These diagrams should be studied in conjunction with pressure plots of fig. 23. Unlike the case of F-5A, the inviscid and turbulent cases are very similar at both the stations because of the fixed separation line as discussed earlier. The flow decelerates as it approaches the chine edge

because of the change of the body cross-sectional shape, and separates at the chine edge.

Figures 29 and 30 show inviscid and turbulent stagnation pressure contours respectively at two different stations. These clearly show the chine-edge generated vortices. The position and magnitude of the primary vortices are nearly identical in both the inviscid and turbulent cases. The turbulent solution also shows the formation of secondary vortices near the chine edge due to boundary layer separation. For chine shapes the effects of viscosity are a secondary effect on vortex size, position and strength. Strong vortex formation can be seen all along the forebody in fig. 31 with the leeward vortices rising above the surface much faster than the windward vortices. Such strong vortex formation on bodies with sharp chines is responsible for positive directional stability even at 20° angle of attack which was not found in the F5-A case.

SOLUTION STRATEGY FOR PARAMETRIC FOREBODY GEOMETRY STUDY

Based on the analysis of the computational solutions obtained on the Erickson chine forebody, a solution strategy for forebody shaping study was chosen. When β was fixed at 5° it was shown in the case of the Erickson chine forebody that the inviscid pressures were very close to the experimental data and the side-force and C_{n_β} trends were qualitatively similar and nearly the same for the Euler and turbulent flow computations. Though refining the grid made a slight improvement in the Euler results, it was very expensive considering the minor change in the results. Hence, it was decided that to assess aerodynamic trends arising from forebody geometry variations on chine-shaped forebodies, the computations could be done using the Euler equations and the baseline grid.

To study the advantage of using multigrid and multisequencing, the inviscid flow over a generic analytical forebody was computed at $\alpha = 30°$ and $\beta = 5°$. Three levels of sequencing were used with multigridding on each level. The surface pressures as shown in fig. 32 were identical when the residual went down to the same order of magnitude in both cases. However,

13

there was a 33% reduction in CPU time. After this approach was established, the remaining Euler calculations were performed with three levels of sequencing and multigridding on each level of sequencing.

GENERIC CHINE FOREBODY STUDY

To study geometric shaping effects on forebody aerodynamic characteristics, an analytical forebody model with the ability to produce a wide variation of shapes of interest was defined in Ref. 5. This generic forebody model makes use of the equation of a super-ellipse to obtain the cross-sectional geometry. The super ellipse, used previously to control flow expansion around wing leading edges (Ref. 12), can recover a circular cross section, produce elliptical cross-sections and can also produce chined-shaped forebodies. Thus it can be used to define a variety of different cross-sectional shapes.

The super-ellipse equation for the forebody cross section was defined in Ref. 5 as:

$$\left(\frac{z}{b}\right)^{2+n} + \left(\frac{y}{a}\right)^{2+m} = 1$$

where n and m are adjustable coefficients that control the surface slopes at the top and bottom plane of symmetry and chine leading edge. The constants a and b correspond to the maximum half-breadth and upper or lower centerlines respectively. Depending on the value of n and m, the equation can be made to meet all the requirements specified above. The case $n = m = 0$ corresponds to the standard ellipse. The body is circular when $a = b$.

When $n = -1$ the sidewall is linear at the maximum half breadth line, forming a distinct crease line. When $n < -1$ the body cross-section takes on the cusped or chine-like shape. The derivative

14

of z / b with respect to y / a is:

$$\frac{d\bar{z}}{d\bar{y}} = -\frac{\left(\dfrac{2+m}{2+n}\right)}{\left[1 - \bar{y}^{(2+m)}\right]^{\left(\frac{1+n}{2+n}\right)}}$$

where $\bar{z} = z / b$ and $\bar{y} = y / a$. As $\bar{y} \to 1$, the slope becomes:

$$\frac{d\bar{z}}{d\bar{y}} = \begin{cases} \infty & n > -1 \\ 0 & n < -1 \\ -(2+m)\bar{y}^{1+m} & n = -1 \end{cases}$$

Different cross-sections can be used above and below the maximum half-breadth line. Even more generality can be provided by allowing n and m to be functions of the axial distance x, although in this study the parameters n and m were taken to be constants with respect to x. The parameters a and b are functions of the planform shape and can be varied to study planform effects. Notice that when $n = -1$ the value of m can be used to control the slope of the sidewall at the crease line.

Using the generic forebody parametric model defined above, and the computational strategy developed based on the Erickson forebody results, an investigation of directional stability characteristics of various chine-shaped forebody geometries was made. It was decided to analyse the effect of changing b/a, chine angle and combinations thereof. This range of cross-sectional shapes provides an extremely broad design space to investigate aerodynamic tailoring of forebody characteristics through geometric design.

For the present study the following cases were initially selected :

(a) Geometrical parameters:

$m = 0$

$-1.5 \leq n \leq -1.0, \quad \Delta n = -0.25$

$$0.5 \leq b/a \leq 1.5, \ \Delta b/a = 0.5$$

(b) Flow conditions:

$$20° \leq \alpha \leq 40°, \ \Delta\alpha = 10°$$

$$0° \leq \beta \leq 5°, \quad \Delta\beta = 5°$$

The resulting cross-sectional shapes are shown in fig. 33. The computational study was carried out to determine the shape which leads to the largest increase in directional stability. This test case matrix, shown in Table 2, resulted in 54 different configurations with symmetrical upper and lower surfaces, showing how large the possible set of cases could be without careful selection. The $\beta = 0°$ cases were included to compare the flow physics with and without sideslip. However, with $C_n = 0$ at $\beta = 0°$ and the number of cases being excessive, the $\beta = 0°$ cases were eliminated. Further combinations were eliminated as the study progressed and the results examined. Some asymmetric upper/lower cross-section geometries were also analysed. These geometries were defined using different b/a or different n for upper and lower surfaces.

It was also decided that the planform shape would initially be defined to be similar to the Erickson chine case and to study the effects of varying cross-section geometry. In this calculation the moment center for the computation of the directional stability was kept fixed at the value used in the Erickson forebody test (Table 1). Based on the best cross-sectional shape, limited planform effects were studied.

Discussion of Results for the Generic Chine Forebodies

Effect of varying b/a

This study was conducted for cross-sectional shapes with $m = 0$ and $n = -1.5$ and $b/a = 0.5$, 1.0 and 1.5. Figure 34 shows C_{n_β} vs angle of attack with b/a as the varying parameter. It is interesting to note that the contribution to positive directional stability increases as b/a decreases.at

16

a fixed angle-of-attack. $b/a = 0.5$ is the best cross-section. An understanding of these results requires an examination of the flowfield details presented below.

Figure 35 shows the variation of the side-force with the axial distance at each angle-of-attack. Near the nose the force is initially destabilizing, being negative for all cases computed. Moving aft from the immediate vicinity of the nose, the trend is reversed and the side-force starts to increase toward positive values. The side-force becomes more positive with increasing angle-of-attack. In general, the side-force becomes increasingly negative as the value of b/a increases, making the body more unstable. However, some crossover occurs at the aft end of the body at the higher α, where the $b/a = 0.5$ case is not as positive as the $b/a = 1$ case.

Figures 36 to 38 show the ΔC_p vs z plots at a typical cross-section ($x = 18.35$). The integration of this pressure difference produces the side-force values presented in the fig. 35. The cross-section below the chine edge always makes a negative contribution to the side-force. Above the chine edge there is an abrupt large positive spike in the side-force. This arises because of the asymmetry in strength and position of the vortices. At $\alpha = 20°$ the shallow $b/a = .5$ case produces a much larger spike than the $b/a = 1.5$ case. At higher α the $b/a = 1$ case has nearly the same size spike.

The asymmetry in the position and strength of the windward and leeward vortices which is responsible for the positive side-force on the forebody is shown in fig. 39 for $\alpha = 30°$ and $b/a = 0.5$ and 1.5. Figure 39(a) shows the minimum static pressure found in the vortex over the length of the body. In this case the lower pressure for the $b/a = 0.5$ geometry is much stronger compared to the $b/a = 1.5$ case. Also, the windward vortex for this geometry is much stronger than the leeward vortex resulting in a larger asymmetry. This corresponds to the large difference in directional stability shown in fig. 34. In the sideview shown in fig. 39(b), for $b/a = 0.5$ both the vortices are farther away from the surface than in the $b/a = 1.5$ case, and they are above the top centerline, allowing communication between the windward and leeward vortices. In the planform view, fig. 39(c), the $b/a = 0.5$ case shows more lateral movement particularly in the aft region than

17

the $b/a = 1.5$ case, where the windward and leeward vortices are separated by the large hump on the upper surface all along the length of the forebody and thus restricting the vortex movement. This is illustrated in fig. 40, which presents stagnation pressure contours to show the increase in vortex movement as b/a decreases

Using these results the physics of chined forebody aerodynamics emerges. A shallow upper surface ($b/a = 0.5$) results in a stronger, more asymmetric vortex system compared to a deep surface ($b/a = 1.5$). A deep lower surface results in a larger negative contribution to directional stability. Hence, higher b/a for the upper or the lower surface is undesirable.

Effect of varying chine angle

In this study b/a was held constant at 0.5 (corresponding to the best result obtained above) and n was varied over -1.5,-1.25 and -1.0, which increases the edge angle from a sharp chine to a straight wall. Recall that theoretically the chine edge has a zero angle when $n = -1.5$ and $n = -1.25$ and therefore has a 180° slope discontinuity. When $n = -1.0$ the included edge angle is finite (127°) and the slope discontinuity is smaller.

The effect of changing the shape parameter n on the directional stability is shown in fig. 41. Essentially, all the results are similar at $\alpha = 20°$ and 30° but show differences at $\alpha = 40°$. The sudden decrease in C_{n_β} for $n = -1.0$ at $\alpha = 40°$ was further investigated by looking at the side-force variation in fig. 42. Based on the results shown in this figure for the $n = -1$ case over the axial distance from about 3 to 23, the source of the decrease of C_{n_β} at $\alpha = 40°$ for $n = -1.0$ can be identified. This result provides an indication of how to keep C_{n_β} from becoming too positive at high angles-of-attack. Figures 43 to 45 show the ΔC_p vs z plots at a typical cross-section ($x = 18.35$). At $\alpha = 20°$and 30° the effect of the chine angle is predominant on the upper surface. Though the behavior changes on the upper surface, the area under the curves remains nearly the same. At $\alpha = 40°$ the area under the curve suddenly decreases for the $n = -1.0$ case and this leads

to a decrease in side-force at this cross-section. Figure 46 shows the vortex strength and position for the case of $n = -1.0$. This shows that the side-force could arise from the asymmetry in both the relative strengths and relative positions of the windward and leeward vortices.

The vorticity being generated due to separation has been shown to be proportional to the square of the velocity at the separation point in Ref. 14. When $n < -1$ the slope discontinuity is maximum at the chine edge, and results in large velocities approaching the separation point. This results in larger vorticity being generated at the chine edge for these cases. Figure 47 shows the square of velocity at the separation point plotted for different chine angles at $\alpha = 40°$. The $n = -1.0$ case is distinctly different than the other cases. When $n < -1$ the edge angle is zero and hence the strengths of the corresponding leeward and windward vortices are comparable. Also, very close to the nose the leeward vortex is stronger than the windward vortex leading to a negative side-force. As the axial distance increases the vorticity shed on the windward side increases and hence the side-force is positive. Such observations were also made by Kegelman and Roos based on experimental results in Ref. 7. When $n = -1$, as expected, the vorticity shed is much less and of an entirely different character because of reduced slope discontinuity. Moving downstream from the nose, the edge with the largest separation velocity switches sides several times. This is reflected in the side-force plot of fig. 42(c). In this case, very close to the nose the windward vorticity shed is larger than leeward vorticity leading to a positive side-force. As we move aft, the side-force changes sign as the relative shed vorticity strength changes.

Effect of unsymmetrical b/a

Unsymmetrical cross-sections were generated using different values of b/a for the upper and lower surfaces while keeping the same functional form with $m = 0$ and $n = -1.5$. This maintains the zero chine edge angle for all the cases. Two cases were tested. The first one had $b/a = 0.5$ for top and $b/a = 1.5$ for bottom. The second one had $b/a = 1.5$ for top and $b/a = 0.5$ for bottom. Figure 48 shows the cross-sectional shapes together with the computed C_{n_β} for these bodies alongside

the results already presented for symmetrical *b/a*.. The Erickson forebody result is also included, which is geometrically similar with symmetrical *b/a* lying between 0.5 and 1.0. The shallow upper surface is seen to provide higher C_{n_β} than the shallow lower surface geometry. This is because the shallow upper surface results in a stronger vortex and provides a bigger contribution to stability than the use of a shallow lower surface to reduce the negative contribution to stability.

Effect of unsymmetrical cross-sections to vary chine angle

Unsymmetrical cross-sections were generated using different values of shape parameter *n* for the upper and lower surfaces while keeping the same *b/a* = 0.5 which was found to be the best ratio earlier. Such a variation of *n* would vary the chine angle. The effect of varying this parameter on the directional stability is shown in fig. 49. The chine angles were zero for symmetrical cross-sections with *n* < -1 and were finite for all other cases shown in that figure. Only the symmetrical case with n = -1.0 which had the highest chine angle shows a sudden decrease in C_{n_β} at α = 40°. This difference in behavior with the different chine angles suggests the existence of a critical angle which controls the rate of feeding of the vortex as the angle-of-attack changes.

Effect of varying the planform shape

The planform shape for the forebodies studied thus far was same as that of the Erickson forebody. This planform is shown in fig. 50. The parameter XN shown for the tangent ogive forebodies is the distance from the tip of the nose to the station where the planform span becomes a constant. The side-force variation in figs. 35 and 42 showed that most of the positive side-force came from the aft portion of the forebody where the chine line was swept nearly 90°. Hence it was postulated that expanding to a constant cross-section faster would give greater positive side-force.

Because the Erickson planform approximates a tangent ogive with XN = 18, the alternative planform was chosen to expand faster with XN =7, as shown in fig. 50.

The effect of the planform variation on the directional stability is shown in fig. 51. There is a small increase in C_{n_β} for a fixed cross-sectional shape with $b/a = 0.5$, $m = 0$ and $n = -1.0$. One other cross-section, with a flat lower surface, was computed with this planform, and resulted in a C_{n_β} increase. This supported our previous assertion that a smaller $.b/a$ on the lower surface reduces the adverse contribution to C_{n_β} at $\alpha = 20°$ and also at $\alpha = 40°$. Here, note that the chine included angle is much less than the symmetrical case. The directional stability continues to increase at $\alpha = 40°$, rather than remain nearly constant, reinforcing the idea that a critical chine angle might exist which reduces extreme contributions to stability at high angle-of-attack.

Figures 52 and 53 show the effect of planform shape on side-force variation at $\alpha = 20°$ and $\alpha = 40°$ respectively. As expected, after the initial negative side-force, the rate of increase of side-force is greater in the aft portion of the forebody for the blunt nosed planform. Also note that at $\alpha = 40°$, the double hump is eliminated with a blunt-nosed planform and with a flat bottom surface the configuration is even better. However very close to the nose the side-force is more negative. A look at the slopes and curvatures of the different planforms in fig. 54 shows that the tangent ogive planform has a large negative curvature close to the tip of the forebody.

CONCLUSIONS AND DESIGN GUIDELINES

A number of conclusions arise based on the results obtained here. For chined-shaped forebodies, where the separation position is not influenced by viscosity, the Euler solutions were found to be in reasonably good agreement with the results of Navier-Stokes calculations using the Baldwin-Lomax turbulence model as modified by Degani and Schiff. Thus Euler solutions could be used to carry out the parametric study. CFD has been used to explicitly identify the method in

which the pressure distribution on the chine contributes to the directional stability. A novel approach to presentation and evaluation of forebody aerodynamics has been introduced.

For aerodynamic design consideration the following guidelines were obtained:

- The best ratio of maximum half-breadth to the maximum centerline width proves to be $b/a = 0.5$ among the cases analysed for positive directional stability. In general, lower b/a for both the upper and lower surfaces is better from point of view of directional stability. In cases where higher b/a is a requirement, it is better to increase the lower surface b/a which results in a smaller penalty than if we were to increase upper surface b/a.

- The effect of chine angle on the directional stability characteristics was found to be insignificant except when the chine angle was large. There could be a critical chine angle beyond which it becomes an important factor (we did not attempt to find one in this study). If such a critical angle exists, it provides an indication of how to keep C_{n_β} from becoming too positive at high angles of attack.

- The positive contribution to the stability is seen to come from the aft portion of the forebody where the chine line is swept nearly 90°. Changing the planform shape by allowing it to expand faster to a constant value increases the C_{n_β} only by a small amount. However, the behavior of the side-force plots vary significantly for different planform shapes.

ACKNOWLEDGEMENTS

Virginia Polytechnic Institute and State University

    Blacksburg, Virginia 24061

        October 22, 1991

        (rev., February 2, 1992)

The following is the list of directories under which the solutions are saved on Voyager. These are stored on the Mass Storage under the userids (1) RAVI or (2) WHMAS.

GEN1 $m = 0$, $n = -1.5$, $b/a = 1.0$ (top and bottom), Erickson planform

GEN2 $m = 0$, $n = -1.5$, $b/a = 0.5$ (top and bottom), Erickson planform

GEN3 $m = 0$, $n = -1.5$, $b/a = 1.5$ (top and bottom), Erickson planform

GEN4 $m = 0$, $n = -1.25$, $b/a = 0.5$ (top and bottom), Erickson planform

GEN5 $m = 0$, $n = -1.0$, $b/a = 0.5$ (top and bottom), Erickson planform

GEN6 $m = 0$, $n = -1.5$ (top and bottom), $b/a = 1.5$ (top) and 0.5 (bottom), Erickson planform

GEN7 $m = 0$, $n = -1.5$ (top and bottom), $b/a = 0.5$ (top) and 1.5 (bottom), Erickson planform

GEN8 $m = 0$, $n = -1.5$ (top) and -1.0 (bottom), $b/a = 0.5$ (top and bottom),

Erickson planform

GEN9 $m = 0$, $n = -1.0$ (top) and -1.5 (bottom), $b/a = 0.5$ (top and bottom),

Erickson planform

GEN11 $m = 0$, $n = -1.0$ (top and bottom), $b/a = 0.5$ (top) and 0 (bottom),

Tangent ogive planform

GEN12 $m = 0$, $n = -1.0$, $b/a = 0.5$ (top and bottom), Tangent ogive planform

Files have been stored for $\alpha = 20°$, $30°$, $40°$ and $\beta = 5°$ for each of the above cases with the following nomenclature :

Grid files   suffixed with " **.grd** "

Restart files   suffixed with " **.rest** "

Output files   suffixed with " **.out** " and " **.prout** "

PLOT3D files   suffixed with " **.plg** " and " **.plq** "

e.g., **GEN2** contains

mrw-r--r--	1 ravi	372052	Apr 8 1991	a20b5.out	(output file)
mrw-r--r--	1 ravi	1158084	Apr 8 1991	a20b5.plg	(PLOT3D grid)
mrw-r--r--	1 ravi	1930449	Apr 8 1991	a20b5.plq	(PLOT3D solution)
mrw-r--r--	1 ravi	62631	Apr 8 1991	a20b5.prout	(output file)
mrw-r--r--	1 ravi	4273400	Apr 8 1991	a20b5.rest1	(restart file)
mrw-r--r--	1 ravi	372052	Apr 9 1991	a30b5.out	(output file)
mrw-r--r--	1 ravi	1158084	Apr 9 1991	a30b5.plg	(PLOT3D grid)
mrw-r--r--	1 ravi	1930449	Apr 9 1991	a30b5.plq	(PLOT3D solution)
mrw-r--r--	1 ravi	62631	Apr 9 1991	a30b5.prout	(output file)
mrw-r--r--	1 ravi	4273400	Apr 9 1991	a30b5.rest1	(restart file)
mrw-r--r--	1 ravi	35485	Apr 19 1991	a35b5.out	(output file)
mrw-r--r--	1 ravi	4275800	Apr 19 1991	a35b5.rest1	(restart file)
mrw-r--r--	1 ravi	372052	Apr 9 1991	a40b5.out	(output file)
mrw-r--r--	1 ravi	35434	Apr 15 1991	a40b5.out1	(output file)
mrw-r--r--	1 ravi	1158084	Apr 9 1991	a40b5.plg	(PLOT3D grid)
mrw-r--r--	1 ravi	464202	Apr 15 1991	a40b5.plg1	(PLOT3D grid latest)
mrw-r--r--	1 ravi	1930449	Apr 9 1991	a40b5.plq	(PLOT3D solution)
mrw-r--r--	1 ravi	773773	Apr 15 1991	a40b5.plq1	(PLOT3D soln latest)
mrw-r--r--	1 ravi	62631	Apr 9 1991	a40b5.prout	(output file)
mrw-r--r--	1 ravi	34209	Apr 15 1991	a40b5.prout1	(output file latest)
mrw-r--r--	1 ravi	4273400	Apr 9 1991	a40b5.rest1	(restart file)
mrw-r--r--	1 ravi	4274920	Apr 15 1991	a40b5.rest2	(restart file latest)
-rw-r--r--	1 ravi	2494	Apr 9 1991	case.mult	(input file)
mrw-r--r--	1 ravi	5464728	Apr 8 1991	job2.grd	(input grid file)

REFERENCES

1. Chambers, J.R., "High-Angle-of-Attack Aerodynamics: Lessons Learned," AIAA Paper 86-1774, June 1986.

2. Chambers, J.R. and Grafton, S.B., "Aerodynamic Characteristics of Airplanes at High Angle of Attack," NASA TM 74097, Dec. 1977.

3. Grafton, S.B., Chambers, J.R., and Coe, P.L., Jr., "Wind-Tunnel Free-Flight Investigation of a Model of a Spin Resistant Fighter Configuration," NASA TN D-7716, June 1974.

4. Mason, W.H., and Ravi, R., "A Computational Study of the F-5A Forebody Emphasizing Directional Stability," AIAA-91-3289, September 1991.

5. Mason, W.H., and Ravi, R.,"Hi-Alpha Forebody Design : Part I - Methodology Base and Initial Parametrics," VPI- Aero-176, October 1990.

6. Erickson, G.E., and Brandon, J.M., "Low-Speed Experimental Study of the Vortex Flow Effects of a Fighter Forebody Having Unconventional Cross-Section," AIAA Paper No. 85-1798.

7. Kegelman, J.T., and Roos, F.W.,"Influence of Forebody Cross-Section Shape on Vortex Flowfield Structure at High Alpha," AIAA Paper 91-3250, September 1991.

8. Roos, F.W., and Kegelman, J.T.,"Aerodynamics Characteristics of Three Generic Forebodies at High Angles of Attack," AIAA Paper 91-0275, Jan 1991.

9. Hall, R.M., "Influence of Forebody Cross-Sectional Shape on Wing Vortex-Burst Location," *Journal of Aircraft*, Vol. 24, No. 9, September 1987.

10. Thomas, J.L., van Leer, B., and Walters, R.W., "Implicit Flux-Split Schemes for the Euler Equations," AIAA Paper 85-1680, July 1985.

11. Ghaffari, F., personal communication, 1990.

12. Mason, W.H., and Miller, D.S., "Controlled Supercritical Crossflow on Supersonic Wings - An Experimental Verification," AIAA Paper 80-1421, July 1980.

13. Mendenhall, M.R., and Lesieutre, D.J., "Prediction of Subsonic Vortex Shedding From Forebodies With Chines," NASA Contractor Report 4323, September 1990.

14. Mendenhall, M.R., Spangler, S.B., and Perkins, S.C.,"Vortex Shedding from Circular and Noncircular Bodies at High Angles of Attack," AIAA Paper 79-0026, Jan 1979.

Reference Parameters	F-5A	Erickson	Generic
Mean Aerodynamic Chord c	16.08 in	32.04 in	32.04 in
Wing Span b'	52.68 in	46.80 in	46.80 in
Model Length l	31.025 in	30.00 in	30.00 in
Reynolds Number Re_l	1.25 x 10^6	1.02 x 10^6	1.02 x 10^6
Reference Area S_{ref}	754.56 in^2	1264.32 in^2	1264.32 in^2
Moment Reference Center from Nose	57.72 in	12.816 in	12.816 in

Table 1. Reference Data Used in Computing Forces and Moments

Matrix of Cases for "Symmetric" Chine Forebody Directional Stability

		$\beta = 0°$			$\beta = 5°$		
		$\alpha = 20°$	$\alpha = 30°$	$\alpha = 40°$	$\alpha = 20°$	$\alpha = 30°$	$\alpha = 40°$
$b/a = 0.5$	$n = -1.50$	✗	✗	✗	✓	✓	✓
	$n = -1.25$	✗	✗	✗	✓	✓	✓
	$n = -1.00$	✗	✗	✗	✓	✓	✓
$b/a = 1.0$	$n = -1.50$	✗	✗	✗	✓	✓	✓
	$n = -1.25$	✗	✗	✗	✗	✗	✗
	$n = -1.00$	✗	✗	✗	✗	✗	✗
$b/a = 1.5$	$n = -1.50$	✗	✗	✗	✓	✓	✓
	$n = -1.25$	✗	✗	✗	✗	✗	✗
	$n = -1.00$	✗	✗	✗	✗	✗	✗

Table 2. Total Cases for Parametric Study

Each inviscid "crude grid" run ≈ 3400 CPU seconds + 200 sec ≈ 3600 sec

effect	planforms	b/a's	α's	β's	n's	total
b/a	1	3	3	1	1	9
sideslip ($\beta = 10°$)	1	1	3	1	1	3
chine angle (extra)	1	1	3	1	2	6
split b/a	1	2	3	1	1	6
split chine angles	1	1	3	1	2	6
planform	2	1	2	1	1	4
flat bottom	1	1	2	1	1	2
						36

Total CPU time for Euler design: 36 hours

Table 3. CPU Time for Parametric Study
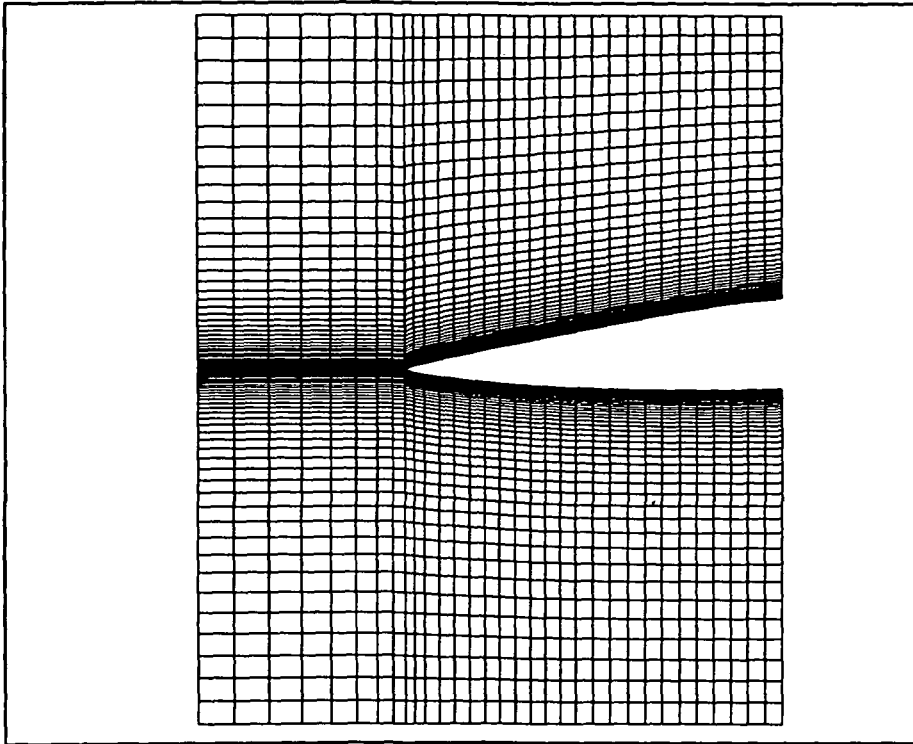
Figure 1. F-5A grid with H-O grid topology used in earlier computations
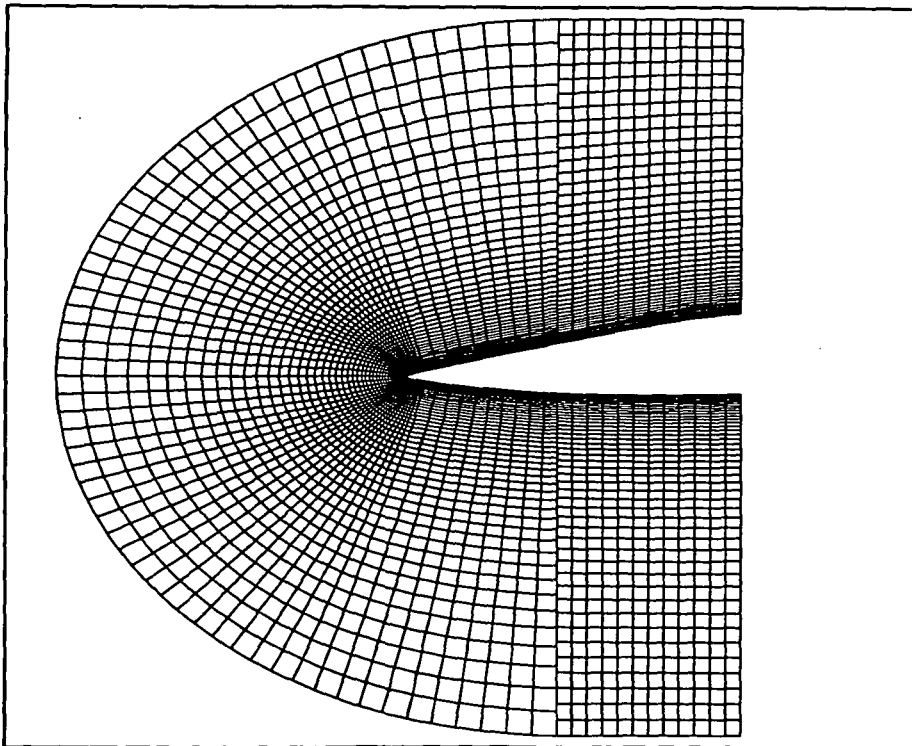
Figure 2. F-5A grid with C-O grid topology for front block and H-O grid for rear block
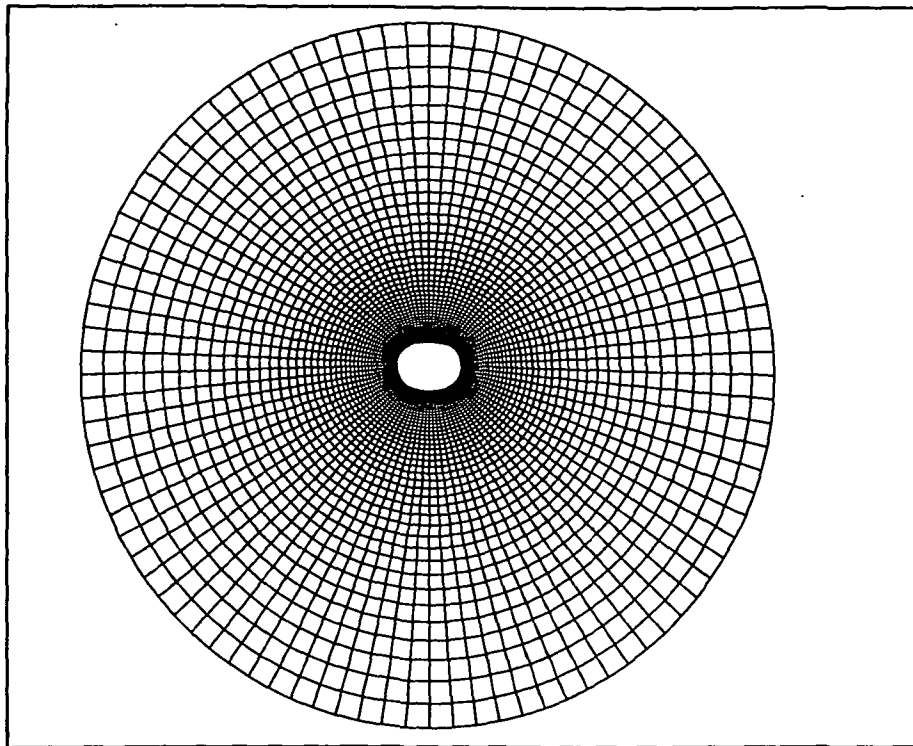
a) entire crossplane grid at FS 14.02
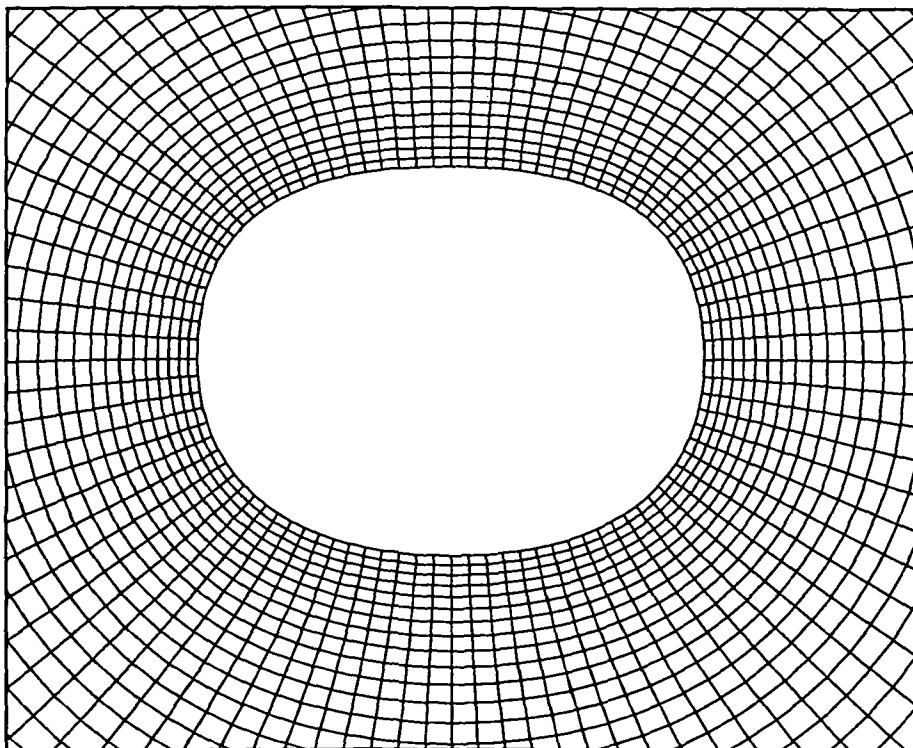
b) near body details at FS 14.02

Figure 3. F-5A forebody grid details in crossflow plane
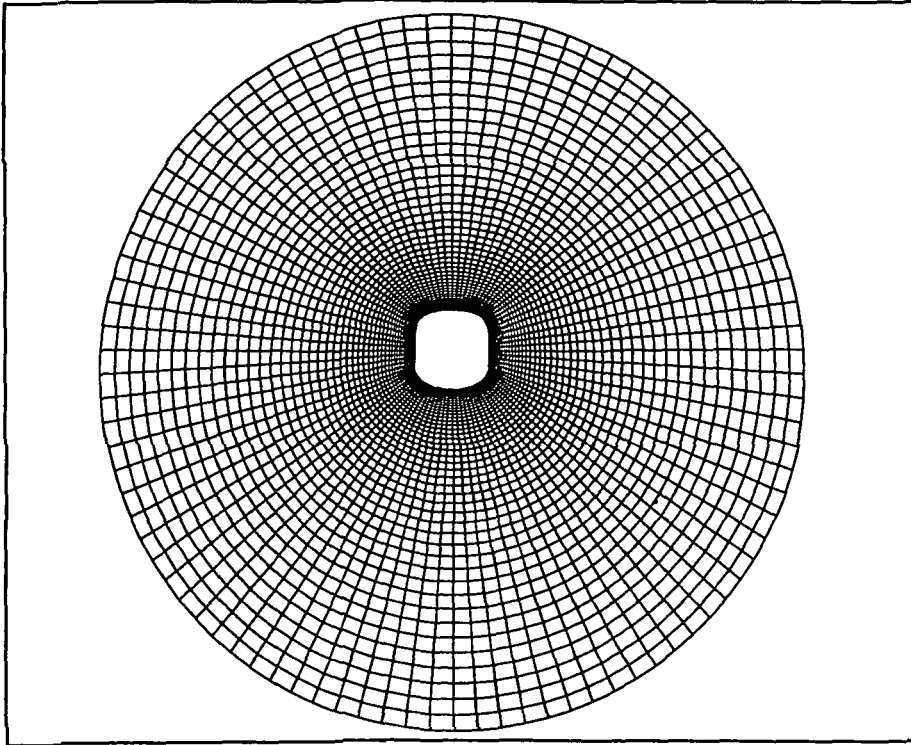
a) entire crossplane grid at FS 29.61
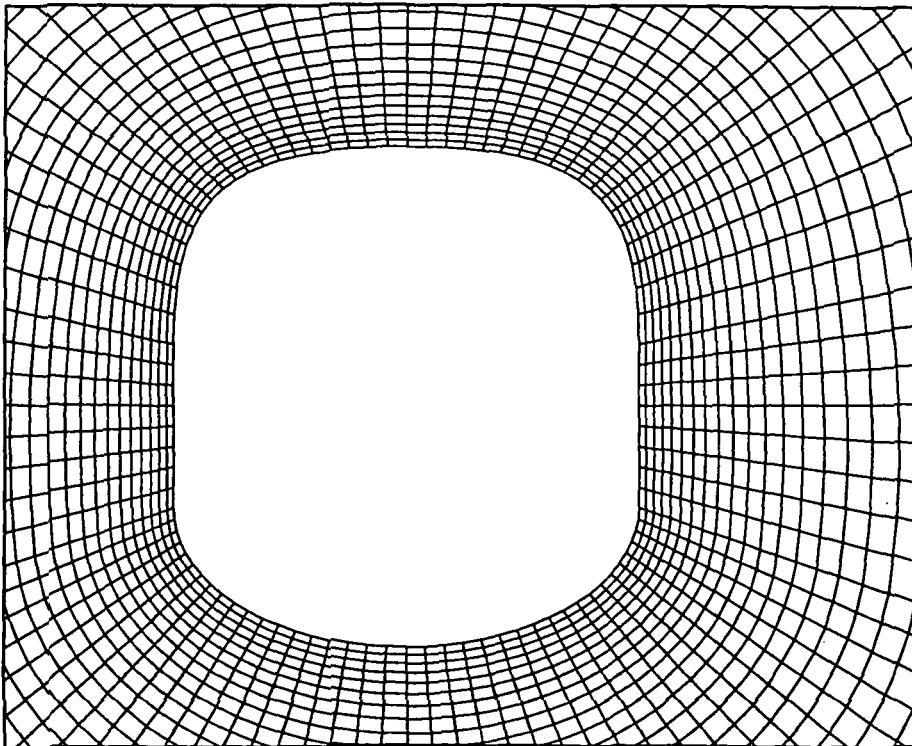
b) near body details at FS 29.61

Figure 4. F-5A forebody grid details in crossflow plane
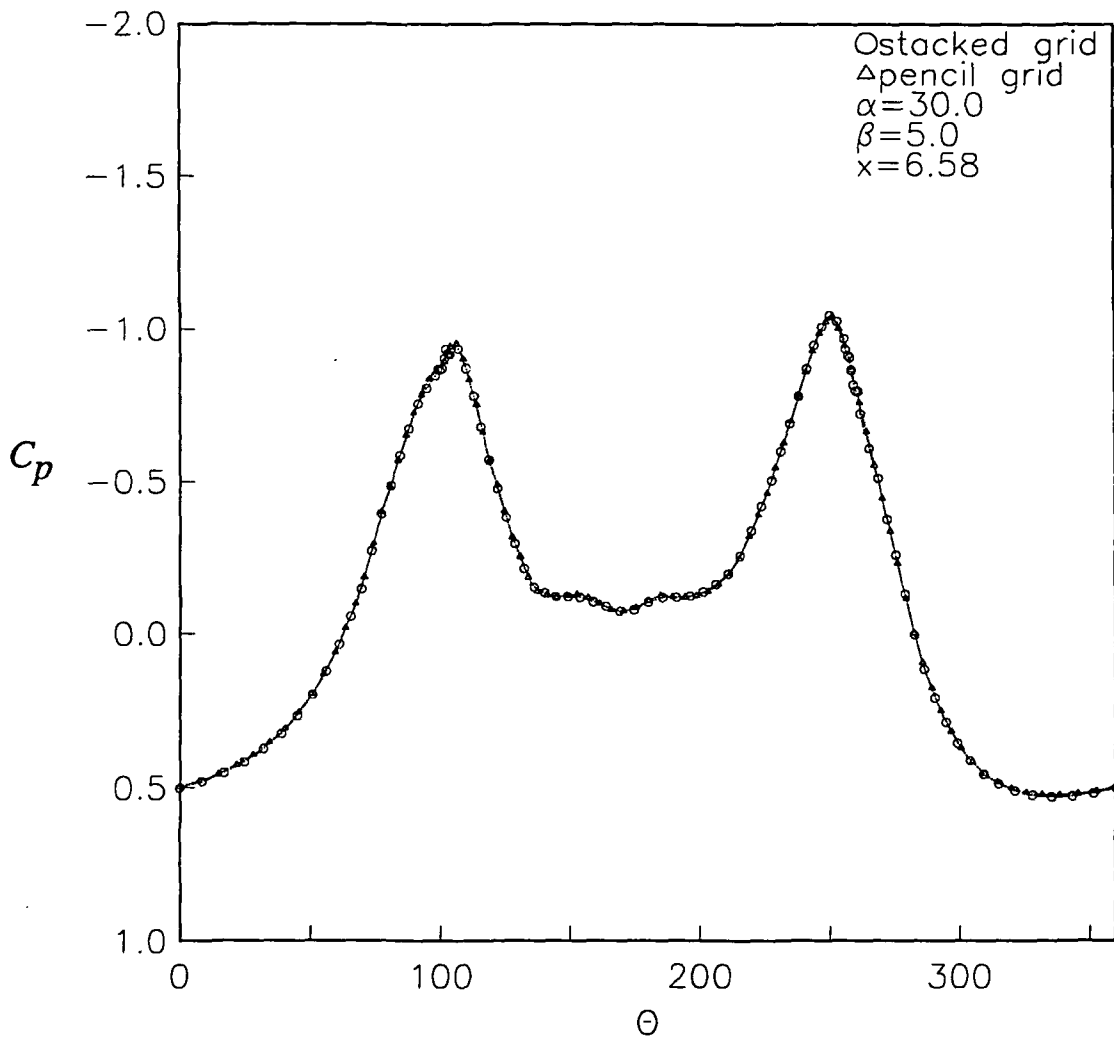
Figure 5.   Comparison of inviscid surface pressures between the two grid systems
    at FS 6.58

32
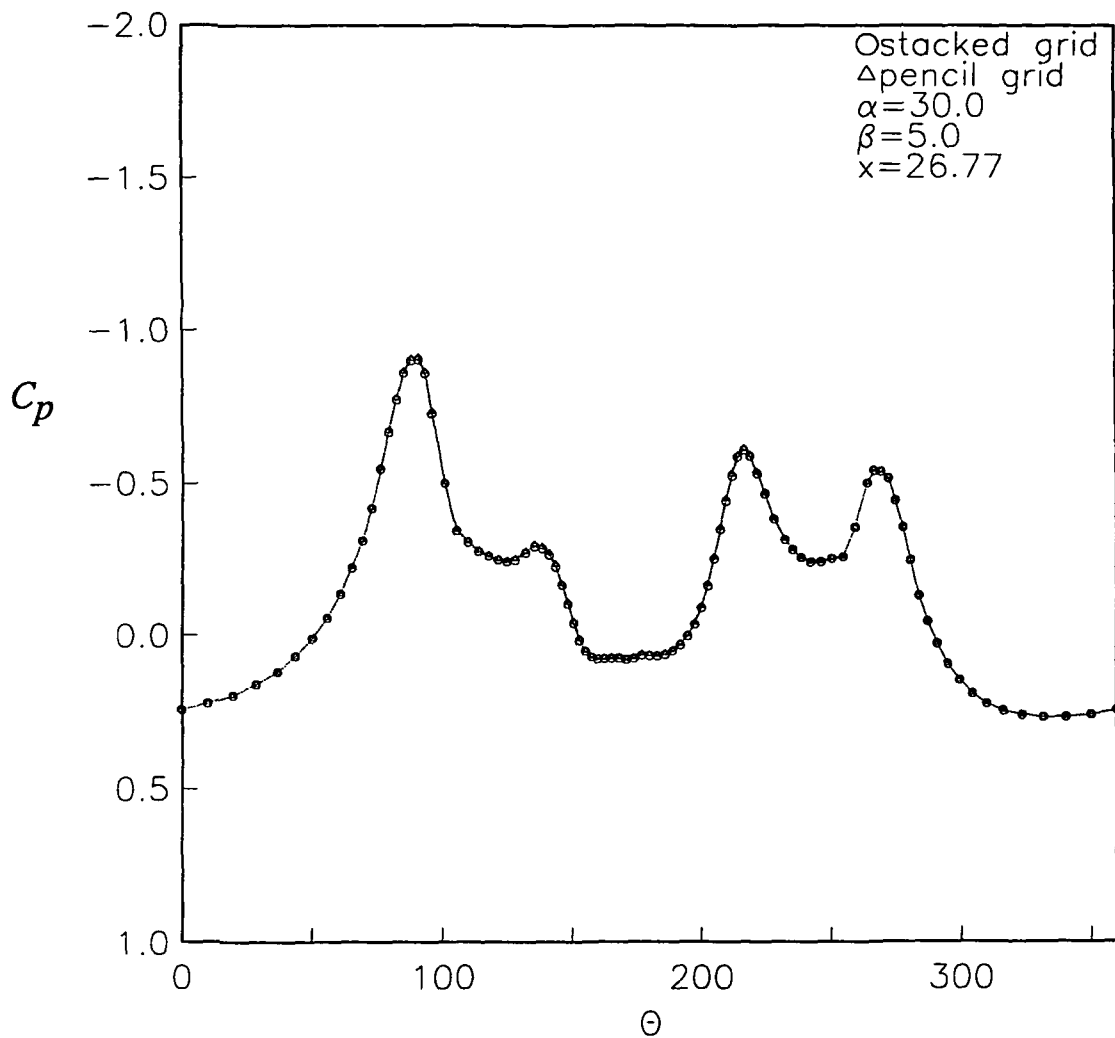
Figure 6. Comparison of inviscid surface pressures between the two grid systems at FS 26.77
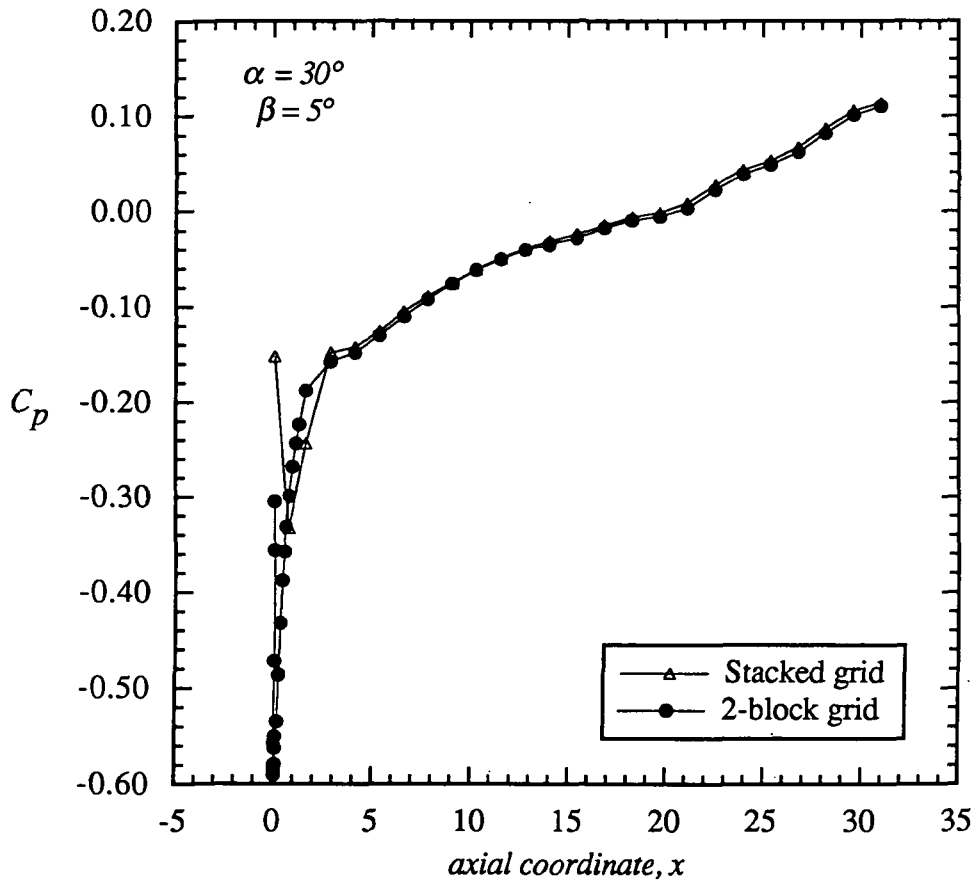
Figure 7. Comparison of F-5A inviscid surface pressures on the leeward plane

$$\Delta C_p = (C_p)_{leeward} - (C_p)_{windward}$$

$$C_y = \int \Delta C_p dz$$

$$C_n = \int_{X_{le}}^{X_{base}} (x - x_{ref}) C_y dx$$
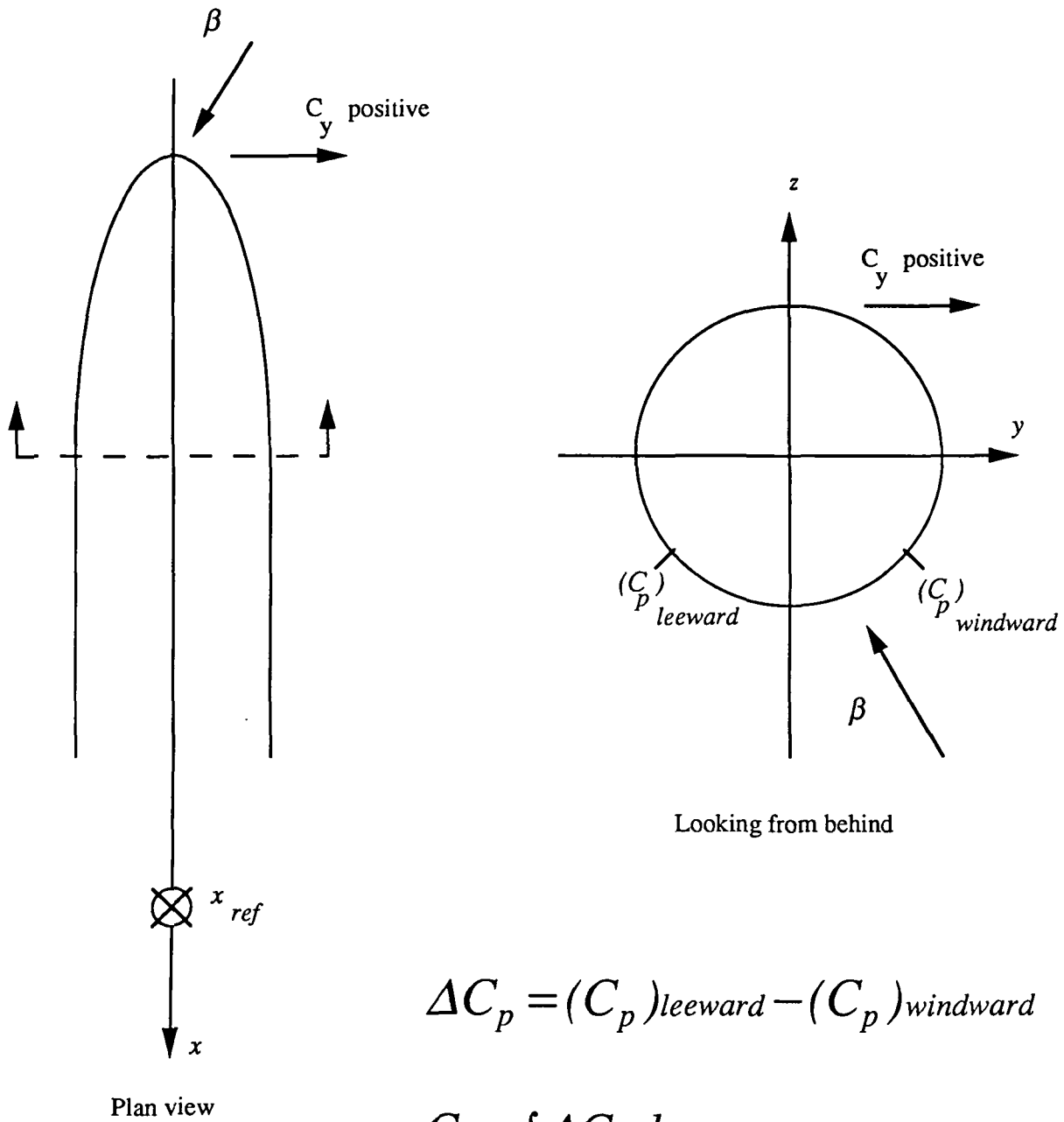
Figure 8. Sign convention for forces and moments used in the present study
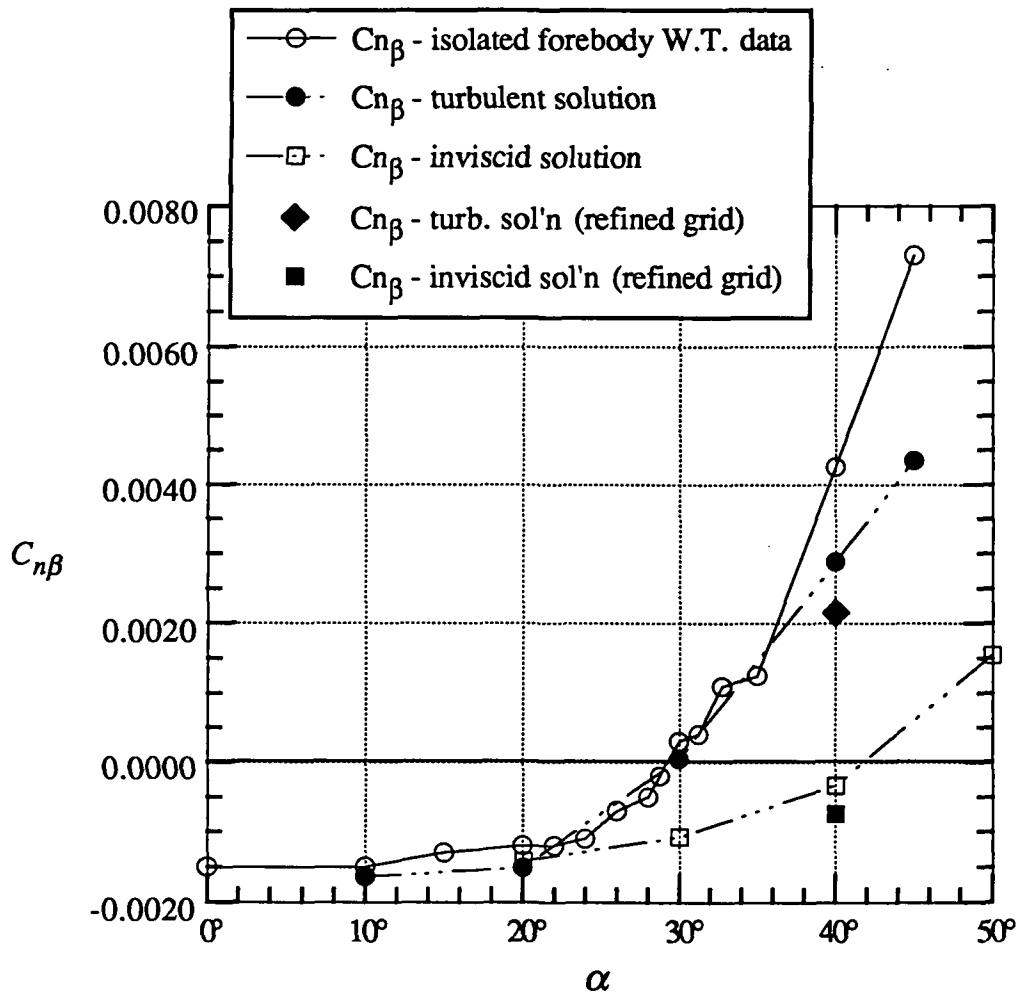
Fig. 9   F-5A directional stability: Comparison of calculation with experiment.
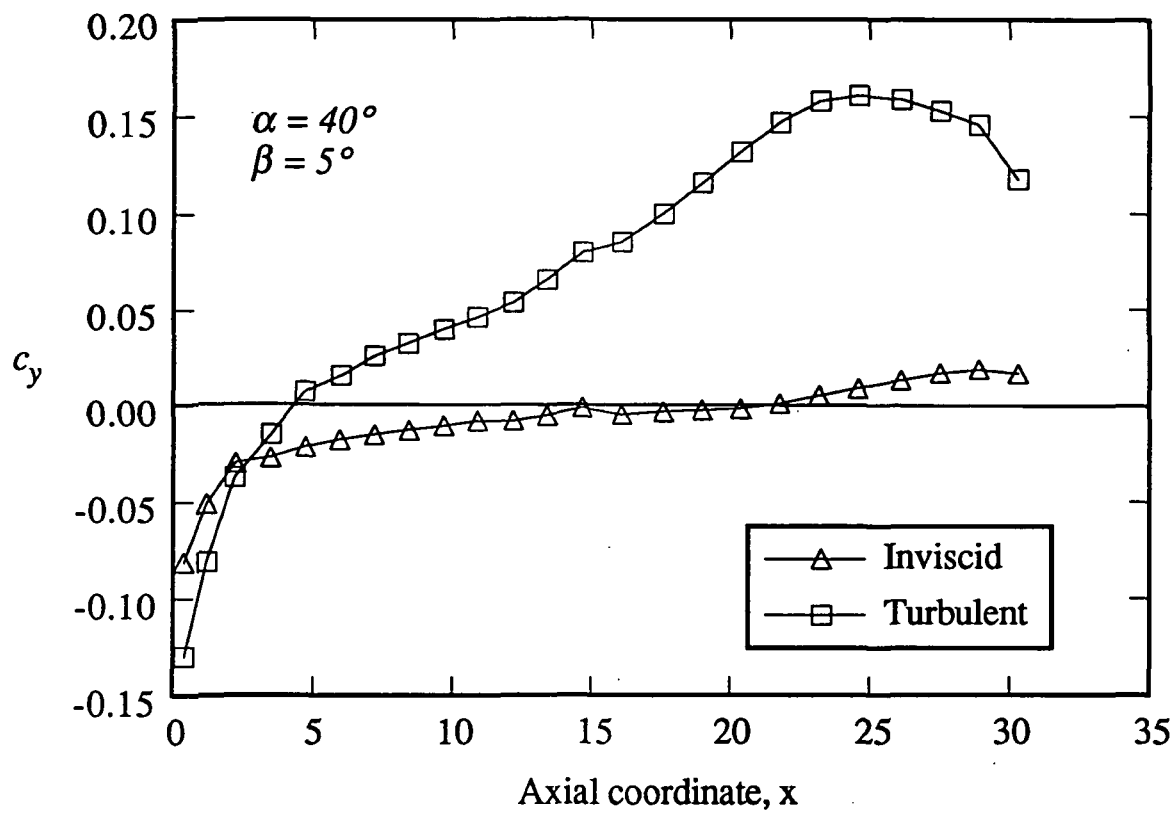
Figure 10. Computed distribution of side force along the F-5A forebody.
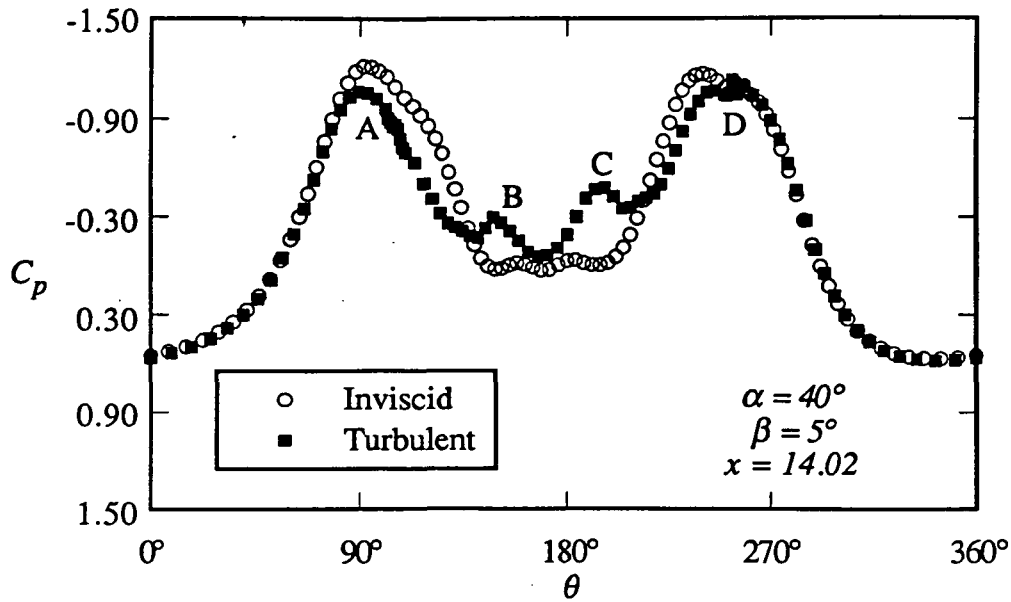
a) inviscid and turbulent surface pressure distribution
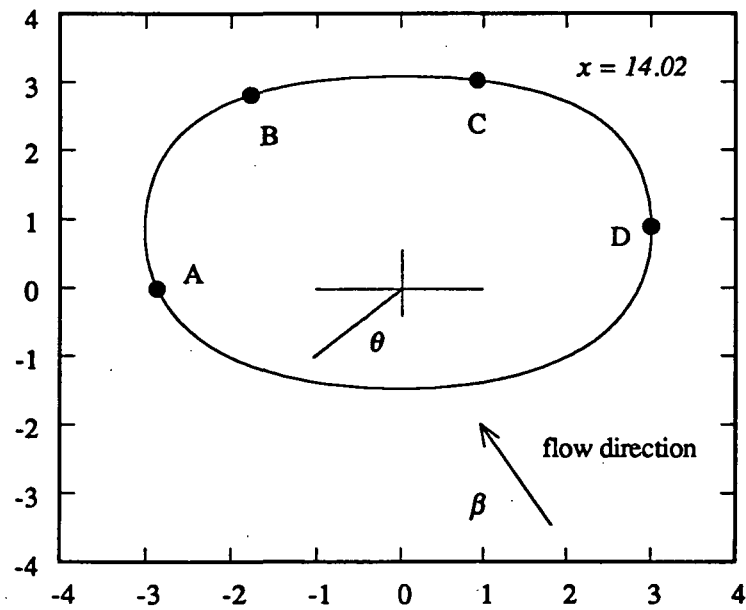
b) cross-section at FS 14.02

Figure 11. Comparison of F-5A inviscid and turbulent surface pressures at FS 14.02

38
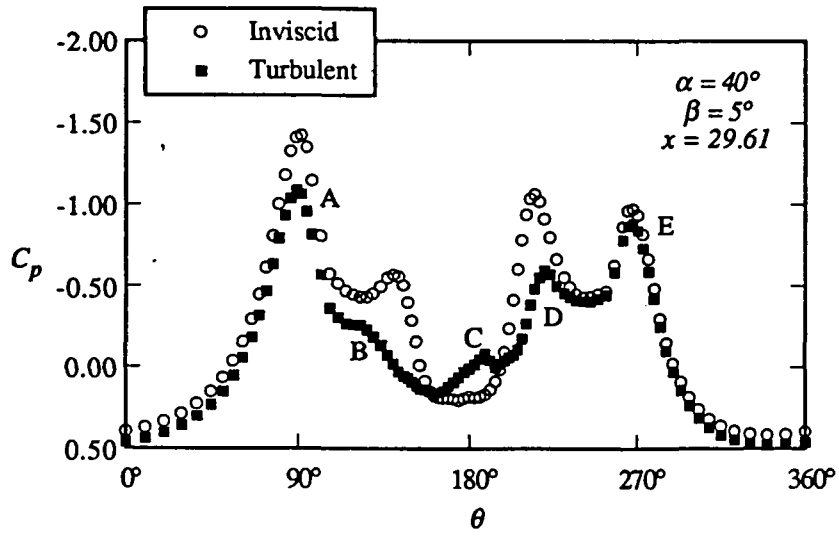
a) inviscid and turbulent surface pressure distribution
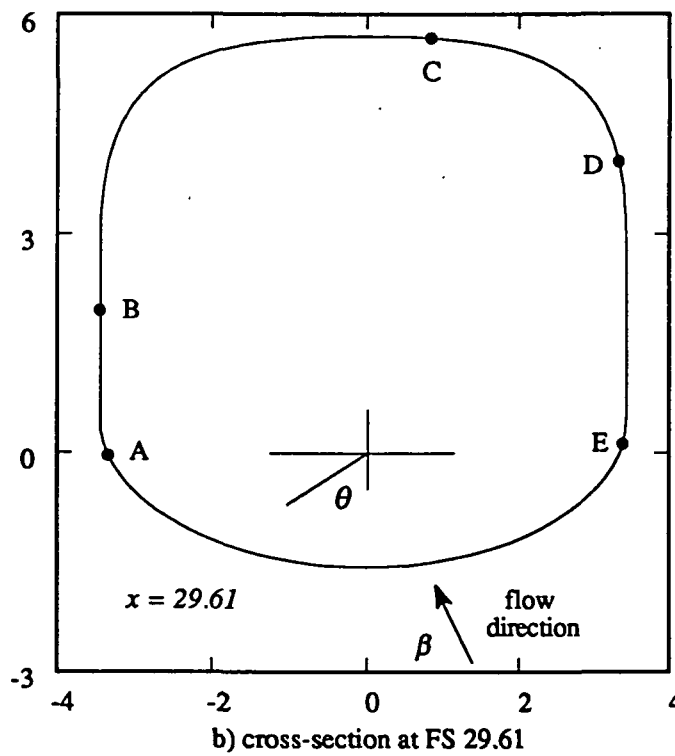
b) cross-section at FS 29.61

Figure 12. Comparison of F-5A inviscid and turbulent surface pressures at FS 29.61
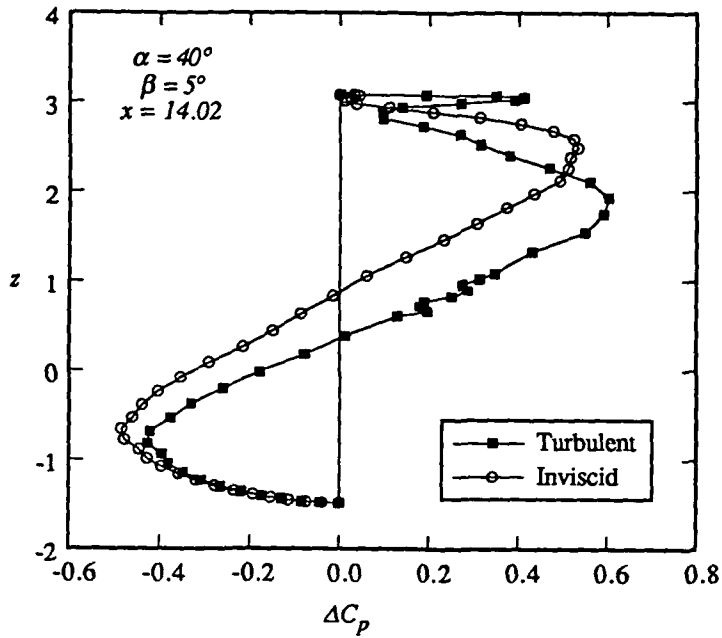
(a) FS = 14.02
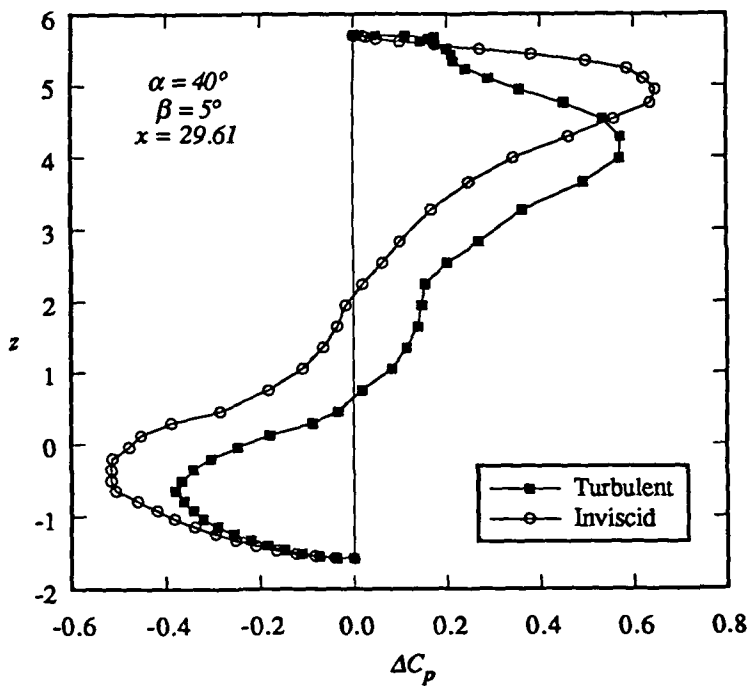
(b) FS 29.61

Figure 13. Variation of ΔC_p vertically along the cross section at FS 14.02 and FS 29.61
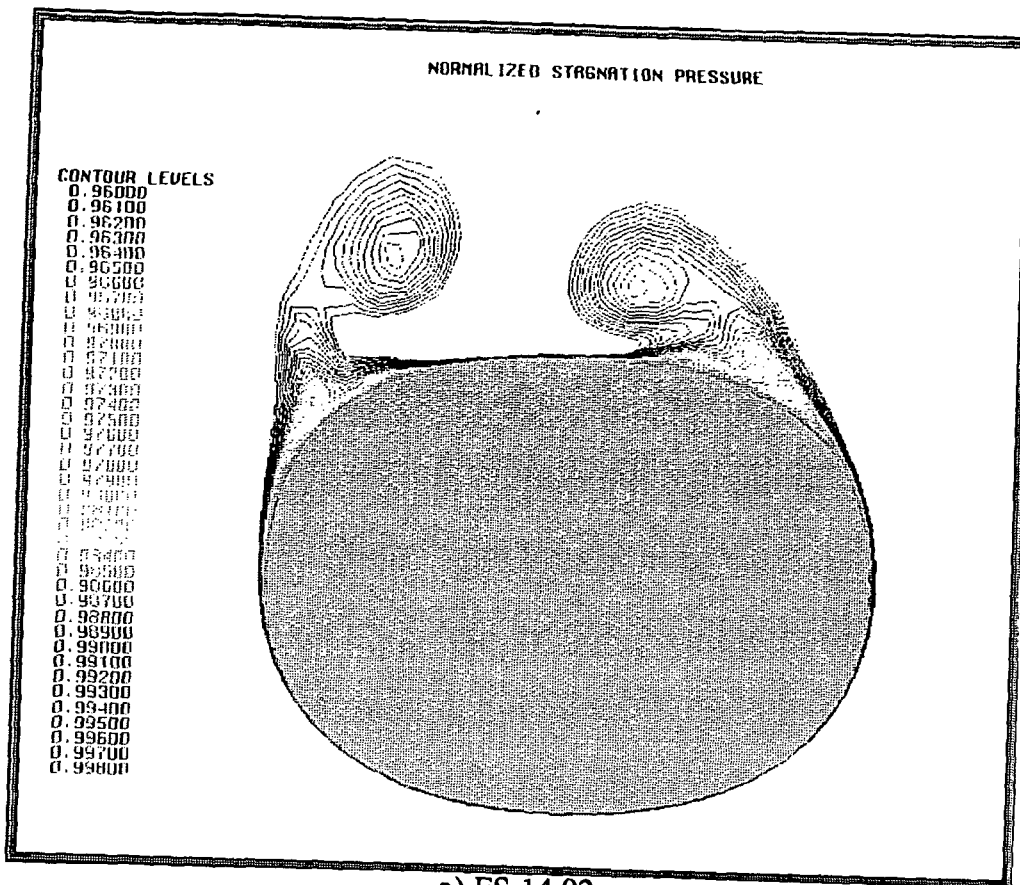
a) FS 14.02
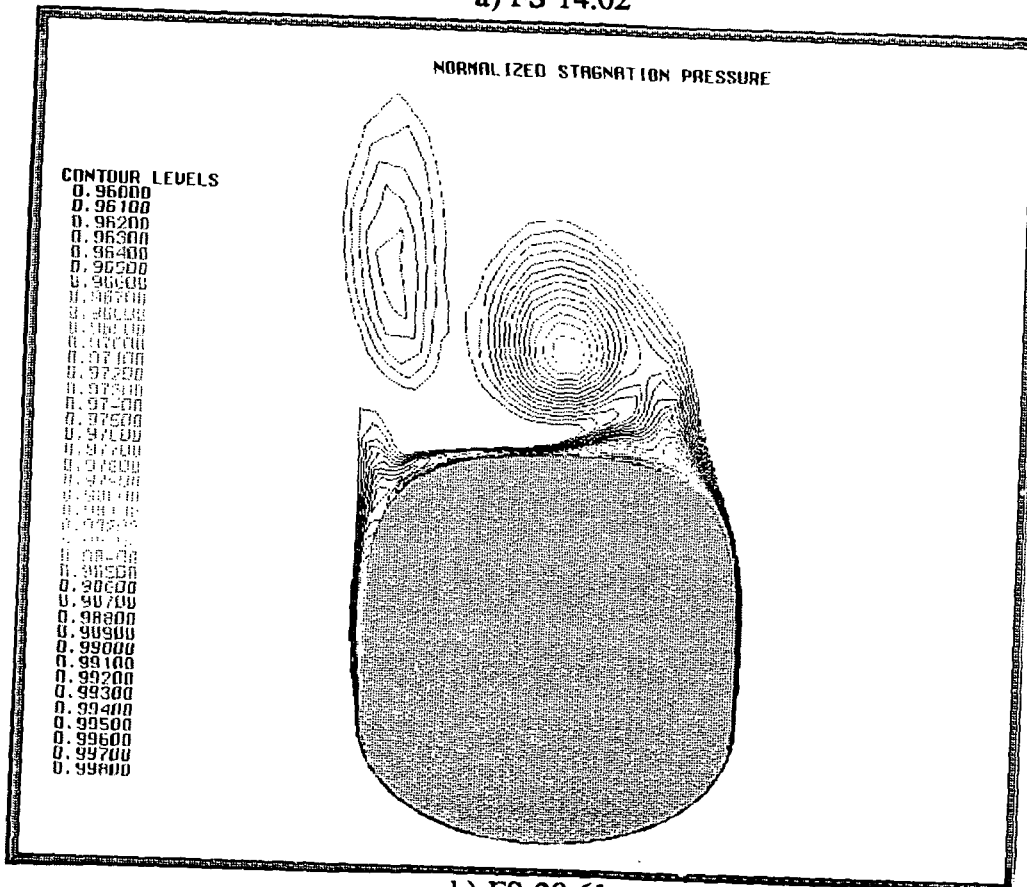
b) FS 29.61

Figure 14. F-5A forebody turbulent stagnation pressure contours for $\alpha = 40°$ and $\beta = 5°$

41
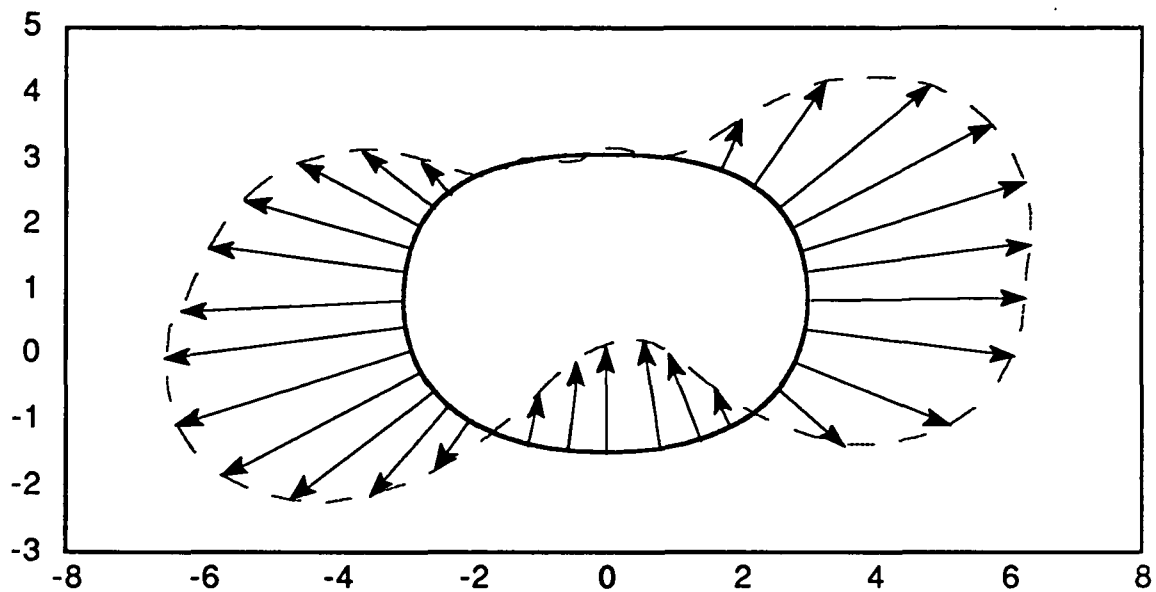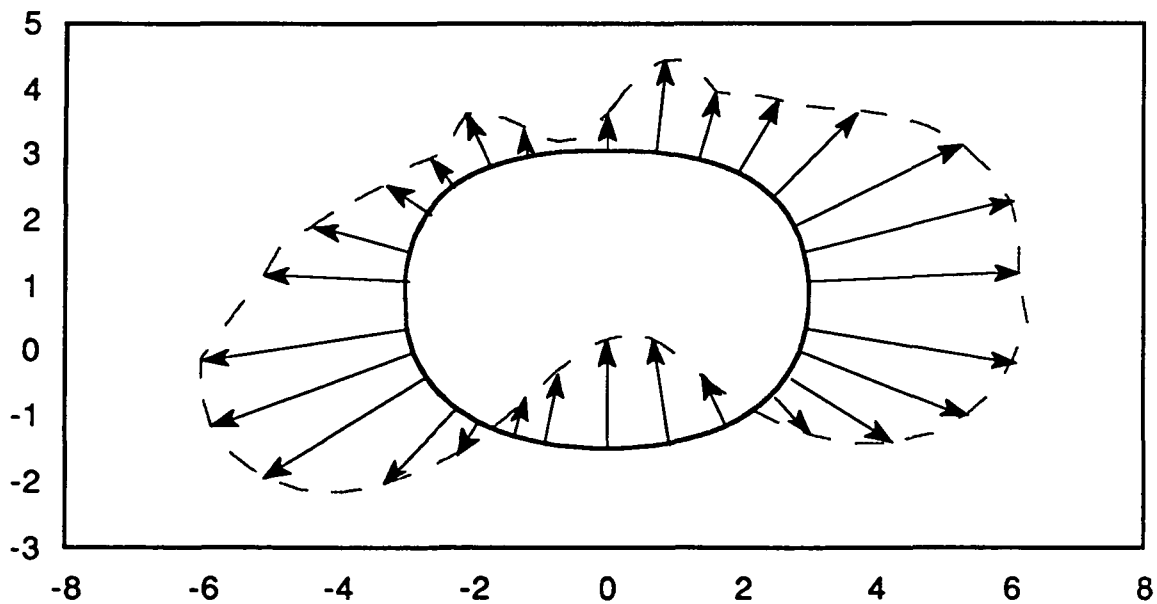
a) Inviscid

b) Turbulent

Figure 15. F-5A forebody pressure vectors at FS 14.02 for $\alpha = 40°$ and $\beta = 5°$
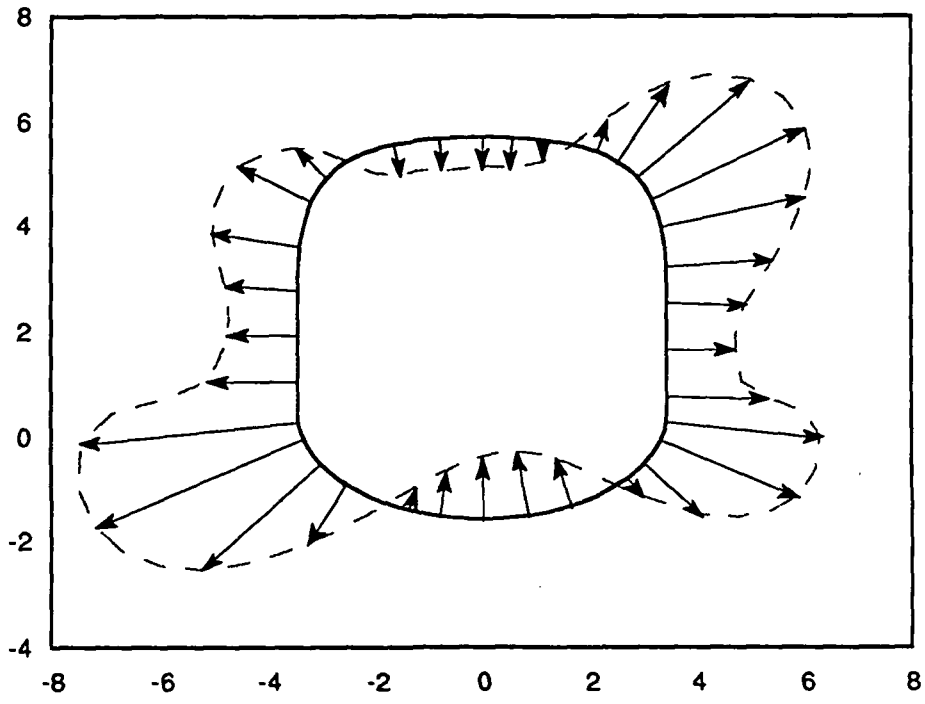
a) Inviscid
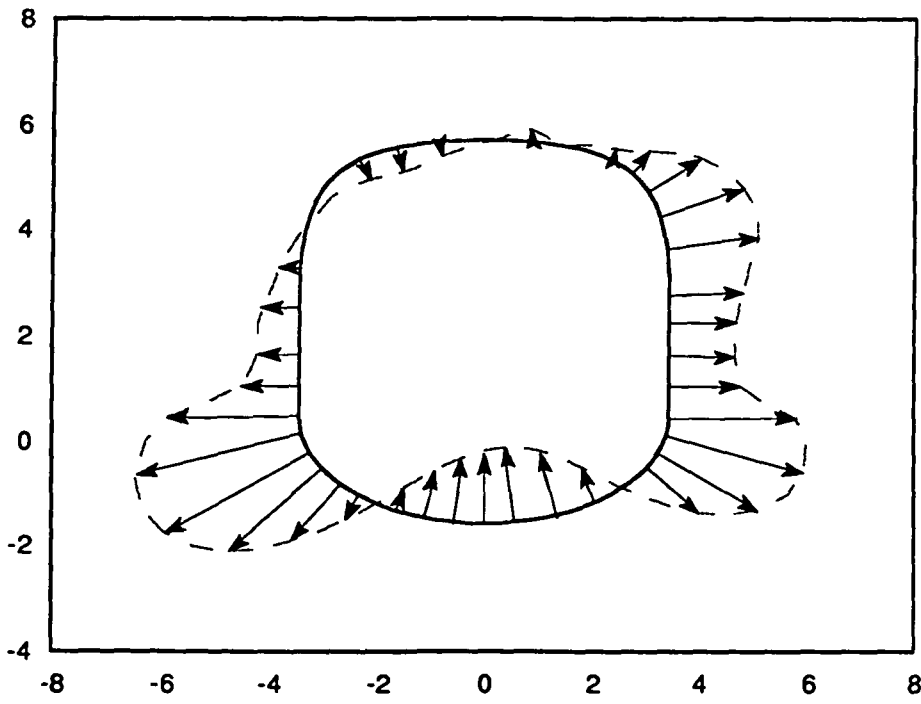
b) Turbulent

Figure 16. F-5A forebody pressure vectors at FS 29.61 for $\alpha = 40°$ and $\beta = 5°$

43
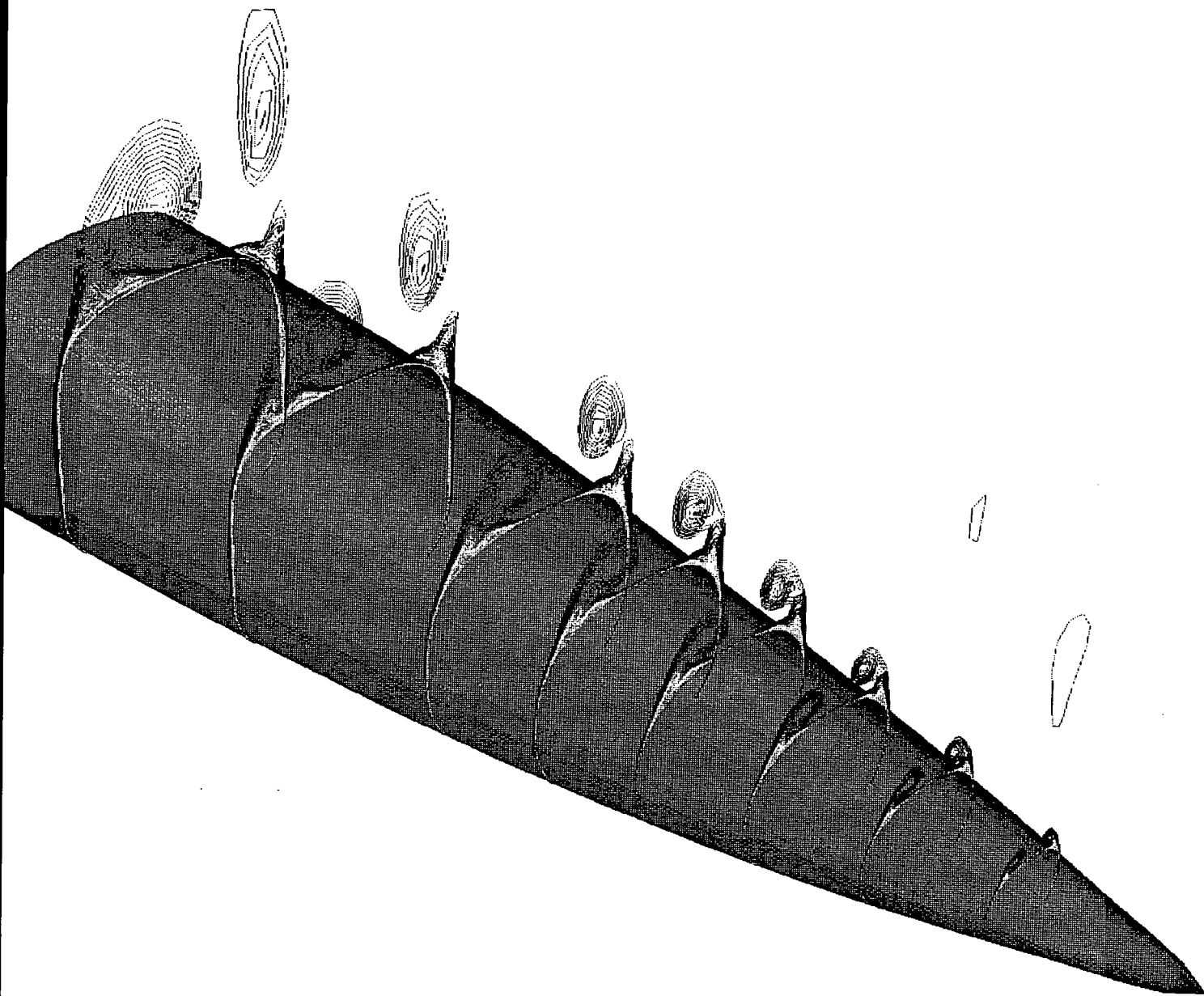
Figure 17. F-5A vortex path along forebody for $\alpha = 40°$ and $\beta = 5°$ ·
(turbulent stagnation pressure contours)
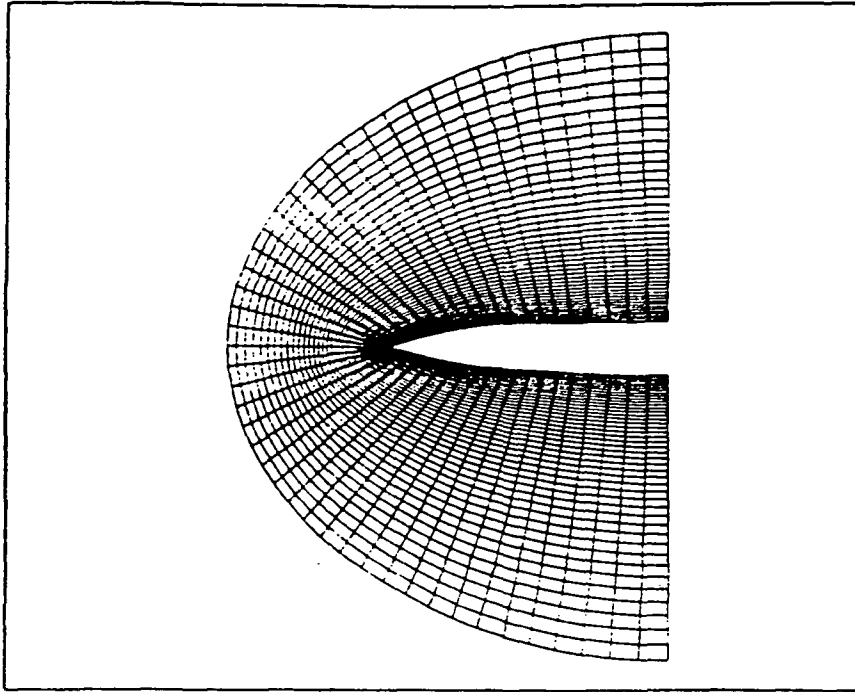
(a) Full plane
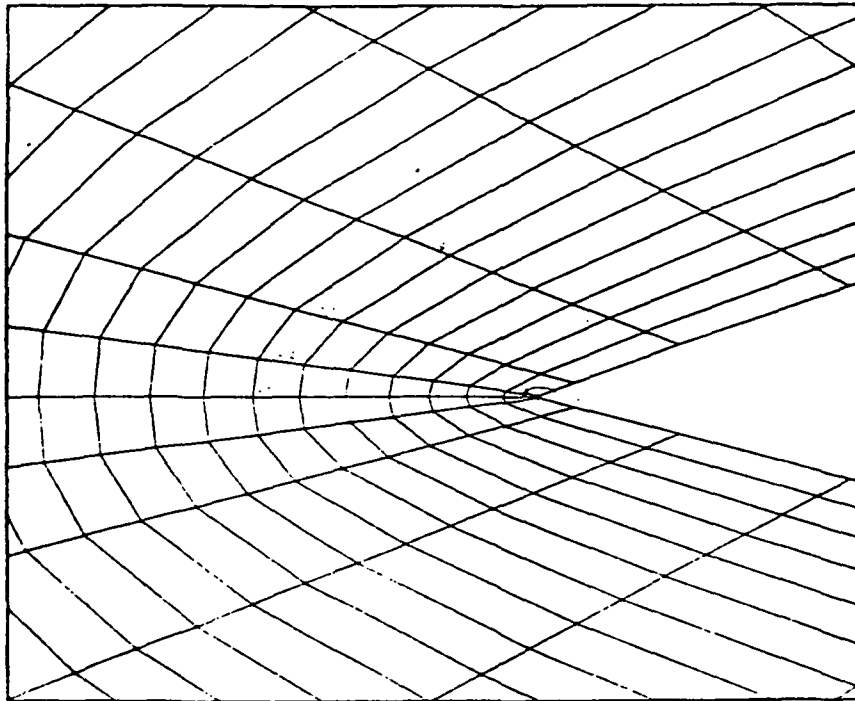
(b) closeup at the nose

Figure 18. Erickson chine forebody longitudinal baseline grid details

45
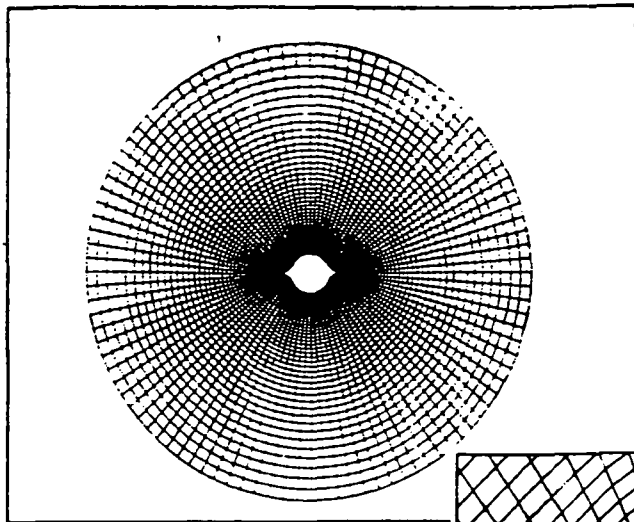
(a) Cross sectional grid

(b) Closeup at the surface
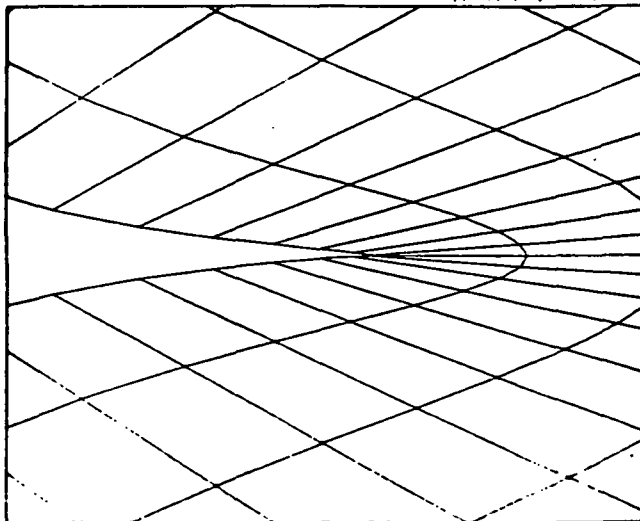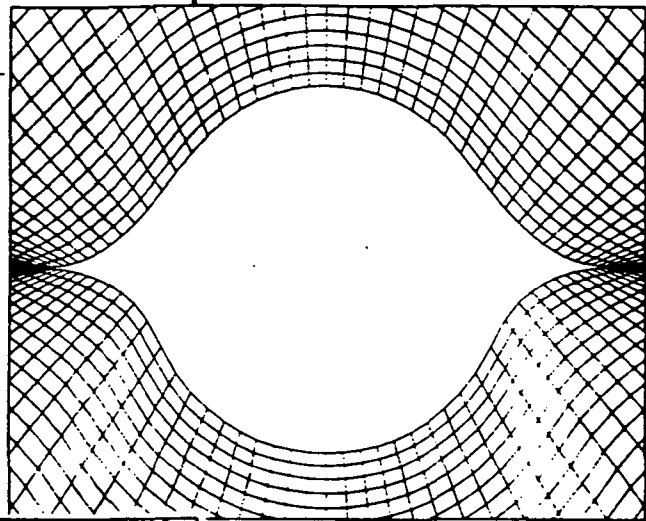
(c) Closeup at the chine edge

Figure 19. Erickson chine forebody cross sectional baseline grid details
$x = 30$ *in.* ($i = 25$)
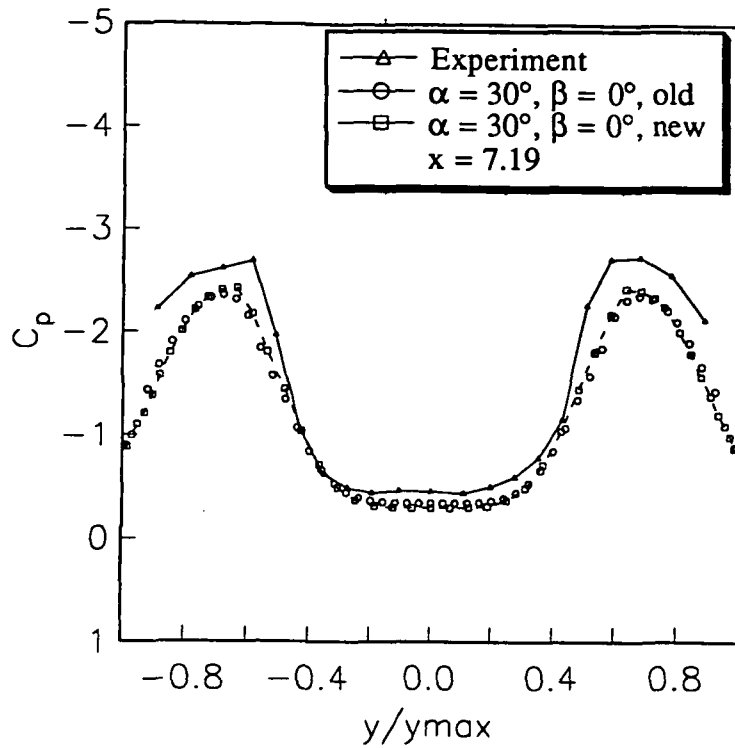
Figure 20. Comparison of Erickson forebody surface pressures between stacked and pencil grids at FS 7.19
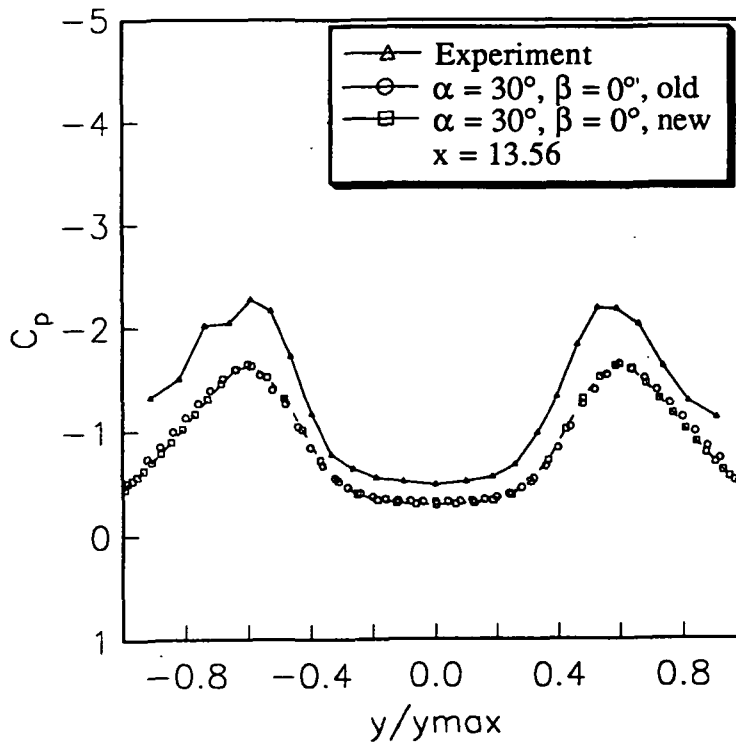
Figure 21. Comparison of Erickson forebody surface pressures between stacked and pencil grids at FS 13.56
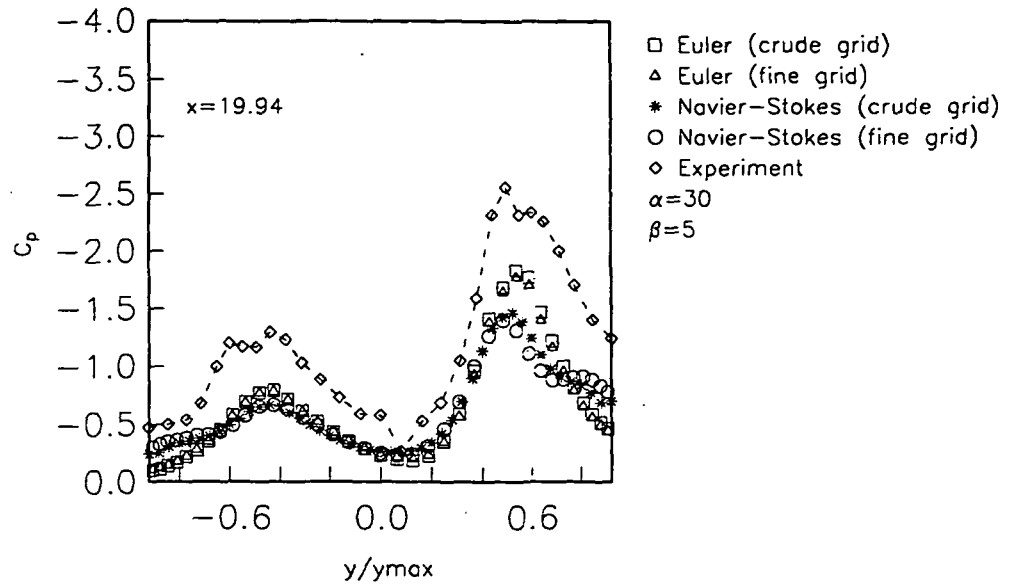
c) FS 19.94
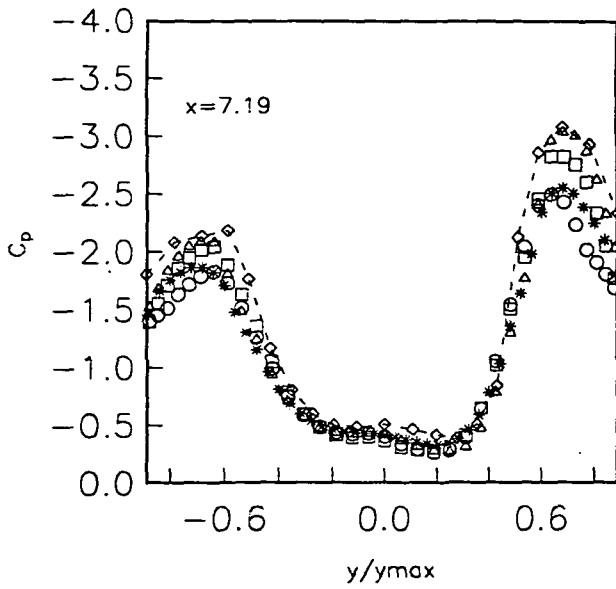
a) FS 7.19
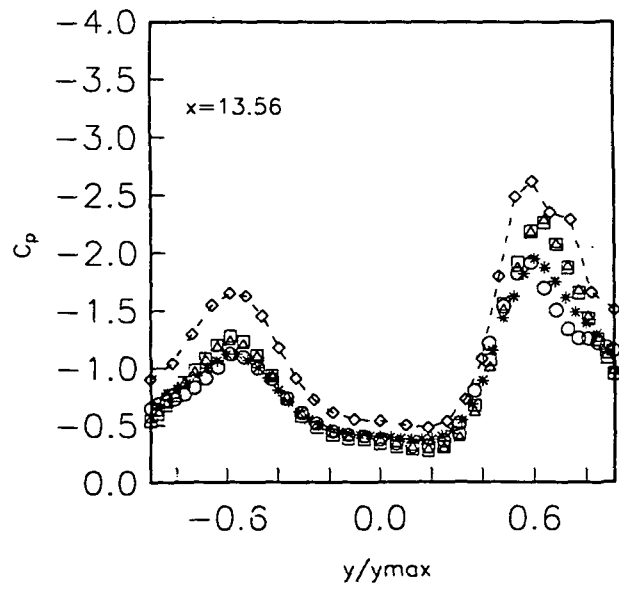
b) FS 13.56

Figure 22. Erickson chine forebody surface pressures at $\alpha = 30°$ and $\beta = 5°$

48
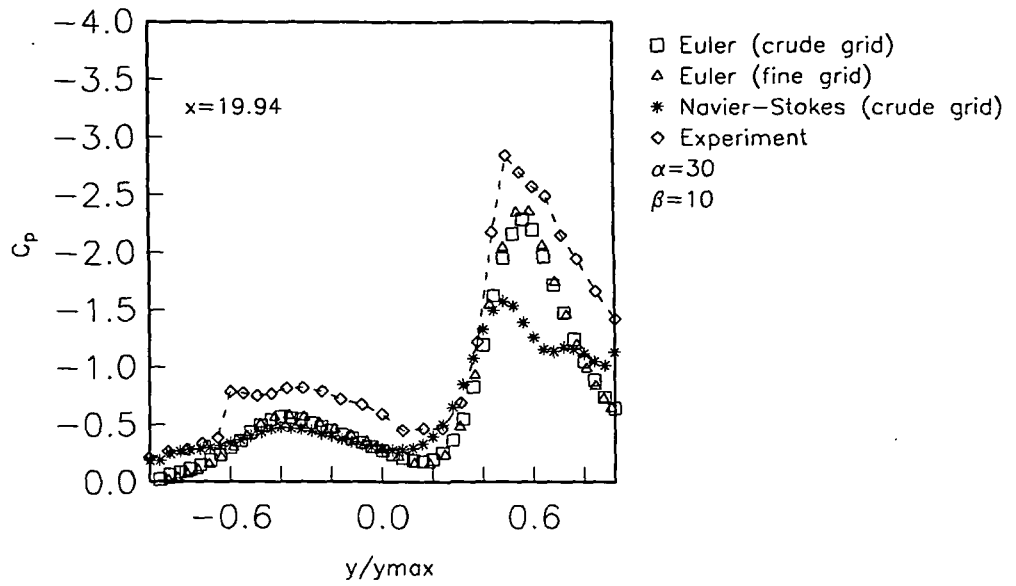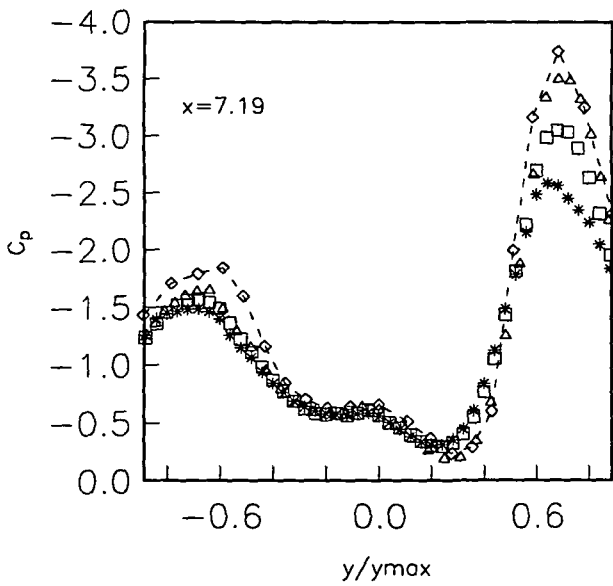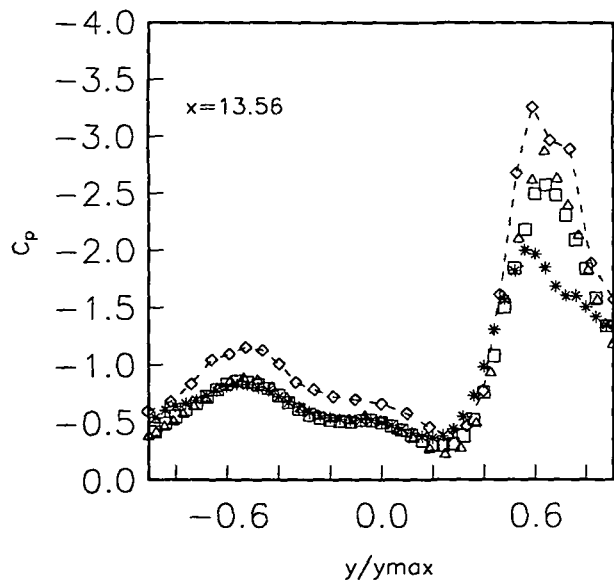
c) FS 19.94

a) FS 7.19

b) FS 13.56

Figure 23. Erickson chine forebody surface pressures at $\alpha = 30°$ and $\beta = 10°$

49
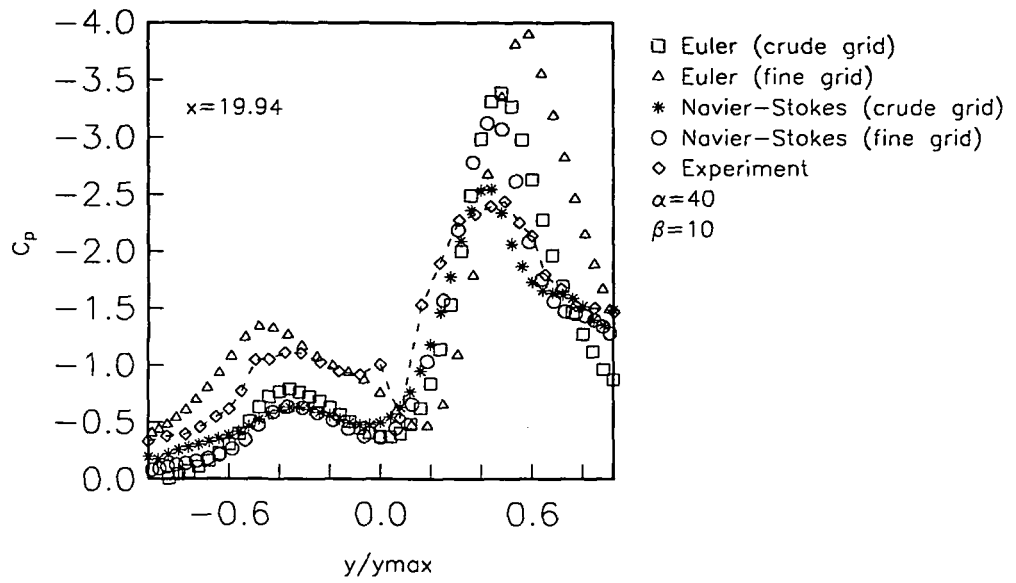
c) FS 19.94
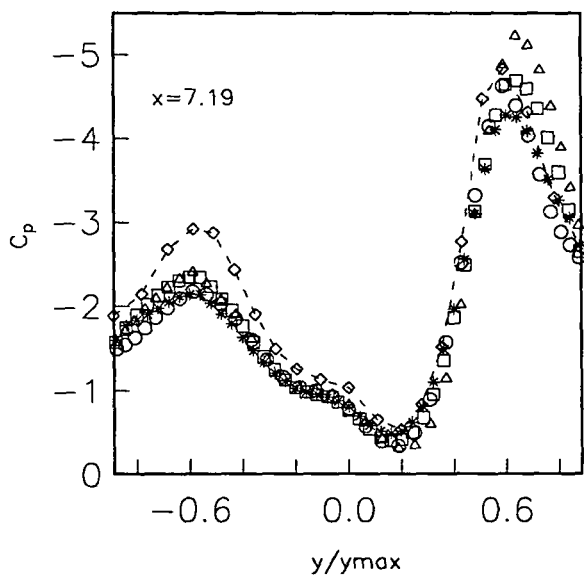
a) FS 7.19
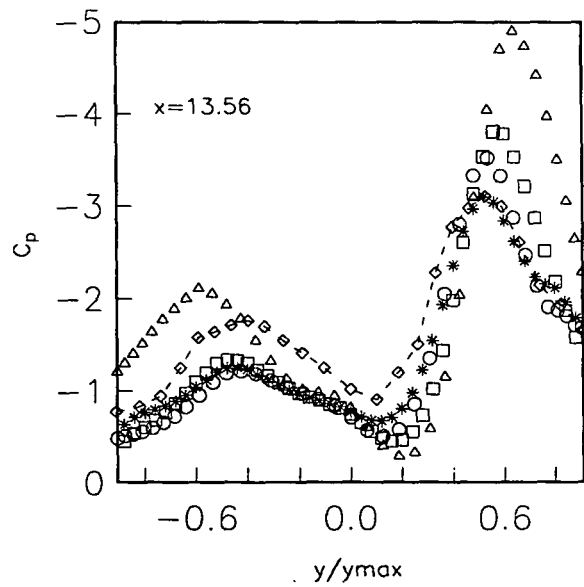
b) FS 13.56

Figure 24. Erickson chine forebody surface pressures at $\alpha = 40°$ and $\beta = 10°$
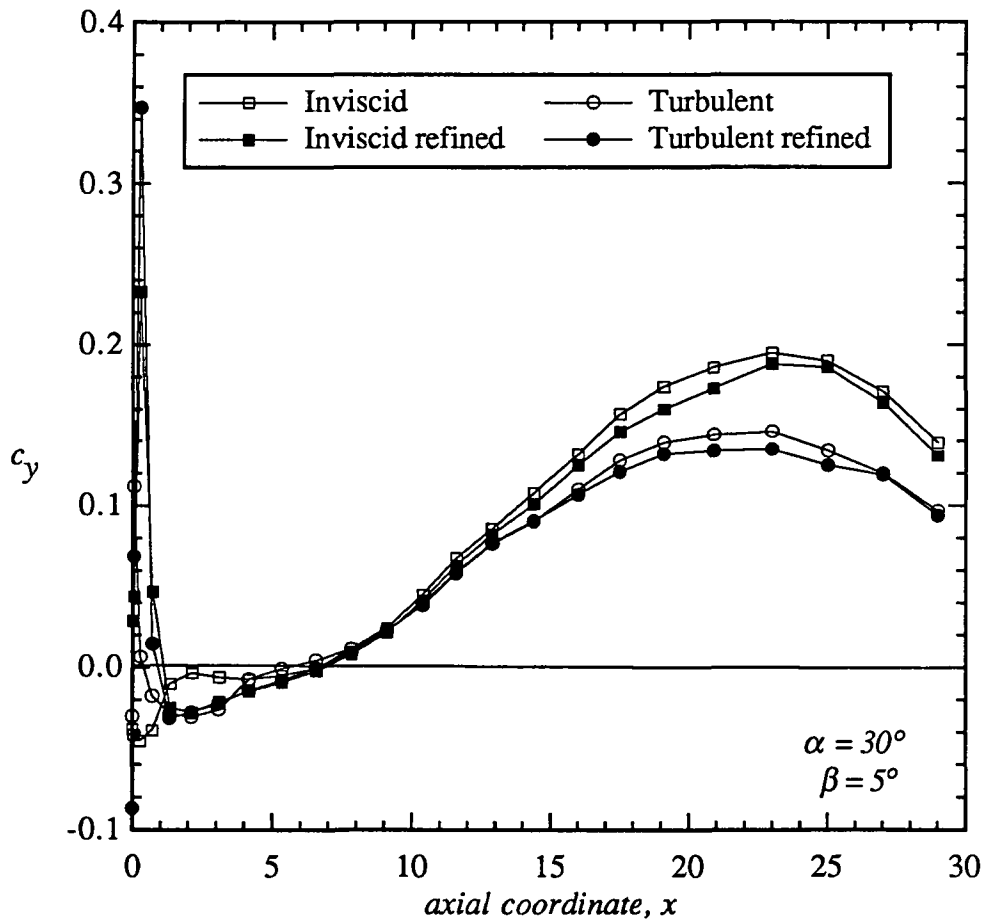
Figure 25. Erickson chine forebody side force variation along the forebody
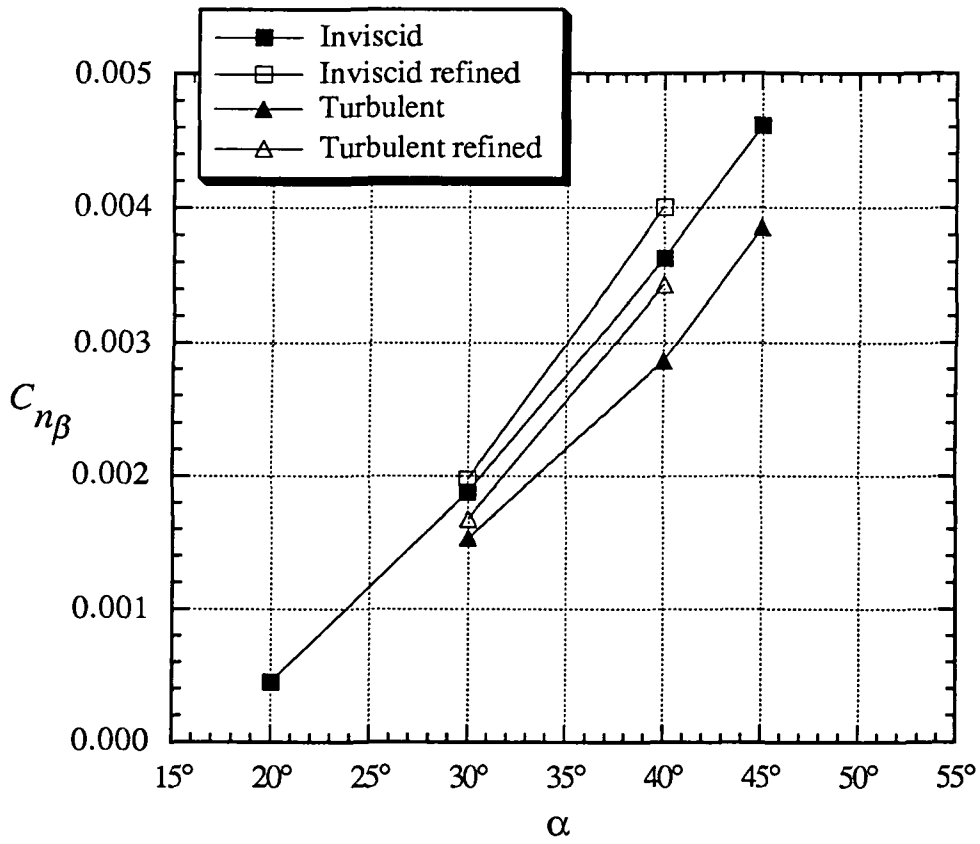
Figure 26. Erickson chine forebody directional stability characteristics
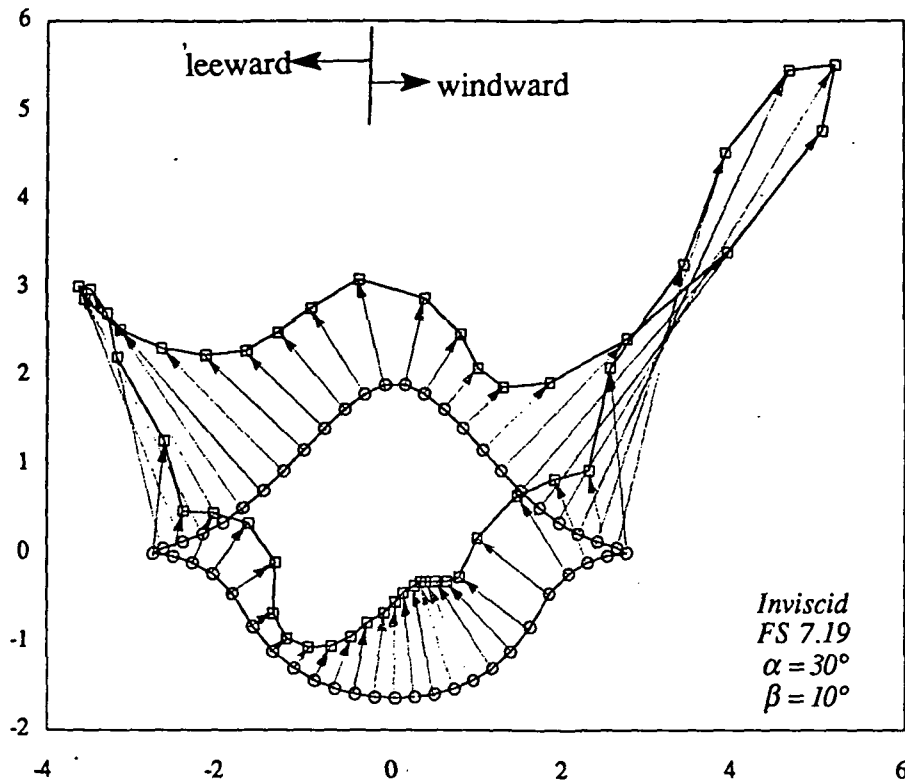
a) Inviscid
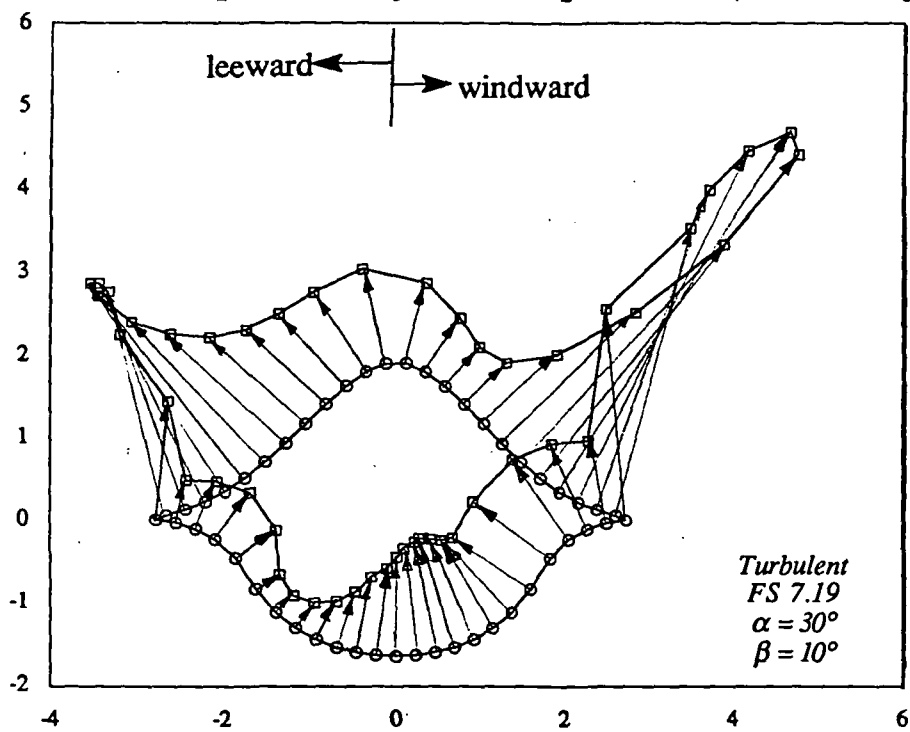
b) Turbulent

Figure 27. Erickson forebody inviscid and turbulent pressure diagrams at FS 7.19
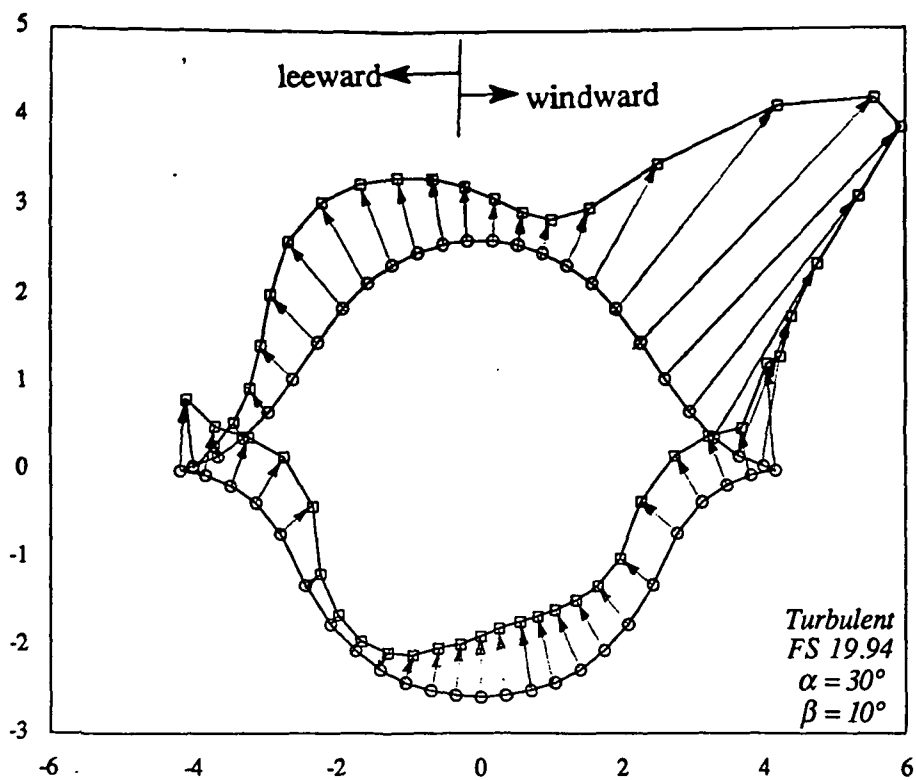
a) Turbulent
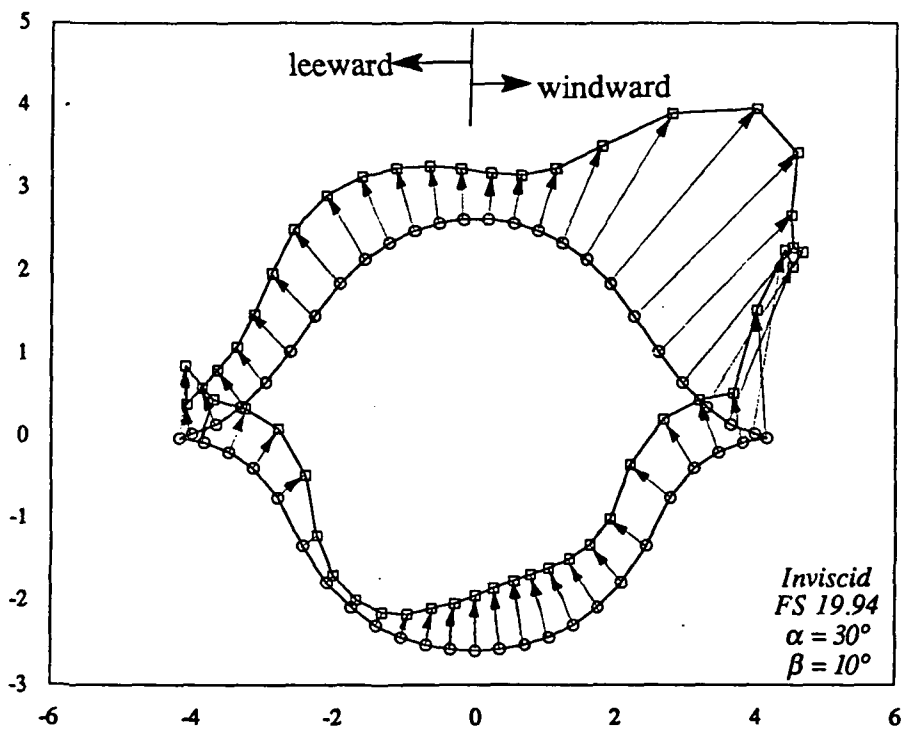
b) Inviscid

Figure 28. Erickson forebody inviscid and turbulent pressure diagrams at FS 19.94
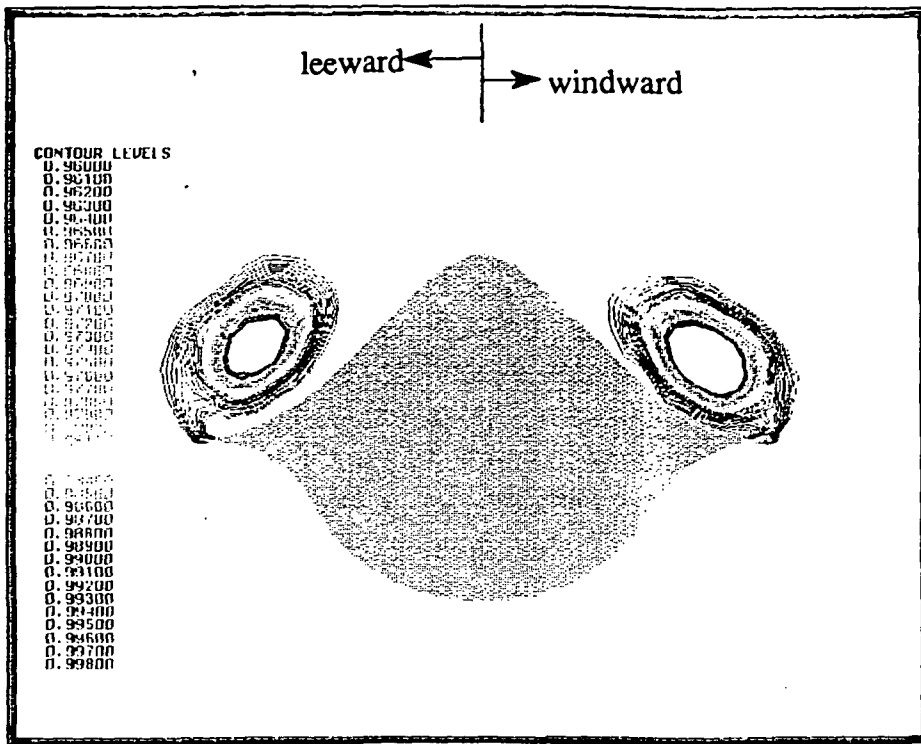
a) FS 7.19
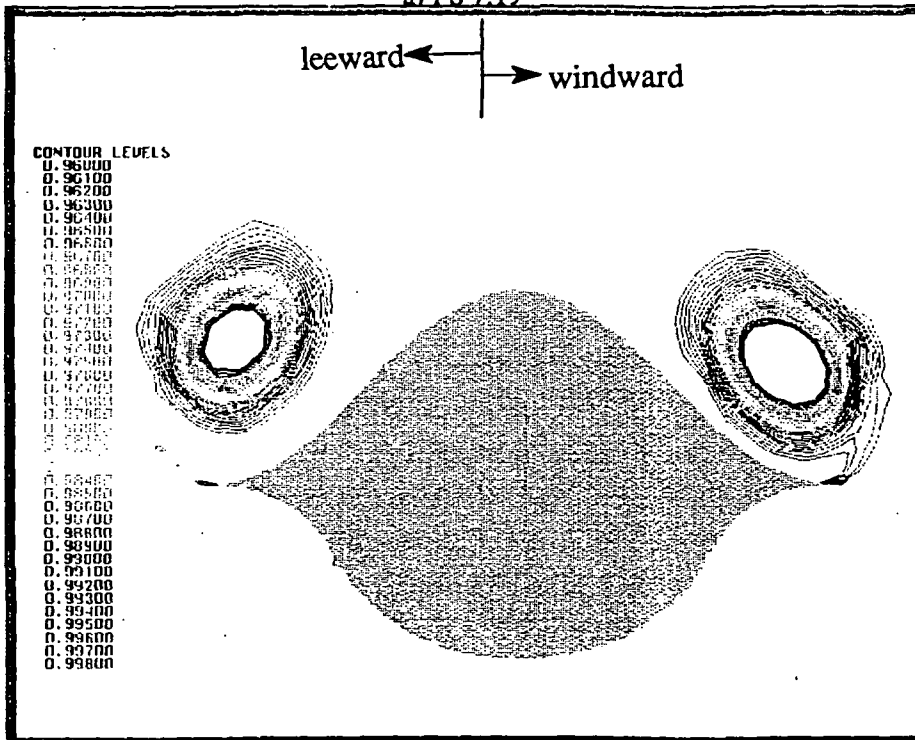
b) FS 13.56

Figure 29. Erickson forebody inviscid stagnation pressure contours for $\alpha = 30°$ and $\beta = 5°$
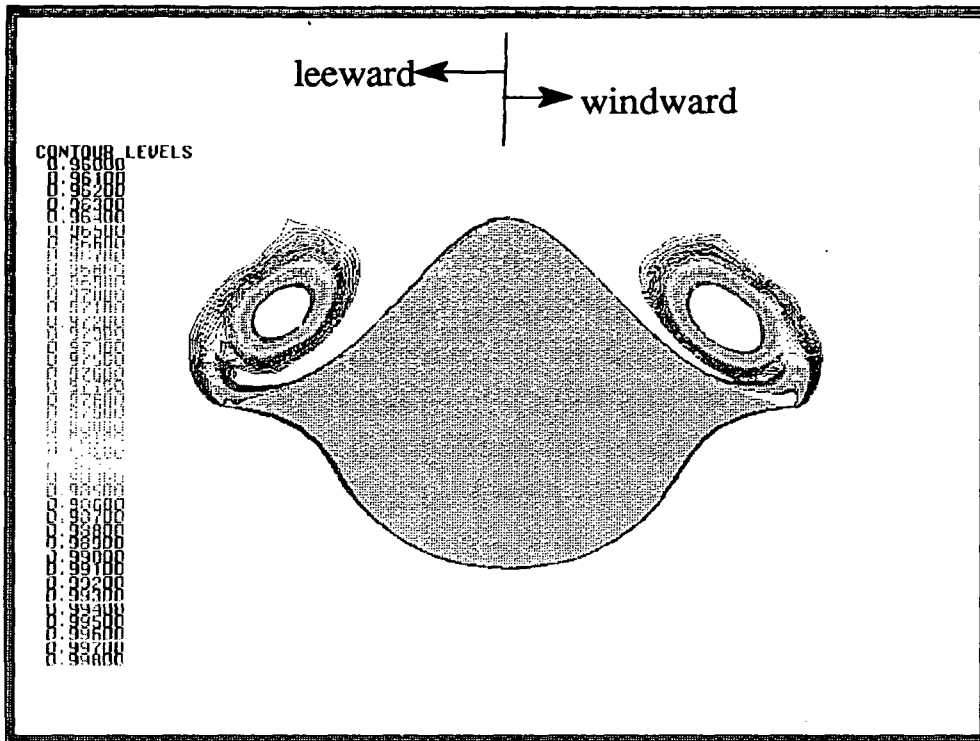
a) FS 7.19
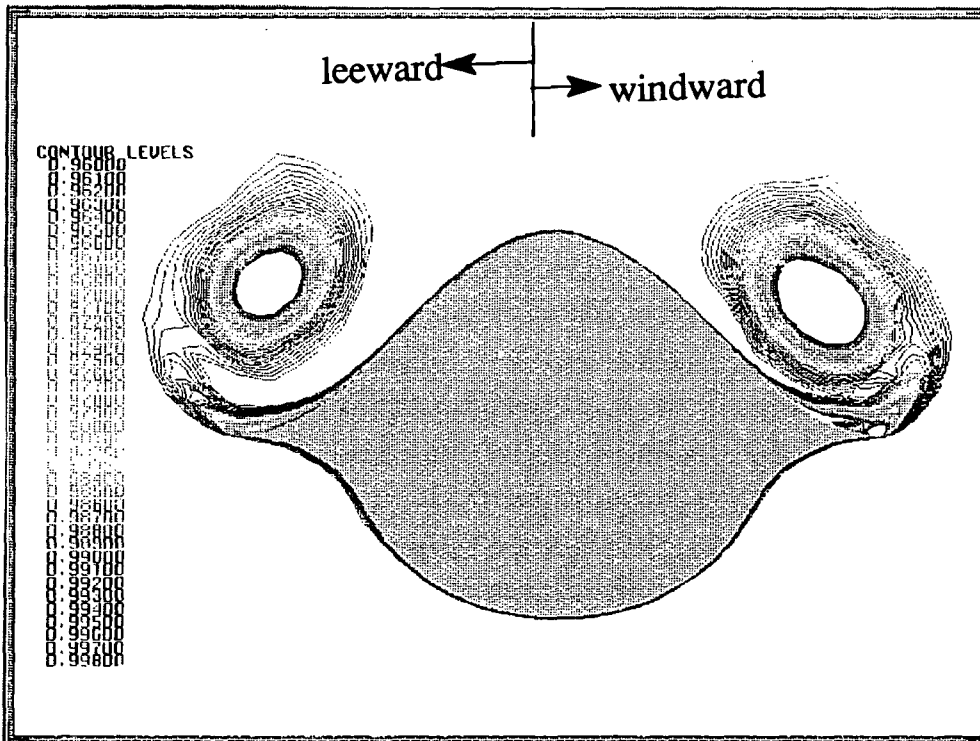
b) FS 13.56

Figure 30. Erickson forebody turbulent stagnation pressure contours for $\alpha = 30°$ and $\beta = 5°$
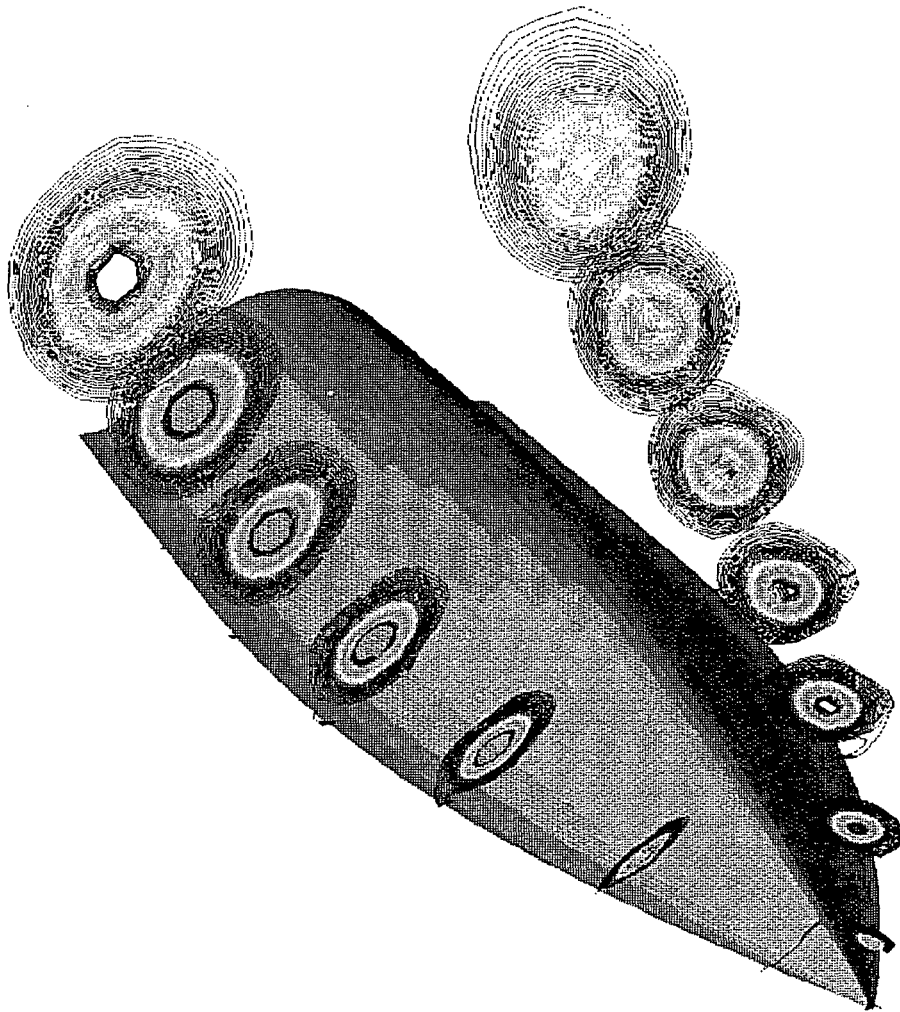
Figure 31. Erickson forebody vortex path along forebody for $\alpha = 30°$ and $\beta = 5°$
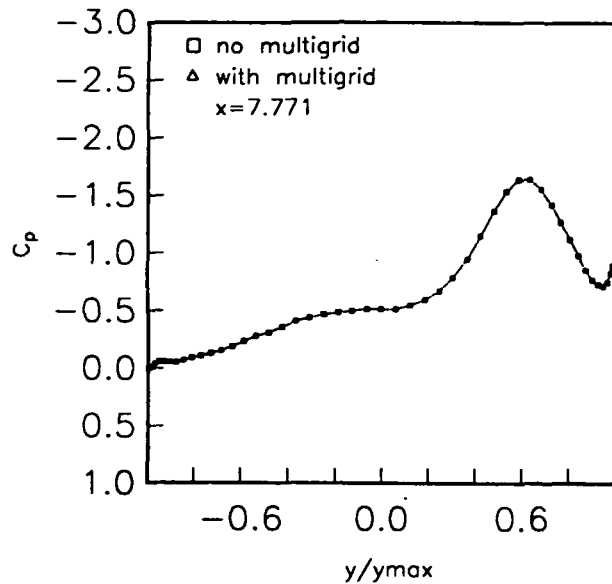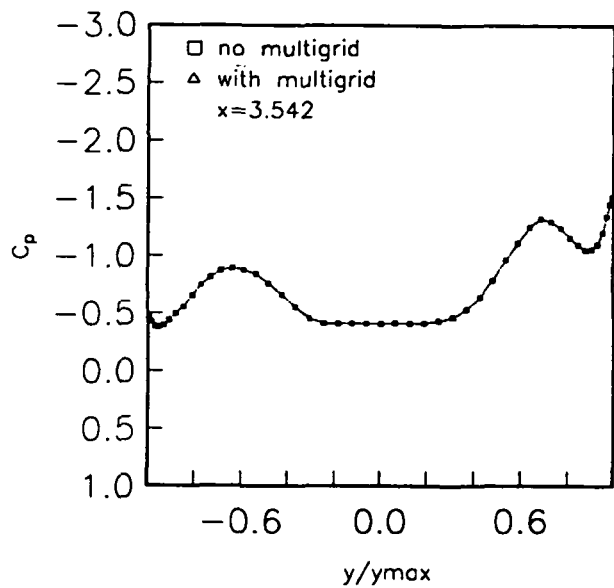
a) Upper Surface
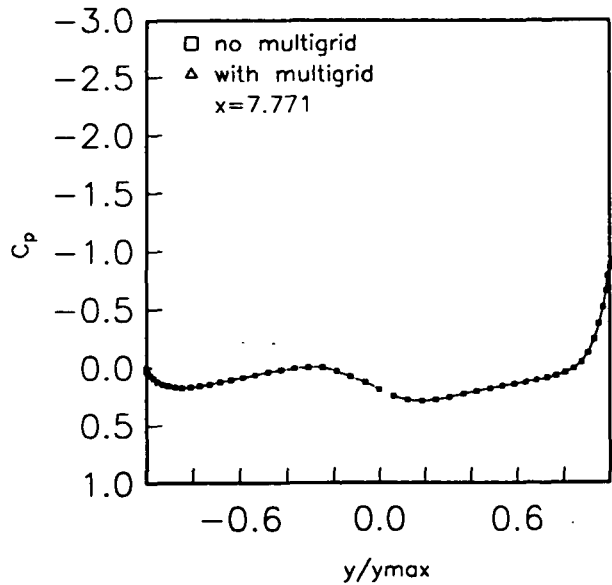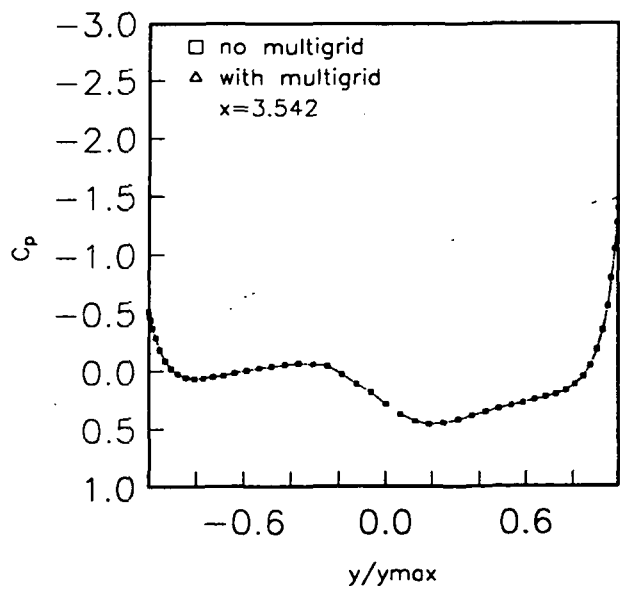
b) Lower Surface

Figure 32. Surface Pressures on a generic forebody showing effect of multigridding and multisequencing
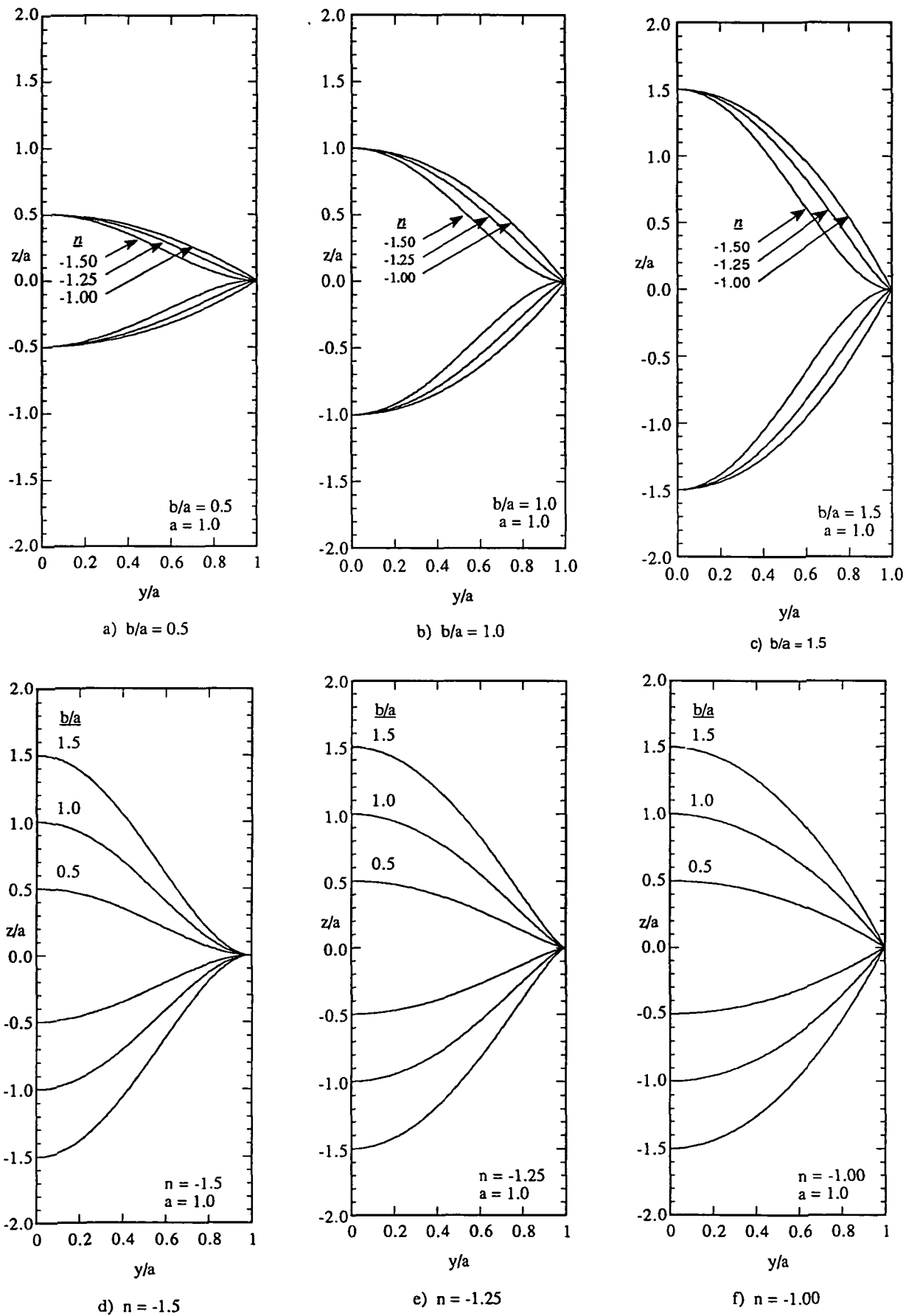
Figure 33. Cross-sections used in the present forebody design study
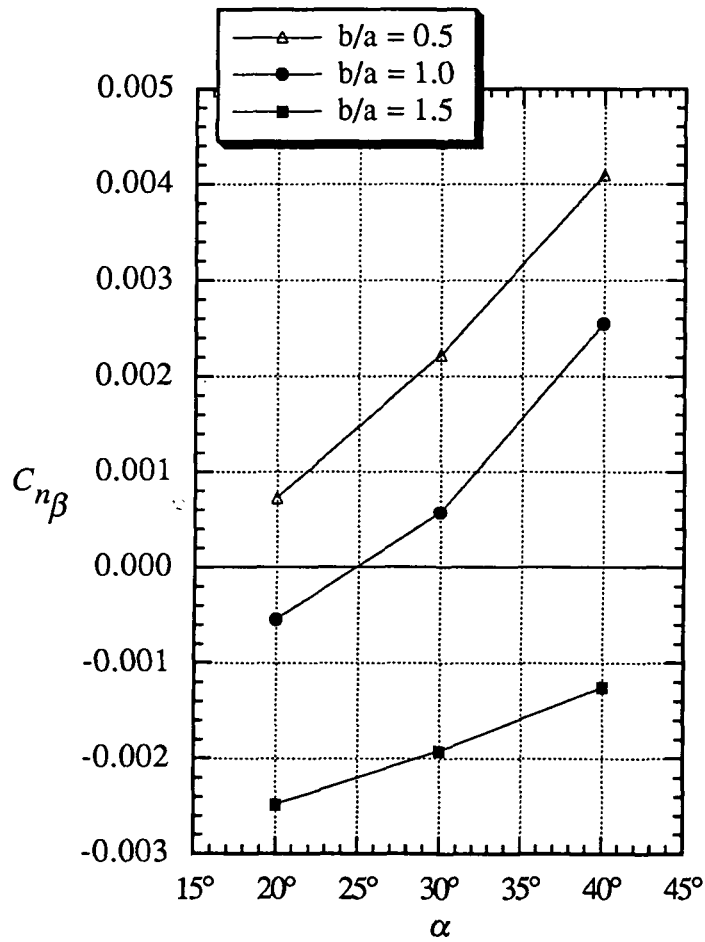
Figure 34. Effect of varying *b/a* on the directional stability characteristics
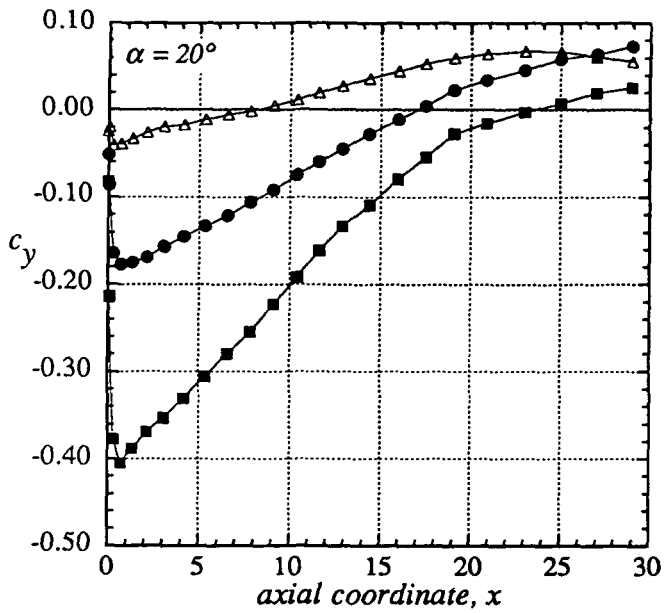
a) $\alpha = 20°$
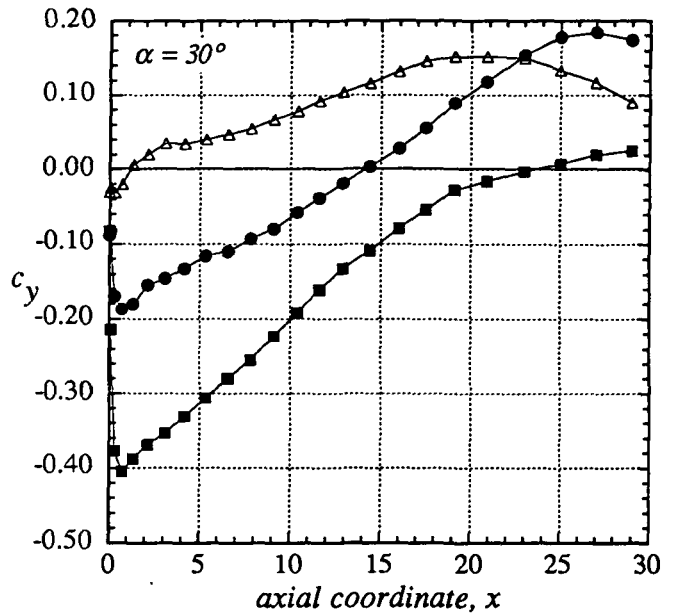
b) $\alpha = 30°$
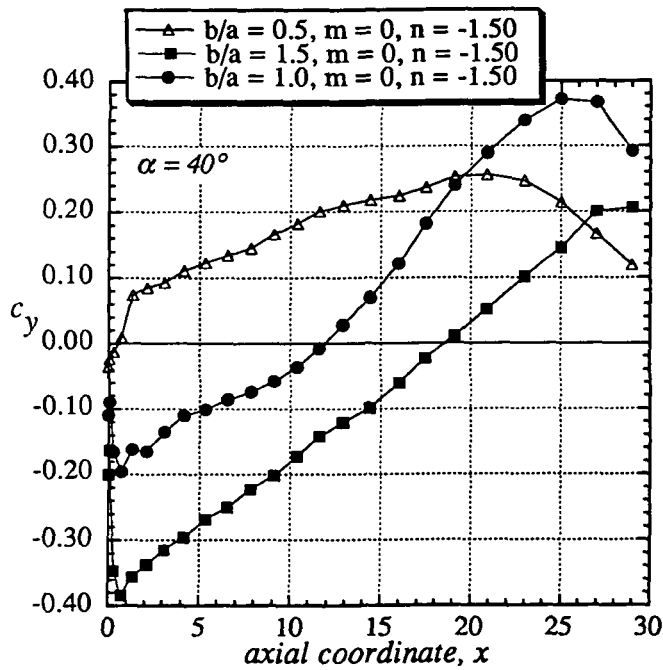
c) $\alpha = 40°$

Figure 35. Effect of varying b / a on side force at various angles of attack
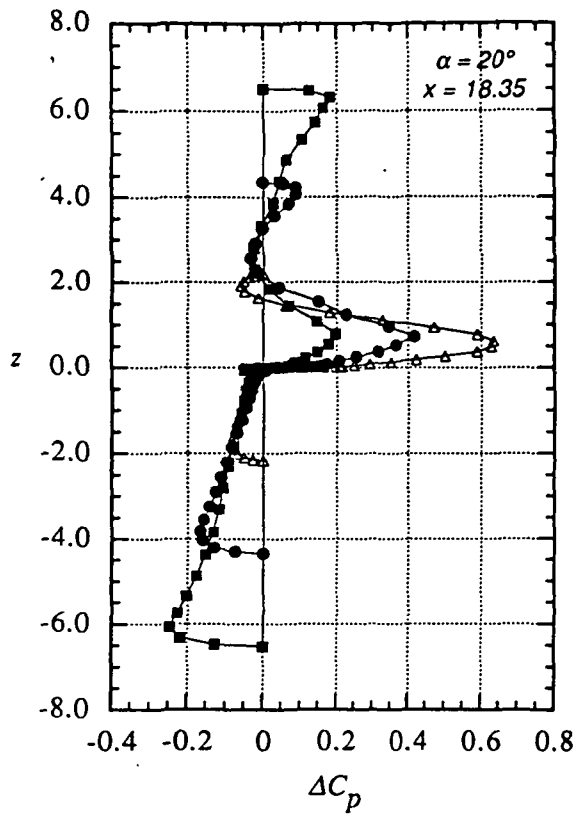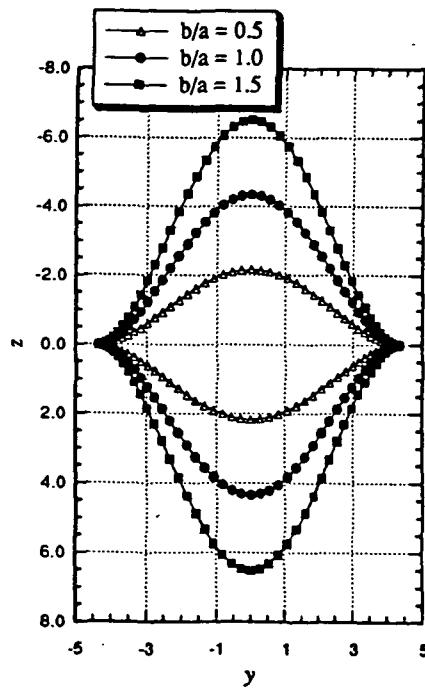
a) ΔC_p distribution

b) geometry variation

Figure 36. Effect of varying b/a on the variation of ΔC_p at $\alpha = 20°$
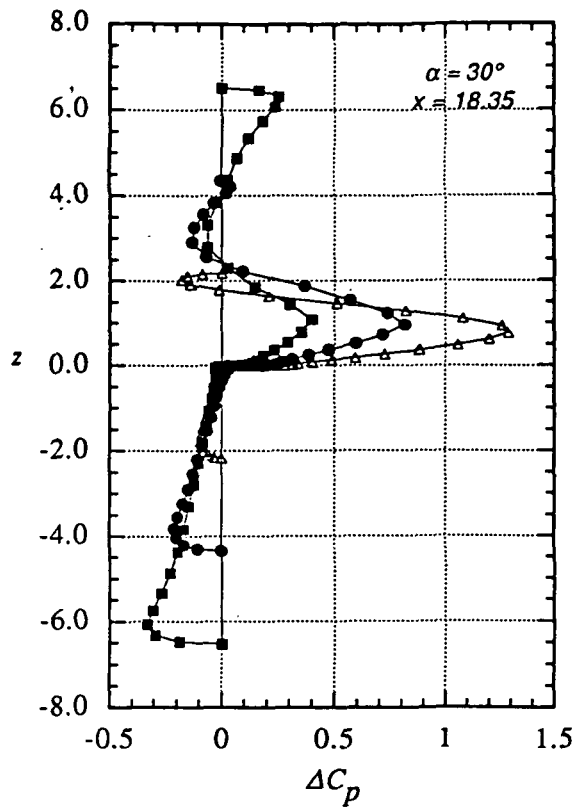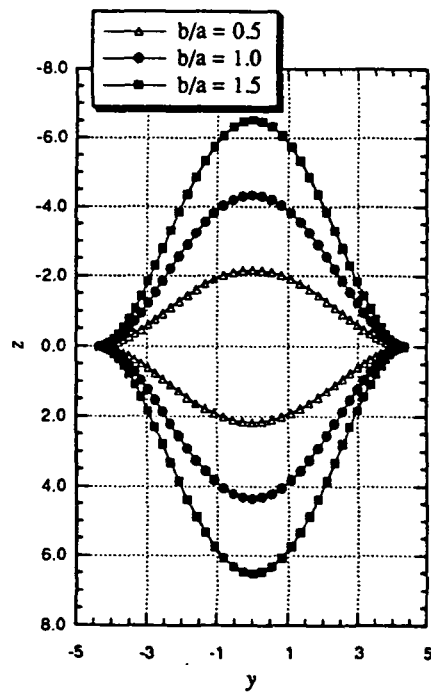
a) ΔC_p distribution

b) geometry variation

Figure 37. Effect of varying b/a on the variation of ΔC_p at $\alpha = 30°$
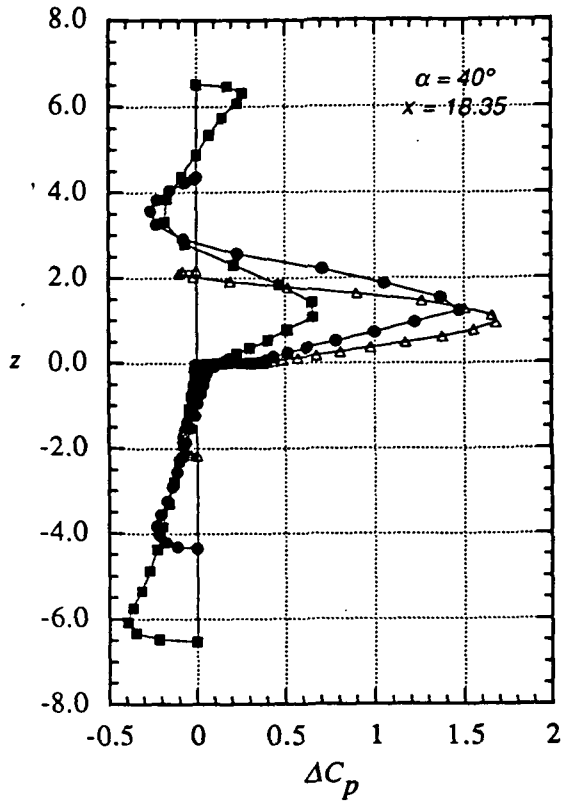
a) ΔC_p distribution
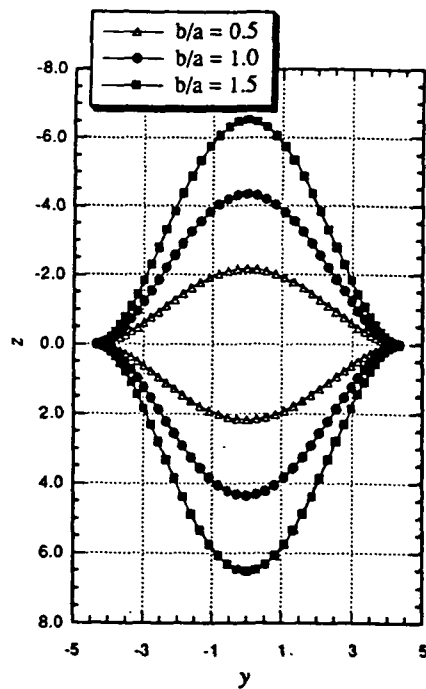
b) geometry variation

Figure 38. Effect of varying b/a on the variation of ΔC_p at $\alpha = 40°$
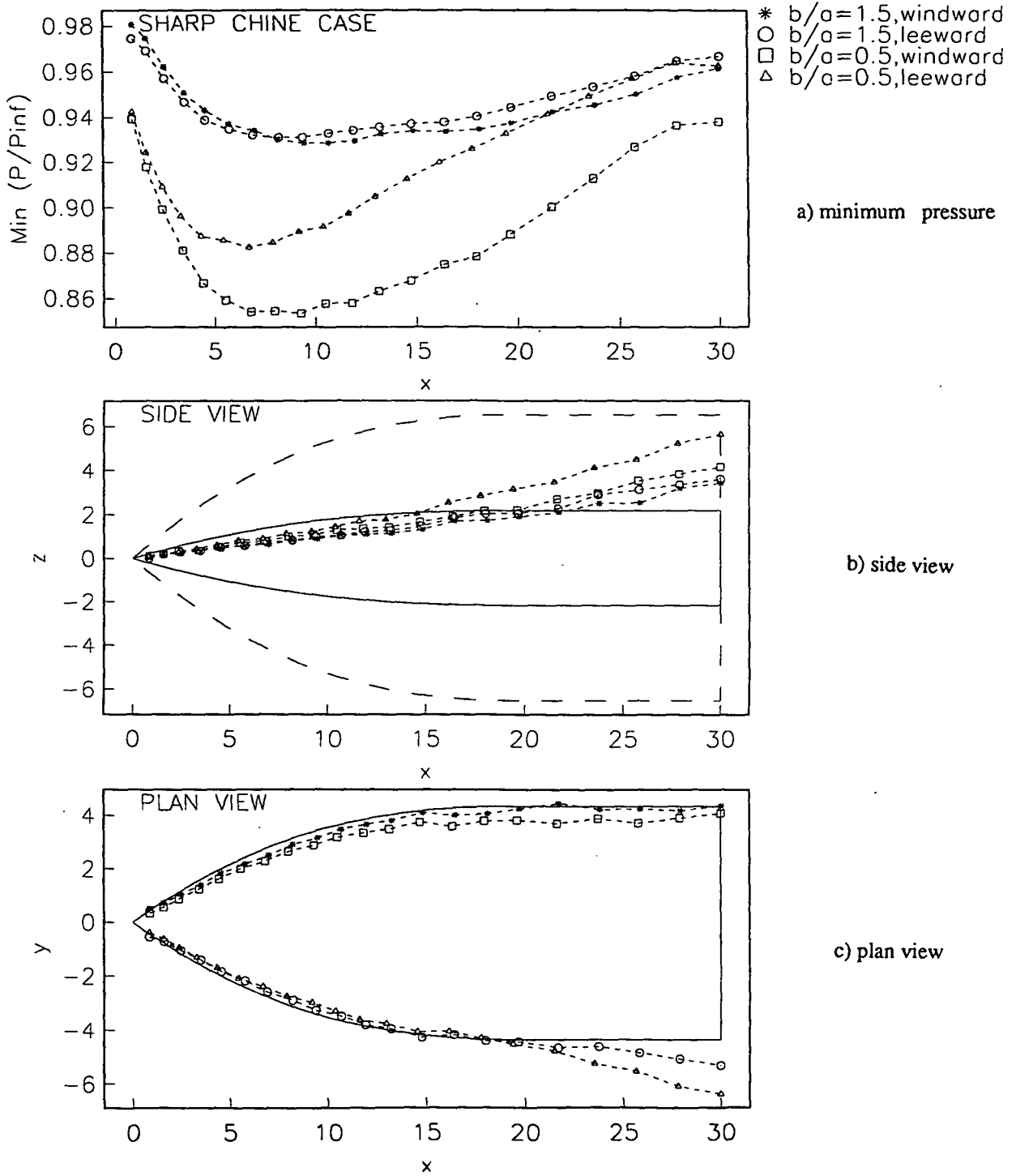
Figure 39. Vortex position and strength variation with *b/a* at $\alpha = 30°$
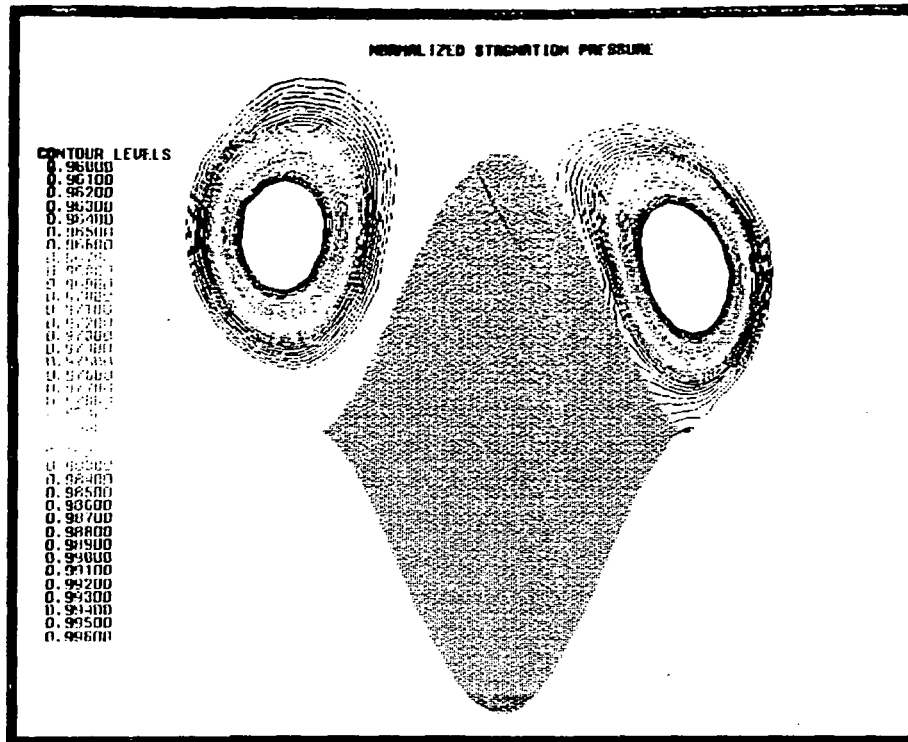
a) $b / a = 1.5$
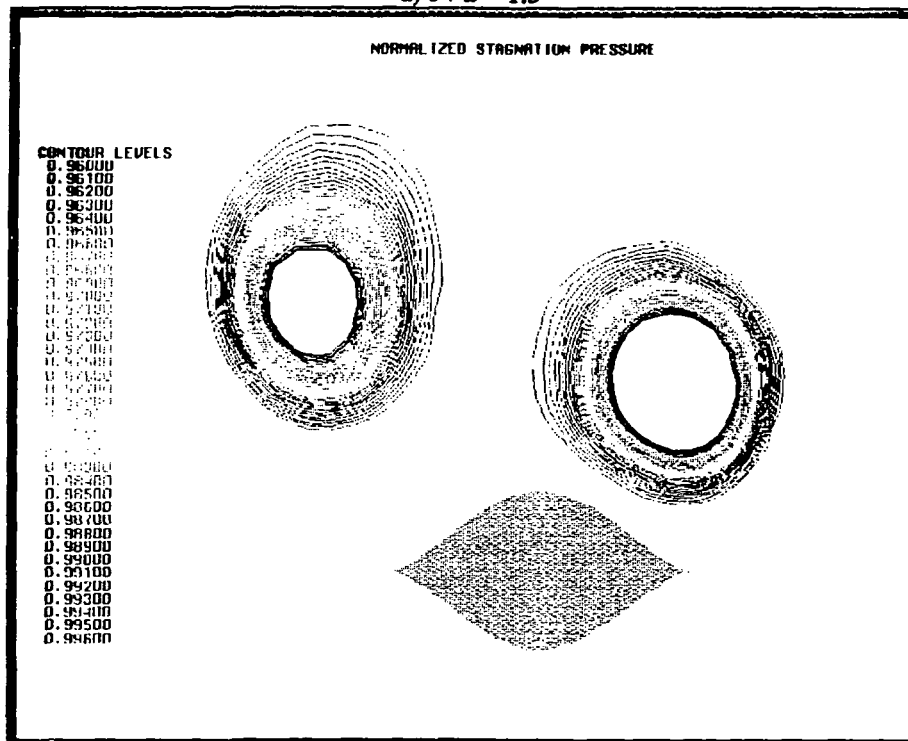
b) $b / a = 0.5$

Figure 40. Stagnation pressure contours for $\alpha = 40°$ and $\beta = 5°$ at $x = 27.99$ *in.*
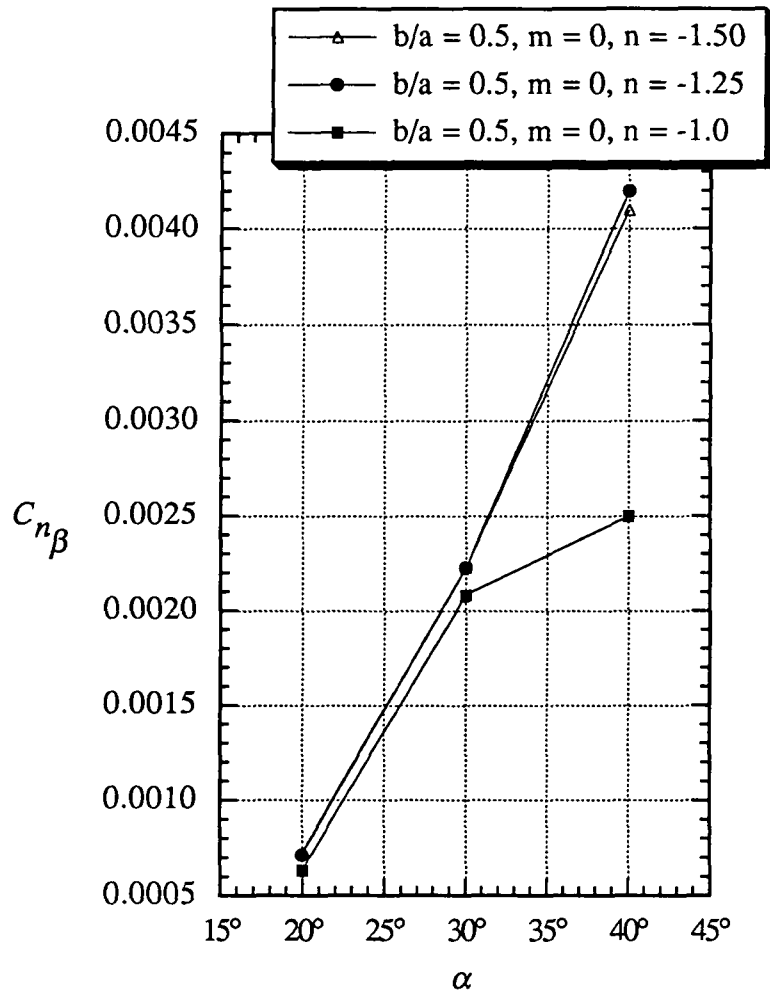
Figure 41. Effect of varying chine angle on the directional stability characteristics for $b/a = 0.5$.
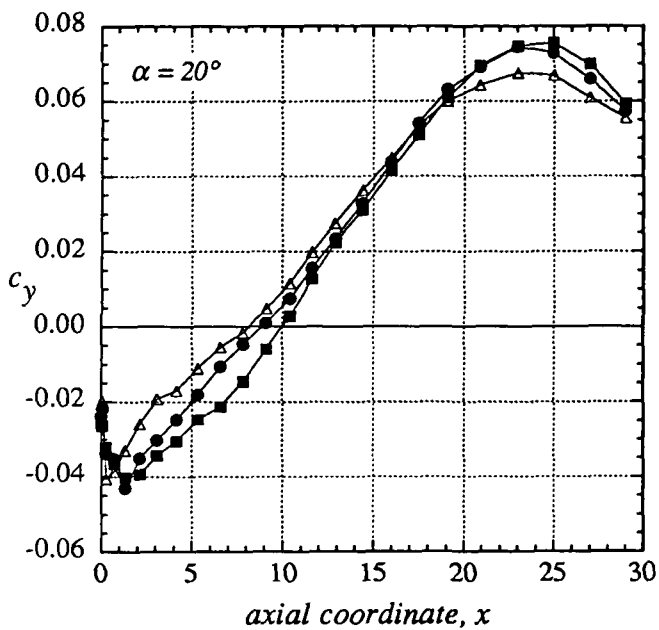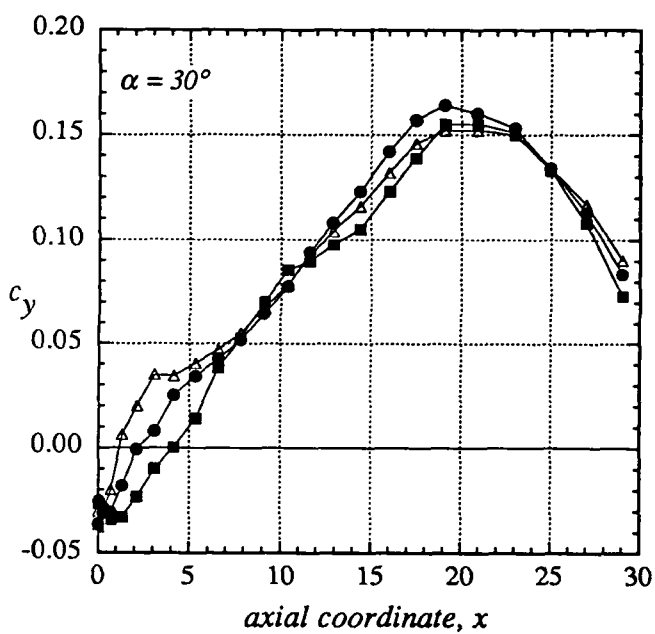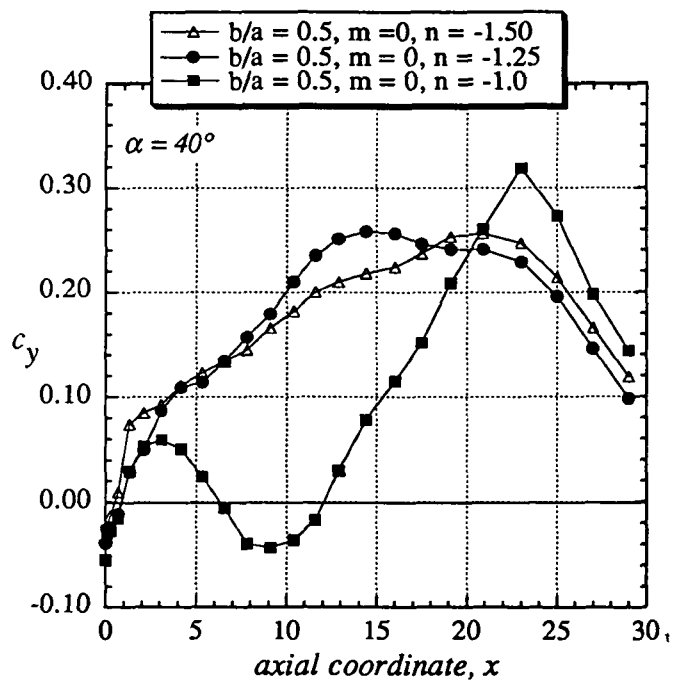
Figure 42. Effect of varying chine angle on side force at various angles of attack for $b / a = 0.5$
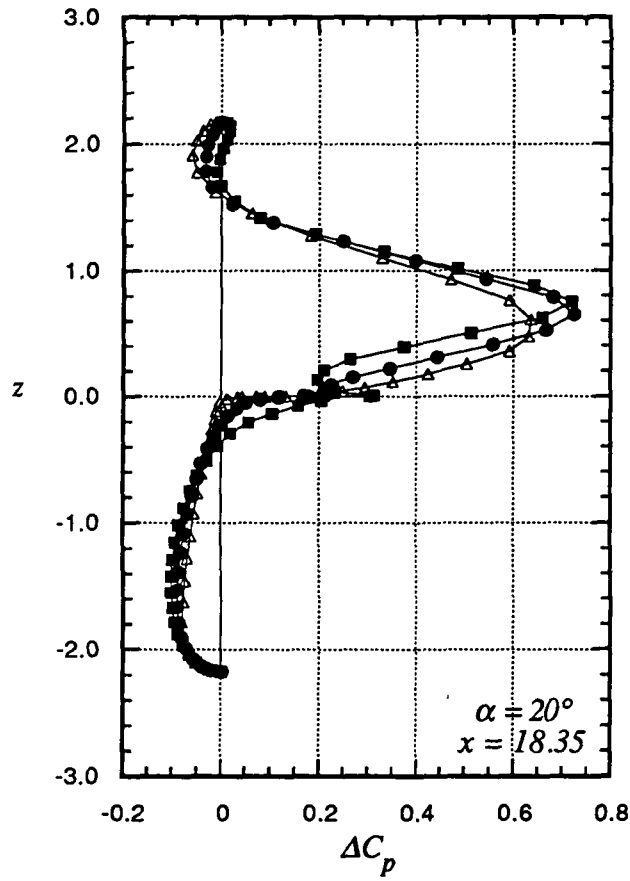
a) ΔC_p distribution
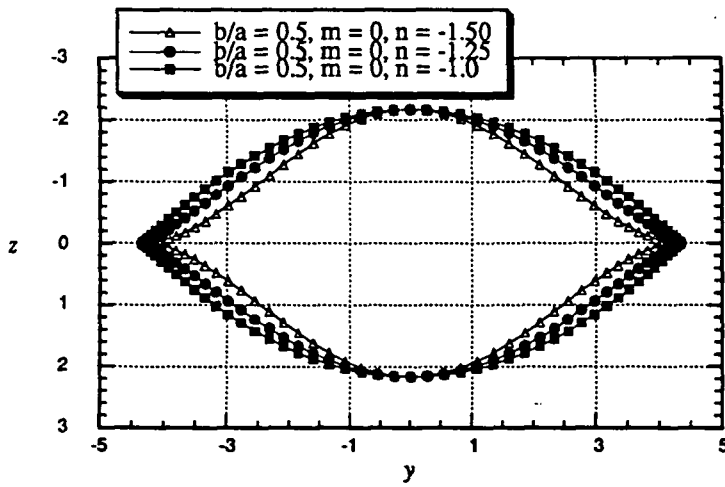
b) geometry variation

Figure 43. Effect of varying chine angle on the variation of ΔC_p at $\alpha = 20°$

a) ΔC_p distribution

$\alpha = 30°$
$x = 18.35$

b) geometry variation

b/a = 0.5, m = 0, n = -1.50
b/a = 0.3, m = 0, n = -1.25
b/a = 0.3, m = 0, n = -1.0
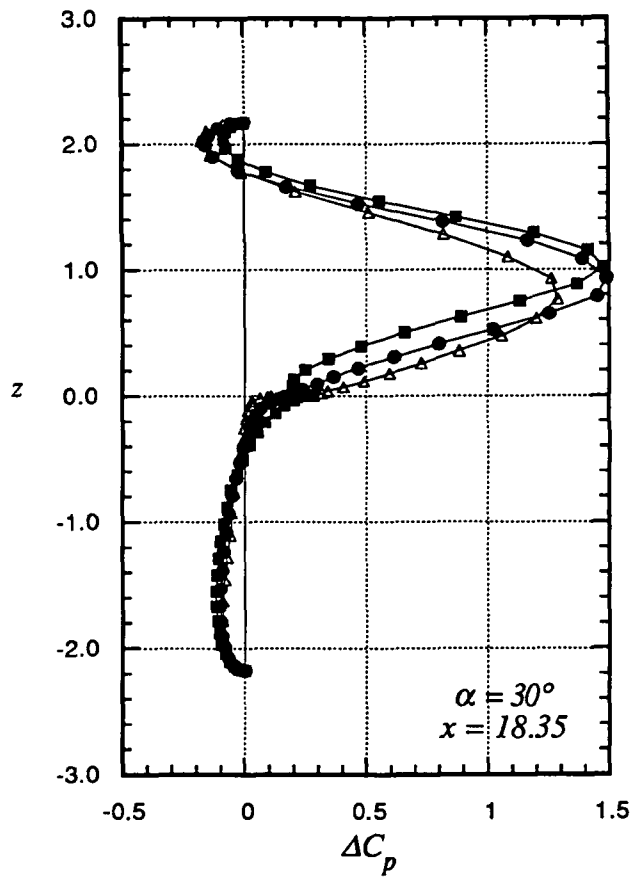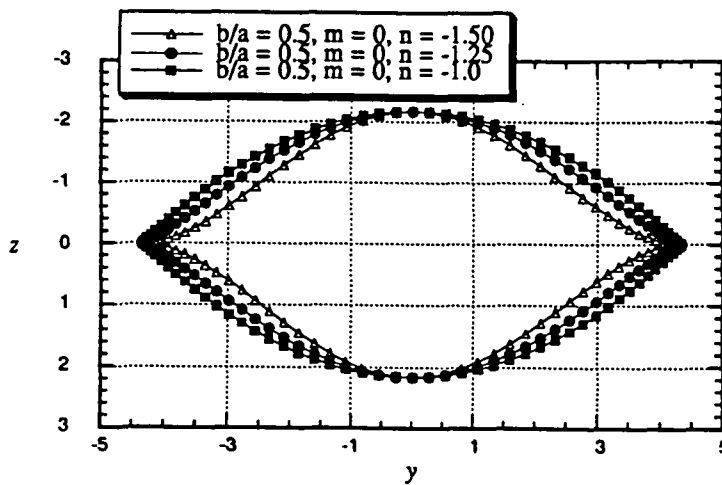
Figure 44. Effect of varying chine angle on the variation of ΔC_p at $\alpha = 30°$

a) ΔC_p distribution

$\alpha = 40°$
$x = 18.35$

b/a = 0.5, m = 0, n = -1.50
b/a = 0.3, m = 0, n = -1.25
b/a = 0.3, m = 0, n = -1.0
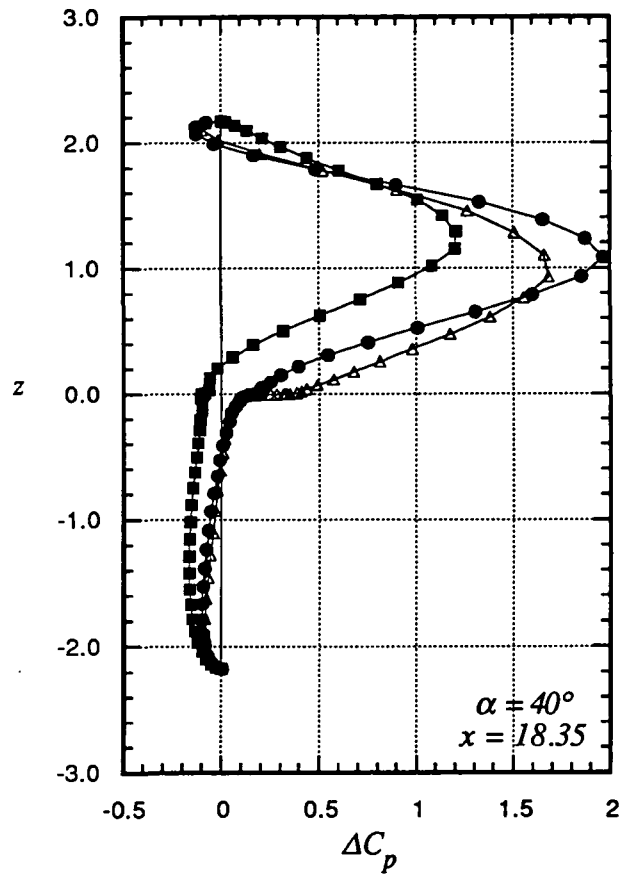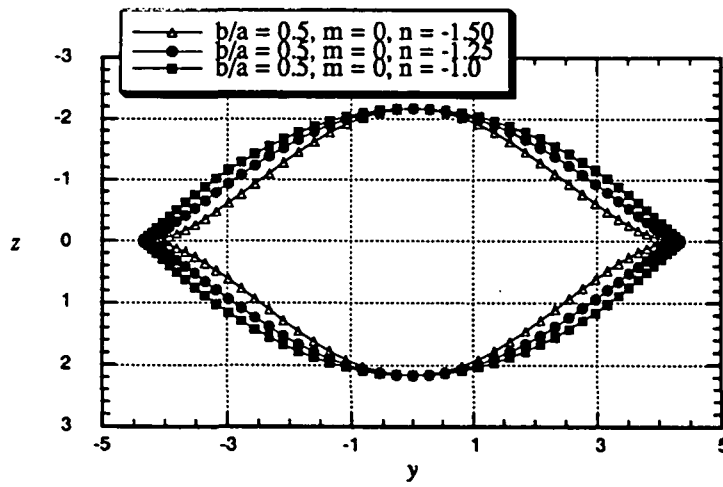
b) geometry variation

Figure 45. Effect of varying chine angle on the variation of ΔC_p at $\alpha = 40°$
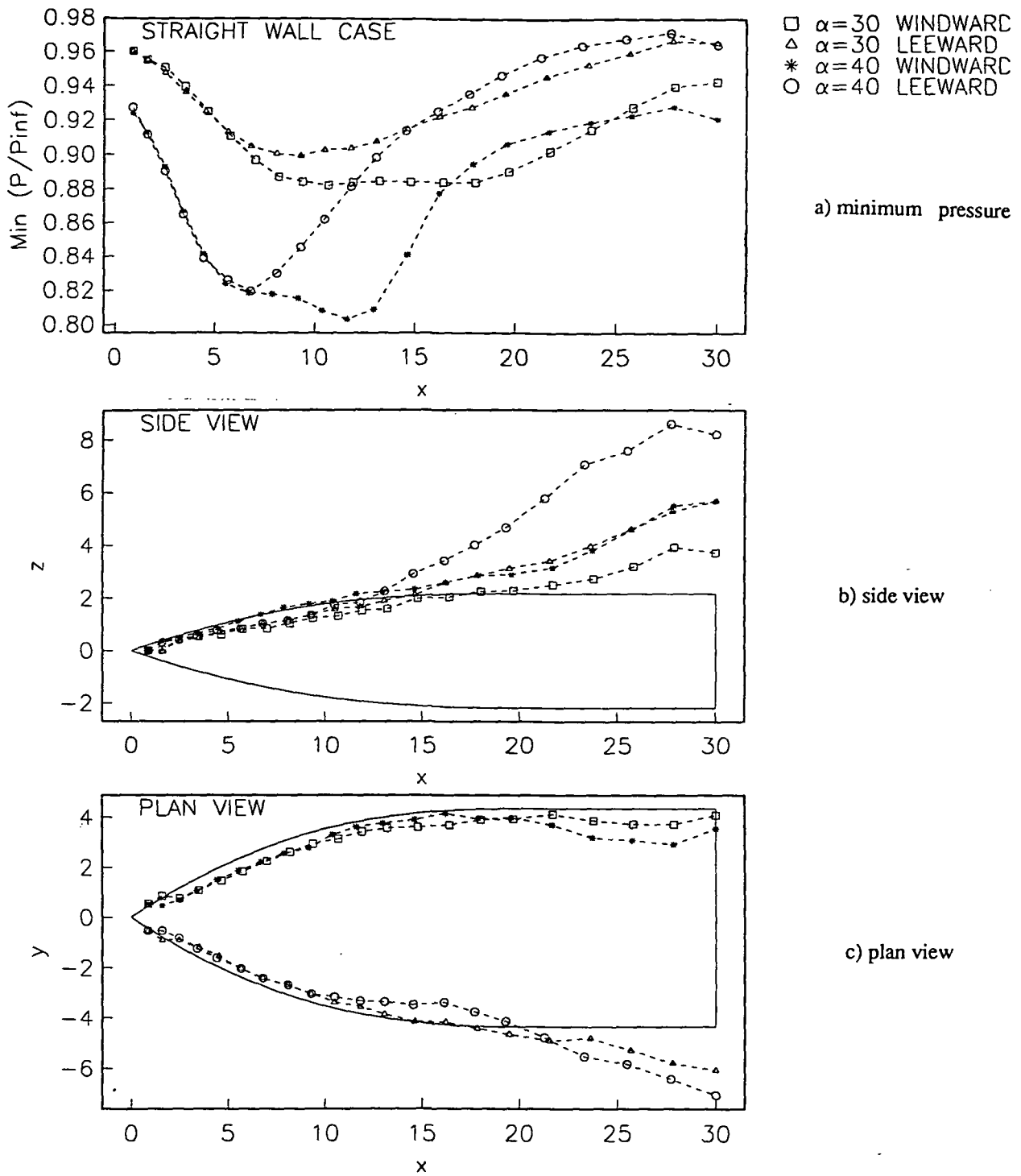
Figure 46. Vortex position and strength comparison between $\alpha = 30°$ and $\alpha = 40°$

72
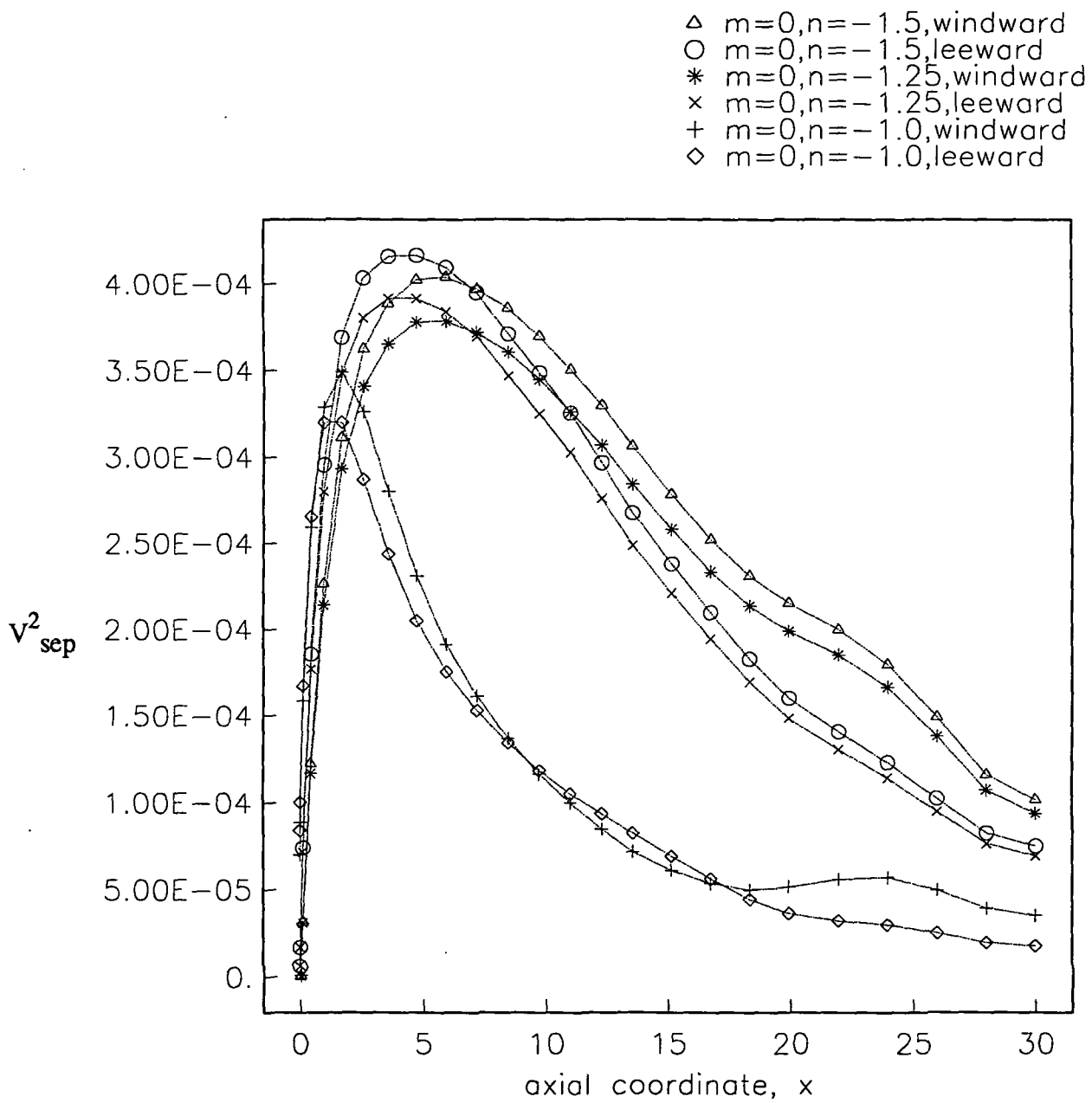
Figure 47. Comparison of square of velocity at separation for $\alpha = 40°$ for various chine angles

The legend for the figure reads:

- $\triangle$ m=0,n=−1.5,windward
- $\bigcirc$ m=0,n=−1.5,leeward
- $*$ m=0,n=−1.25,windward
- $\times$ m=0,n=−1.25,leeward
- $+$ m=0,n=−1.0,windward
- $\diamond$ m=0,n=−1.0,leeward

The vertical axis is labeled V^2_{sep} with values 0., 5.00E−05, 1.00E−04, 1.50E−04, 2.00E−04, 2.50E−04, 3.00E−04, 3.50E−04, 4.00E−04.

The horizontal axis is labeled "axial coordinate, x" with values 0, 5, 10, 15, 20, 25, 30.
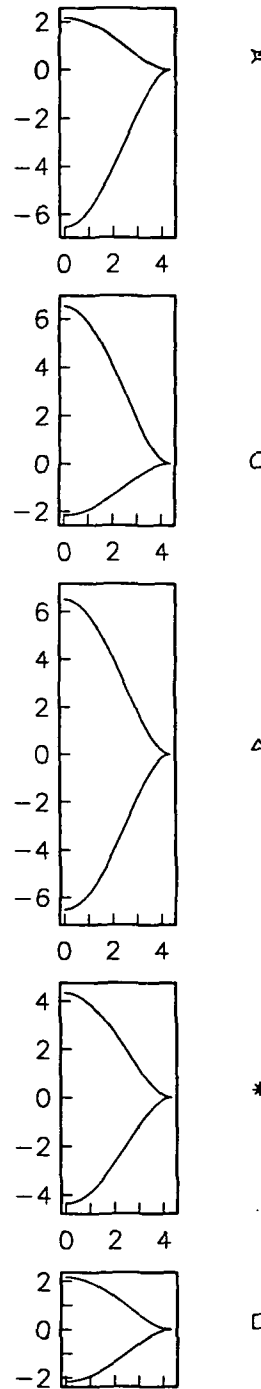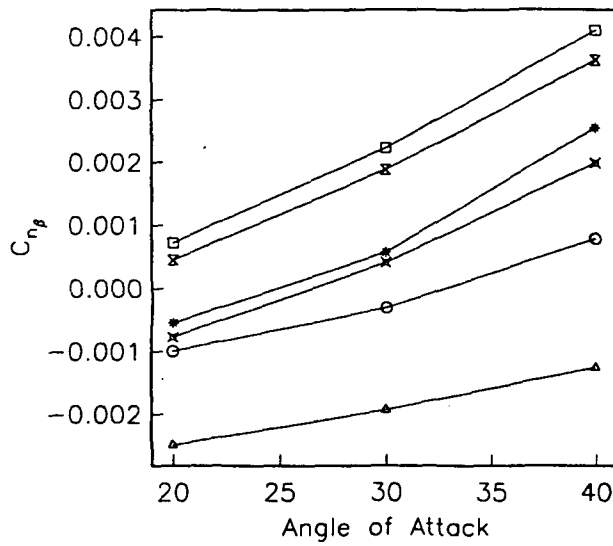
Figure 48. Effect of unsymmetrical *b/a* on the directional stability characteristics
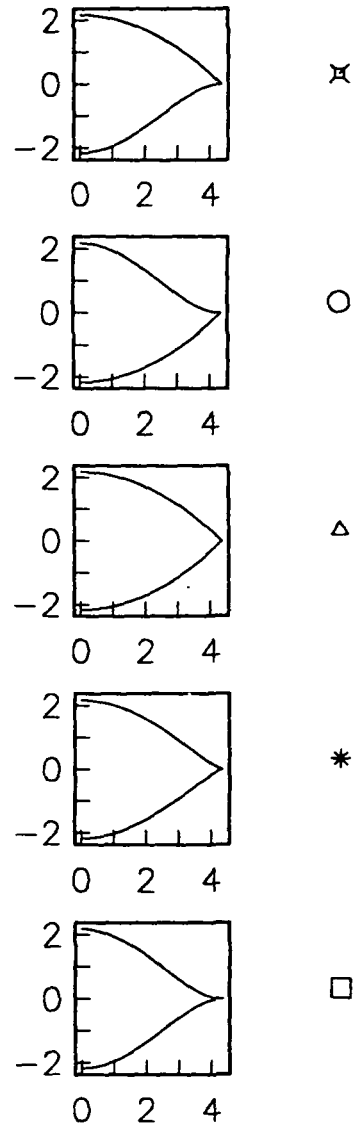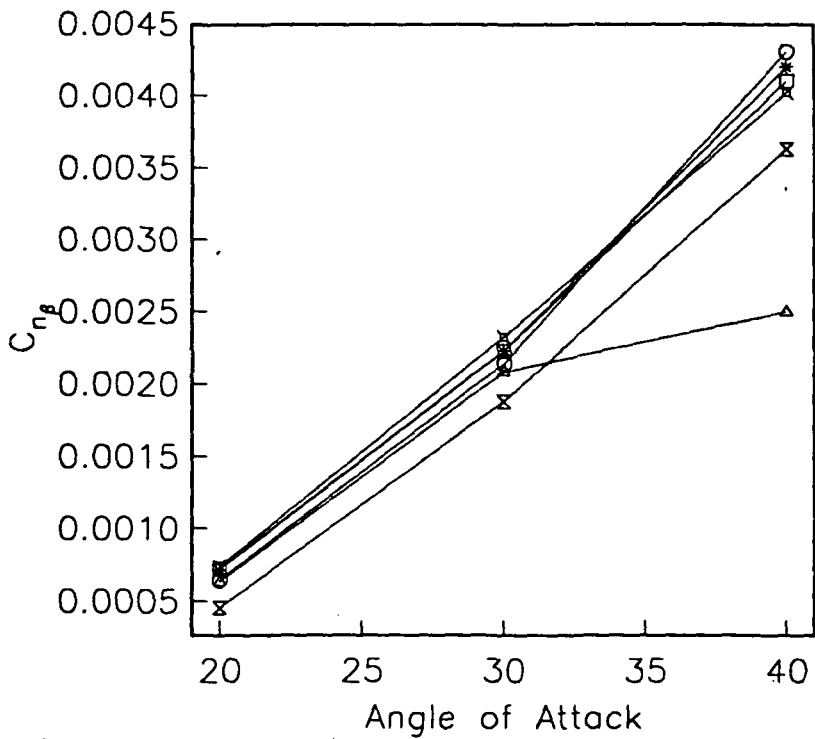
Figure 49. Effect of unsymmetrical shape factor n on the directional stability characteristics
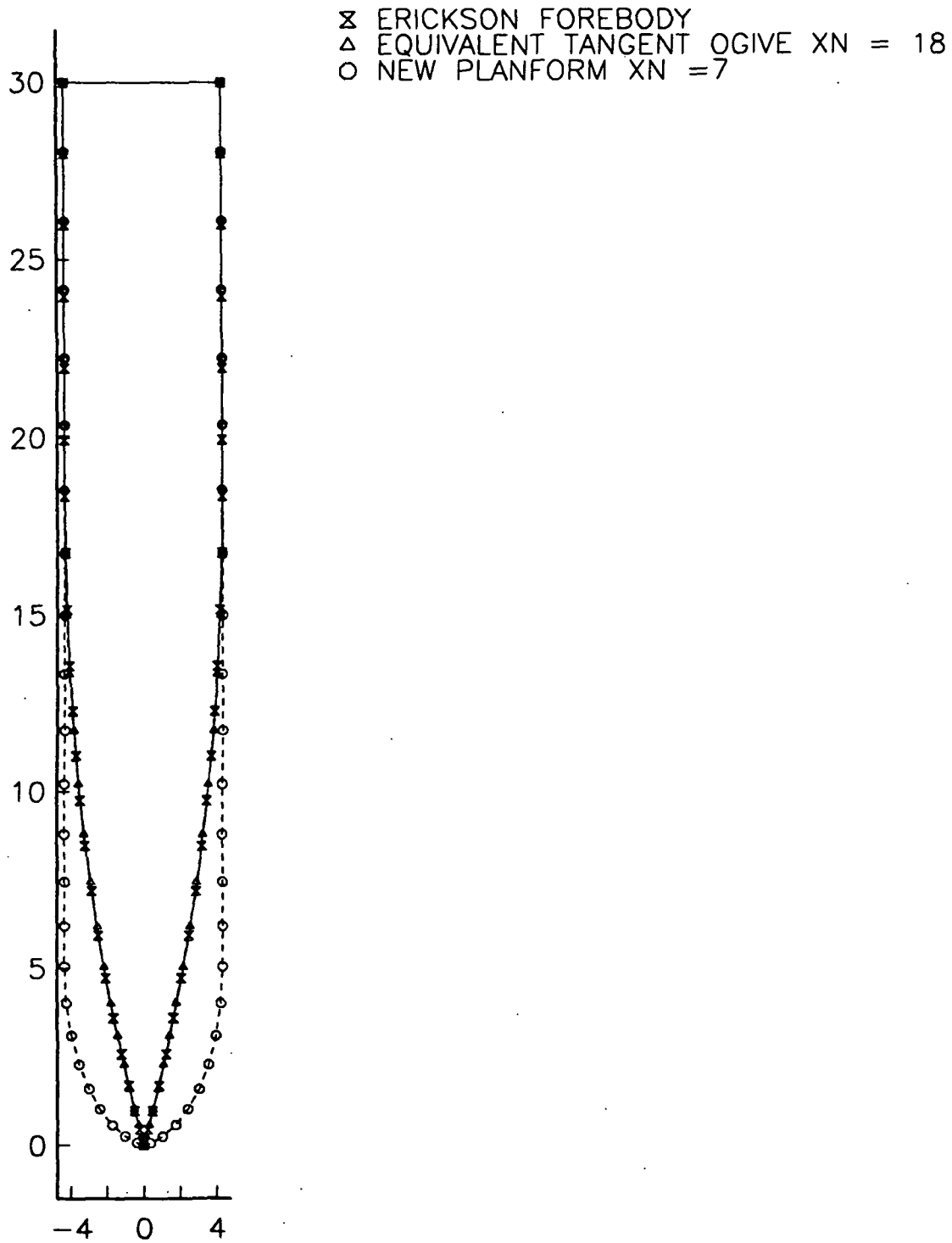
Figure 50. Planform shapes used in this study
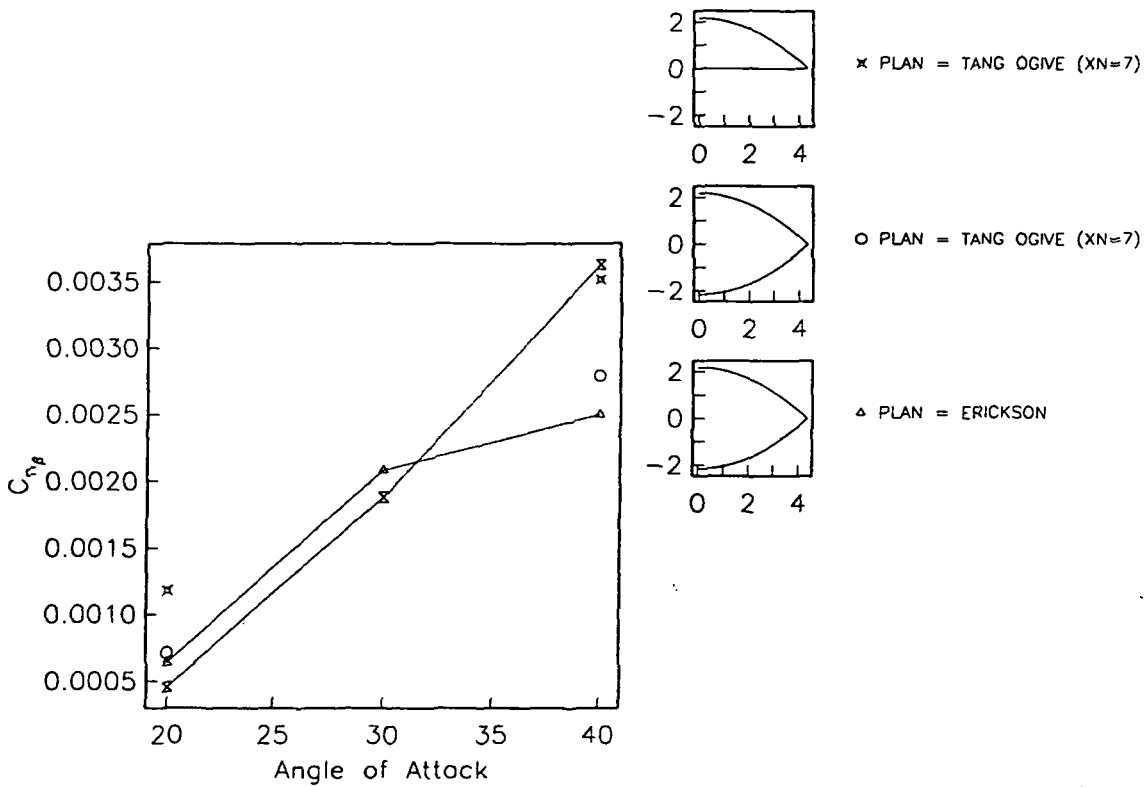
Figure 51. Effect of planform shape variation on the directional stability characteristics
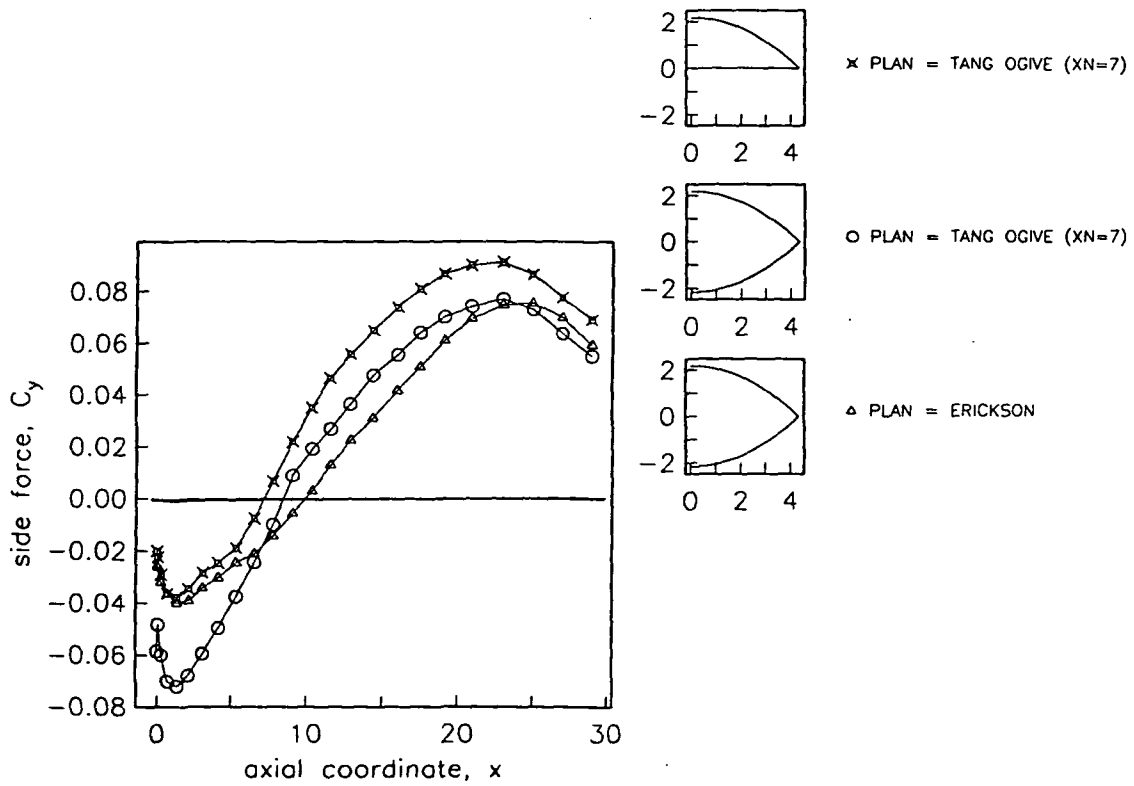
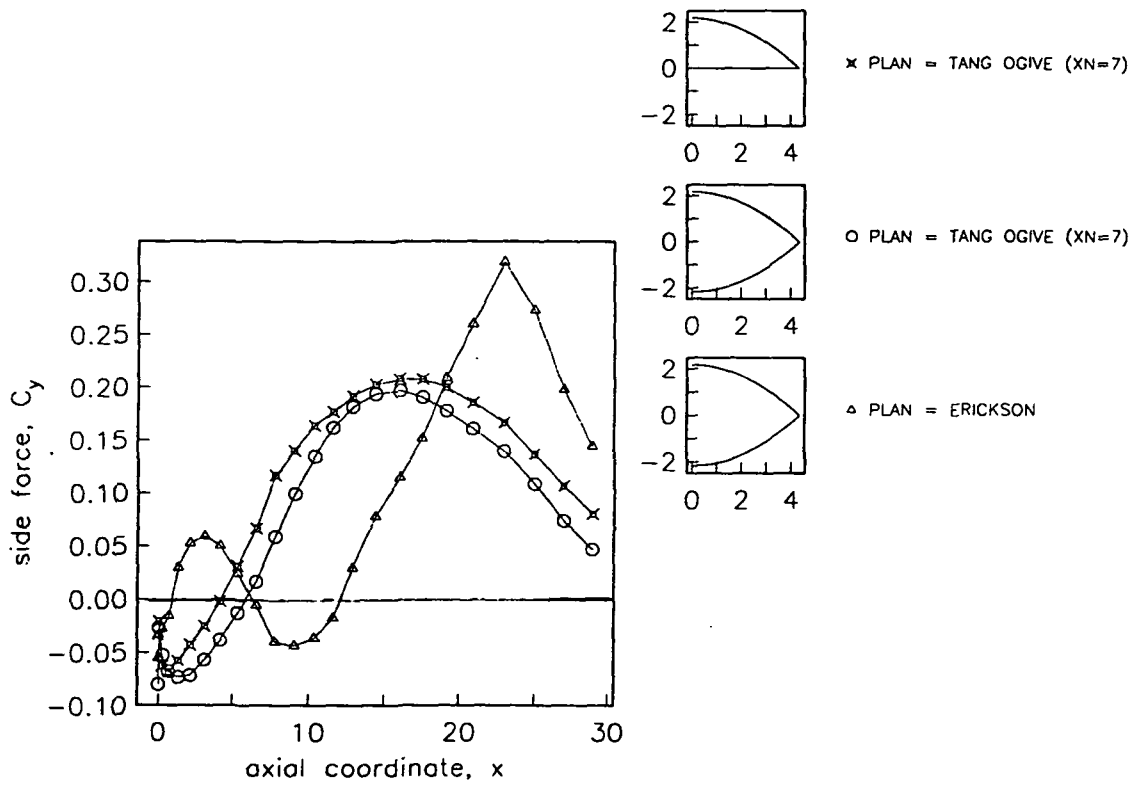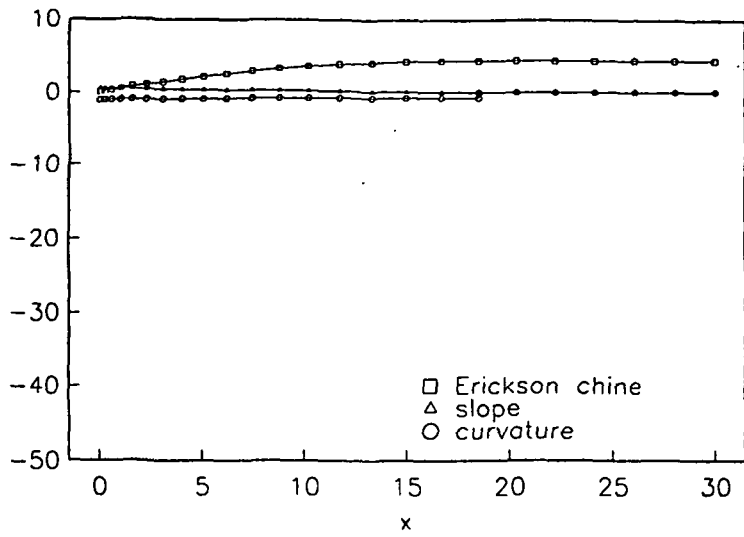Figure 52. Effect of planform shape variation on the side force at $\alpha = 20°$
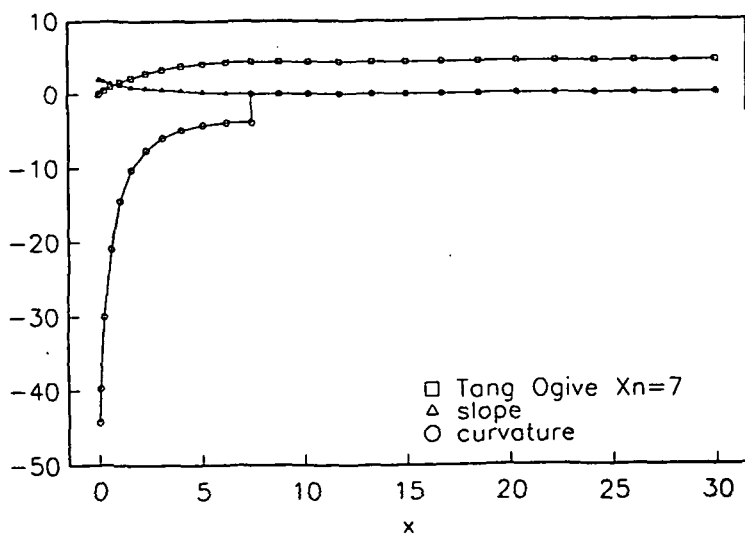
Figure 53. Effect of planform shape variation on the side force at $\alpha = 40°$

a) Erickson chine

b) Tangent Ogive

Figure 54. Variation of planform shapes with their slopes and curvatures

80